UNIVERSITY OF LIVERPOOL

Development of Time-domain Full-field Optical Coherence Tomography as a Non-destructive Testing Method

Thesis submitted in accordance with the requirements of the University of Liverpool for the degree of Doctor in Philosophy

in

Department of Electrical Engineering and Electronics

By

Jinke Zhang

September 2017

Development of Time-domain Full-field Optical Coherence Tomography as a Non-destructive Testing Method

by

Jinke Zhang

Acknowledgments

This thesis could not be finished without the help and support of many people who are gratefully acknowledged here. First and the most important, I would like to express my most sincere gratitude to my supervisor Professor Yao-chun Shen, who always gives various of aspects and suggestions on my PhD works and guides me in my research with his rich experience. He is easy-going in discussing with me, whenever I need his help and support, and strict in my academic research. I would also like to thank Dr. Yalin Zheng, who is my second supervisor from the Department of Eye and Vision Science, for providing me ideas of signal processing of OCT data and useful skills in paper writing, presentations and posters as well as supplying human cornea samples and relative equipment needed in the OCT measurements of corneas.

I would also like to thank Dr. Bryan Williams from the Department of Eye and Vision Science for reviewing and commenting on my manuscripts and providing useful imaging segmentation methods for my OCT data analysis. I would like to thank Pfizer Ltd. for supplying pharmaceutical pellet samples and Jaguar Land Rover Ltd. for providing automotive panel samples. I would like to thank Mr. David Atkinson from School of Engineering for polishing automotive panel samples and providing high magnification microscopy images. I would also thank Dr. Alfred Sidambe for useful discussions and regarding potential comparison with a commercial white light interferometry device.

I am also grateful to thank my current and present colleagues: Dr. Samuel Lawman, Dr. Yue Dong, Dr. Lin Liu, Dr. Chen Li, Dr. Zhe Shen, and Mr. Xiaoran Li, Mr. Zijian Zhang, for your kindness and help through my four-year research.

Last but not least, I would like to thank my family member: my father Mr. Yongming Zhang, my mother Mrs. Yan Wang and my grandmother Mrs. Yuqin Xu for supporting me during my PhD research mentally and financially. I would also like to thank Miss. Yanni Xue for her selfless love and support to my work which would not be finished without her encouragement.

Abstract

Optical coherence tomography (OCT) serves as a non-destructive and non-invasive technique that is capable of imaging the inner structure of optical scattering samples with a high spatial resolution and deep penetration depth. Full-field time-domain OCT (FF-TD-OCT) is an extension of time-domain OCT (TD-OCT) which uses a two-dimensional (2D) detector to capture a series of *en-face* images to reconstruct the inner structure of samples in three-dimension (3D).

In pharmaceutical industry, the pellet or tablet coating performs an important role in the release of active pharmaceutical ingredients (API) and controlling the desired API absorption rate in human body. Therefore, the accurate evaluation of coating thickness is vital to the pharmaceutical coating process. Our FF-TD-OCT system was developed in this research to image the pharmaceutical coating of small size pellets with a high axial resolution of 3.9μm and lateral resolution of 4.4μm. We characterized two pellet samples: a two-layer pellet with one clear coating layer and one drug-loaded layer, and a three-layer pellet with one clear coating layer and two drug-load layers. The mean thickness of a two-layer pellet was precisely determined automatically as 39.7±7.3μm and 49.1±7.0μm for the outer and inner layers respectively. The mean thickness of a three-layer pellet were 26.5±2.3μm, 20.6±3.4μm and 57.3±7.2μm respectively. In addition, the particles in the drug-loaded layer can be clearly resolved form the cross-section image.

The precise and power information of the human corneal surface is of significant benefit in corneal corrective surgeries. Our developed FF-TD-OCT was combined with an average back-vertex focal length and average power

calculation algorithm in order to measure and calculate the individual power of the corneal surface. Meanwhile, the angle of incident light was considered as an important parameter and the errors introduced by the paraxial approximation was reduced. We managed to measure six formalin-fixed and two fresh corneas and map the surface power information of them. In addition, the cross-section image of cornea generated from our FF-TD-OCT system showed its structure including epithelium, Bowman's layer and stroma clearly and the features of the stroma.

For automotive paint system, the metallic flakes in base coat has a significant effect on the appearance of automotive bodies. Precise evaluation of the properties of these flakes is important in the automotive painting system in the purpose for quality assurance. Our FF-TD-OCT system was combined with a 3D variational segmentation method to measure and segment the individual flakes within the base coat of automotive paint system in 3D for the first time. The properties of flakes, including number, size and orientation in 3D space, were precisely calculated, which cannot be achieved by current commercial methods.

Declaration

The author hereby declares that this thesis is a record of work carried out in the Department of Electrical Engineering and Electronics at the University of Liverpool during the period from October 2013 to September 2017. The thesis is original in content except where otherwise indicated.

Table of Contents

List of Figures

List of Tables

Abbreviation

API: active pharmaceutical ingredients

a.u.: arbitrary unit

CCD: charge-coupled device

CLSM: confocal laser scanning microscopy

CMOS: complementary metal-oxide-semiconductor

CT: X-ray computer tomography

DOCT: Doppler optical coherence tomography

DoF: depth of field

FD-OCT: Fourier domain optical coherence tomography

FF-TD-OCT: full field time domain optical coherence tomography

FT: Fourier transform

FWHM: full width at half maximum

GPUs: graphics processor units

HPMC: hydroxypropyl methylcellulose

IOL: intraocular lens

IRT: infrared thermography

LASIK: laser assisted in situ keratomileusis

LCI: low coherence interferometry

LED: light emitting diode

LVC: laser vision correction

MCC: microcrystalline cellulose

MRI: magnetic resonance imaging

NA: numerical aperture

NDT: non-destructive testing

NIR: near-infrared

OCDR: optical coherence-domain reflectometry

OCE: optical coherence elastography

OCM: optical coherence microscopy

OCT: optical coherence tomography

OPD: optical path difference

PMMA: polymethyl-methacrylate

PS-OCT: polarization-sensitive optical coherence tomography

QA: quality assurance

SD-OCT: spectral-domain OCT

SNR: signal to noise ratio

SOCT: spectroscopic optical coherence tomography

SS-OCT: swept-source optical coherence tomography

STD: standard deviation

SVM: support vector machines

TD-OCT: time domain optical coherence tomography

TPI: terahertz pulsed imaging

3D: three-dimensional

Chapter 1. Introduction

Non-destructive testing (NDT) comprises a wide group of inspecting and testing techniques to evaluate the properties of samples or materials without damaging them. NDT methods can keep samples useable after being analysed, which is more effective and sustainable than destructive testing methods, such as metallography and incisional biopsy. NDT methods, such as ultrasonic testing [1,2], electromagnetic testing [3,4] and Terahertz imaging [5,6], are widely used in today's modern industry in order to reduce production costs by inline testing, control manufacturing processes and assure product quality uniformity, integrity and reliability. In medical imaging, NDT allows clinicians to diagnose conditions and design therapy without causing more pain and suffering to patients. Methods such as X-ray computer tomography (CT) [7,8] and magnetic resonance imaging (MRI) [9,10] have been proven to be important tools in diagnosing cancer.

Optical coherence tomography (OCT) has developed rapidly in the past decade. OCT is a three-dimensional (3D) NDT method which uses light imaging in optical scattering media and can achieve high spatial resolution (1-15μm) and high depth penetration at the same time. OCT is based on low-coherence interferometry (LCI) and utilises a light source with low coherence length and broad bandwidth such that the interference of the light occurs over a distance of only a few micrometres. OCT imaging is similar to ultrasound imaging, but it uses a low coherence light source rather than an ultrasound signal. OCT is a tomographic technique that has the capability of obtaining cross-section images within target objects and these slice images of three-dimensional (3D) objects

allow detailed non-invasive inspection. OCT has a great advantage of trade-off between spatial resolution and penetration depth. As shown in Figure 1.1, it achieves a few micrometre resolution and millimetre depth penetration, since it utilises short wavelength light sources such as near-infrared light or visible light. Typical OCT systems can achieve spatial resolution of 1~15μm and penetration depth of a few millimetres. Besides this, OCT has the merits of being non-contact, having low cost, and requiring a relatively simple setup. These advantages allow OCT to be used in many medical related areas including ophthalmology [11,12], dermatology [13], pharmacology [14,15], and pellet coating analysis [16,17] as well as non-medical related areas including automotive paint analysis [18,19].

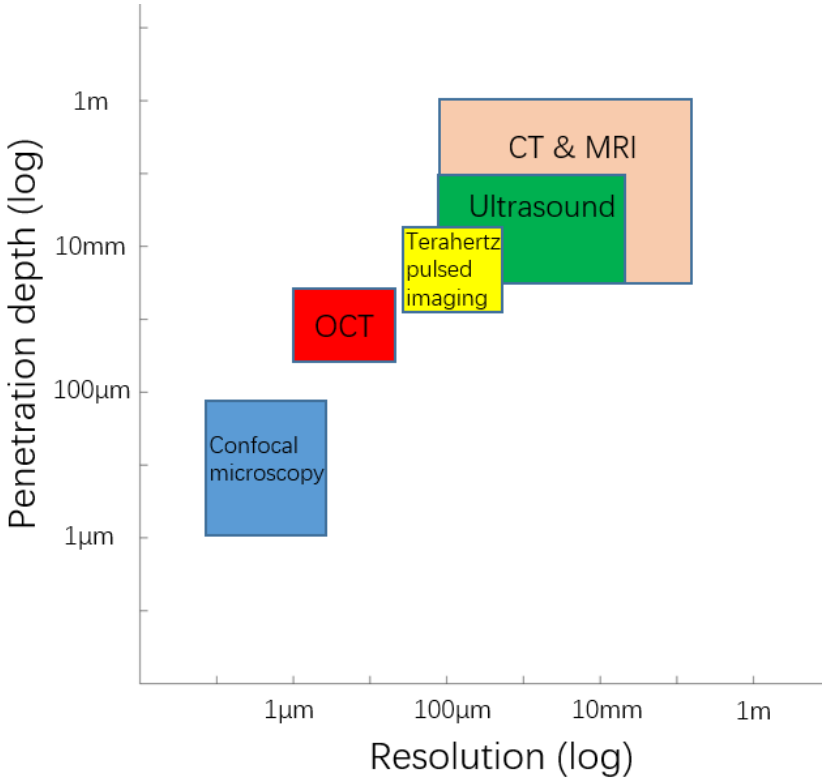

Figure 1.1: Comparison of resolution and penetration depth for confocal microscopy, optical coherence tomography, terahertz pulsed imaging, computed tomography, magnetic resonance imaging and ultrasound imaging.

OCT can be divided in to time-domain OCT (TD-OCT) and Fourier-domain OCT (FD-OCT). In TD-OCT, the optical path difference between the reference and sample is transferred into time difference of backreflecting light. In FD-OCT, interference can be captured by a spectrometer and, after a Fourier transform, the depth profile of samples can be calculated without depth scan. Full-field TD-OCT (FF-TD-OCT) is capable of measuring *en-face* images without lateral scanning by using two-dimensional (2D) detector, such as a charge-coupled device (CCD) or complement metal-oxide-semiconductor (CMOS) camera.

1.1 Motivation

Film coatings have a variety of applications in industrial manufacturing, and one of the oldest uses of film coatings is decoration [20-22]. Products that are beautiful and colourful are more attractive and aesthetically valuable, making them stand out from their competitors and inspiring people to consume them. The primary purpose of film coatings is to perhaps protect materials from wear associated with environmental factors such as UV radiation, bacteria, and moisture, to extend the life of products and reduce replacement costs [23-26]. Protective coatings can provide an effective barrier for substrates against rust, corrosion, and oxidation. In addition, protective coatings can also make materials waterproof [27], fire resistant [28] and scratch resistant [29] for industrial needs. Another purpose of film coating is to control the consumption rate of coated products in certain environments; for example, the film coatings on pharmaceutical tablets or pellets control the release time and rates of active pharmaceutical ingredients (APIs) in the human body and ensure that the patients can absorb the exact dosage demanded by medical treatment [30]. Therefore, it is vital to determine the properties of film coatings accurately—including their thickness distribution, and uniformity—during their fabrication, not only to control their aesthetics but also for quality assurance (QA).

A single layer of coating is insufficient to respond to sophisticated and dynamic environments, so usually two or more coatings are applied in the fabrication process. Coatings can be painted on, sprayed on, plated on or even welded on to a substrate, and the coating materials can consist of various components, such as a mixture of polymers, flakes, pigments, or effective particles. The evaluation of film coatings can be made through destructive

testing methods, which normally include cutting through the sample and measuring the cross section of the sample by using an optical microscope. Destructive methods are easily executed, but they are time-consuming by nature, in both craftsmanship or automated computer-controlled machines and unsustainable and unrestorable for coated samples. Furthermore, destructive methods may change or even damage the coating structures and thus it will cause possible errors in the analysis, especially for specimens with multi-layer thin structures.

In this context, non-destructive testing (NDT) methods are more suitable and valuable than destructive methods in the evaluation of film coating. They make the tested specimens reusable and save both time and money in quality inspection during fabrication. One of the most commonly used NDTs is ultrasound testing, which relies on acoustic echo waves to determine the layer structure to calculate the thickness of layers [1,2]. The commercially available ultrasonic thickness gauge can measure the thickness of a material through contact with its surface. This method of measurement requires a smooth and flat surface for the ultrasonic sensor head to get a precise result, so measurements of non-smooth surfaces can be inaccurate with this method. Another commercial NDT method, eddy-current testing [3,4], uses a coil of conductive wire with an electrical current to produce a magnetic field. This is used to sense defects in conductive samples by approaching them and monitoring phase and amplitude change of the eddy current. However, eddy-current testing can only be applied to non-conductive and non-magnetisable coatings on electrical conducting substrate material, and only measure the overall coating thickness.

In the past few decades, OCT has been applied in several areas as an accurate NDT method that does not require contact. The high resolution (1-15μm) and good penetration (1-2mm) capability of OCT makes it suitable for thin film coating evaluation. Thus, one of the research focuses of my PhD work is to develop an FF-TD-OCT system for characterizing the thin film coatings of several specimens, more specifically for pharmaceutical pellets and automotive paint panels for the following reasons.

In the pharmaceutical industry, the film coating of pellets or tablets is designed to control the release of API molecules in the human body [30], as well as to mask taste, improve drug stability and the physical separation of incompatible components in the same dosage form [31]. The film coating thickness effects the decomposition speed of pellets or tablets in human body. Therefore, it is significant to precisely evaluate the coating thickness of film coatings applied to pharmaceutical tablets or pellets during the production process in order to ensure their high quality and uniformity. Several non-destructive analytical imaging techniques have demonstrated their capability to quantitatively characterise coatings of individual pharmaceutical pellets or tablets, including near-infrared (NIR) spectroscopy [32,33] and terahertz pulsed imaging (TPI) [34-36]. High spatial resolution is required to evaluate small pellets, but TPI has a relatively low spatial resolution, insufficient to resolve a thin coating layer less than 40μm [15]. However, previous studies have demonstrated the capability of OCT to characterise coating thickness and evaluate the coating structure of pharmaceutical pellets [16] and in-line monitoring of the pellet-coating process [37]. To get the coating structure, though, these studies focussed on the cross-section (B-scan) images of pellet samples, instead of on 3D data, and this method may be inaccurate in

calculating the coating thickness. The aim of this research is to address the coating thickness distribution of small pellets by using our FF-TD-OCT system.

In the automotive industry, the film coating systems protect vehicles' bodies from corrosion, as well as providing aesthetic enhancement [38,39]. The base coat layer of automotive coating systems provides the colour of choice, which is mixed with primary colour pigment and metallic or mica flakes. The flake size, weight, orientation and geometry has an effect on the desired appearance from all angles. Therefore, the measurement of these flake properties would be beneficial in automotive industrial production to achieve the desired appearance and maintain the consistency of the automotive paint. The most commonly used method of measuring film coating thickness, ultrasound testing, is unsuitable in the measurement of flakes, because of its need to contact the measured surface and its insufficient resolution for gauging small flakes of approximately a 10μm radius. Another commercial method for measuring paint layer thickness, eddy-current testing [40,41], uses a coil of conductive wire with an electrical current to produce a magnetic field. Because eddy-current testing can be applied only to non-conductive and non-magnetisable coatings on electrical conducting substrate material and the film builds of automotive paint are all non-magnetisable, this method can measure only the overall coating thickness of automotive paint layers [42], and it is impossible for it to resolve small flakes. The non-contact TPI method has been applied to the measurement of automotive coating thickness before [43-45]. However, the lateral resolution of TPI is limited by its wavelength and is unsuitable for characterising the small flakes (typically of a radius of 10μm) in automotive base coats. Therefore, we present our FF-TD-OCT, which is non-contact and non-destructive and has sufficient spatial resolution, to measure small metallic

flakes in the automotive paint system. The aim of this research is to explore the properties of individual flakes by using the FF-TD-OCT technique.

One of the major contribution of this thesis is that we combine our FF-TD-OCT system and a novel 3D variational OCT image segmentation method to distinguish individual flakes automatically and measure their properties, including the size, number and orientation, for the first time, a result that has not been achieved by any other measurement method. This method is therefore beneficial to the automotive industry as a QA tool for film coating processes.

Another objective of this thesis is to measure the individual optical power of cornea samples by using our FF-TD-OCT system, in collaboration with the Department of Eye and Vision Science. The ability to measure and analyse the shape and power of the human cornea is beneficial for undertaking therapeutic surgical treatment of ophthalmological diseases, such as astigmatism and glaucoma, which may cause distorted or blurred vision and even vision loss at all distances. Precise information concerning the shape and power of the corneal surface is of significance to any corrective procedures to the corneal surface. Previous OCT applications in corneal power measurement have focussed on net power instead of individual optical power at each location [46], since the local power can provide more corneal information, such as the location of disease region. Due to the limitations of scanning point OCT, the corneal surface is scanned radially along a series of meridians across the vertex. From each meridional image, the refractive power of the corneal anterior surface is determined. However, the surface map of the cornea should be adjusted with a motion-correction algorithm due to the motion of human eye *in vivo* and possible errors in non-telecentric scan deformation [47]. Additionally,

the paraxial approximation, which is a small-angle approximation in optical system, will not be accurate outside the central corneal region, and significant errors can be introduced when calculating individual power in corneal tomography. The aim of this research is to solve the non-telecentric scan problem physically and reduce errors from the paraxial approximation by combining our FF-TD-OCT system (which avoids lateral scan and acquires *en-face* images of cornea samples) with a back-vertex focal power calculation (which avoids the paraxial approximation).

1.2 Organisation of thesis

Chapter 2 introduces the background of the OCT technique including its development and history, its principles and performance and several important extensions of OCT.

Chapter 3 describes the implementation of our compact free-space FF-TD-OCT system and its design, development and imaging performance.

Chapter 4 focuses on the coating thickness measurement and analysis of small pharmaceutical pellet samples with the size of less than 1mm and multilayer structure.

Chapter 5 presents surface measurements of fresh and formalin-fixed corneas and their lens power calculation. The individual power of cornea surface is calculated with a power calculation method, which considers the incident angle of light as an independent variable.

Chapter 6 shows the non-destructive measurement of automotive panel samples and the variational segmentation of metallic flakes within the base coat layer of automotive paint systems. The properties, including size, number and orientation, were calculated for four different kinds of automotive panel samples.

Chapter 7 concludes the work of this thesis and suggests avenues for future work.

1.3 List of publications

The work of this PhD thesis has resulted in the following publications:

- Journal papers:

1. **Zhang, J.**, Williams, B., Lawman, S., Atkinson, D., Zhang, Z., Shen, Y.-C., & Zheng, Y. (2017). Non-destructive Analysis of Flake Properties in Automotive Paints with Full-field Optical Coherence Tomography and 3D Segmentation. Optics Express, 25(16), 18614-18628.

2. Lawman, S., Williams, B., **Zhang, J.**, Shen, Y. -C., & Zheng, Y. (2017). Scan-Less Line Field Optical Coherence Tomography, with Automatic Image Segmentation, as a Measurement Tool for Automotive Coatings. Applied Sciences, 7(4), 351.

3. Dong, Y., Lawman, S., Zheng, Y., Williams, D., **Zhang, J.**, & Shen, Y. -C. (2016). Nondestructive analysis of automotive paints with spectral domain optical coherence tomography. Applied Optics, 55(13), 3695-3700.

- Conference papers:

1. **Zhang, J.**, Shen, Y., & Zheng, Y. (2015, October). The Application of Full-Field Optical Coherence Tomography on Evaluating Film Coating of Pharmaceutical Pellets. In Computer and Information Technology; Ubiquitous Computing and Communications; Dependable, Autonomic and Secure Computing; Pervasive Intelligence and Computing (CIT/IUCC/DASC/PICOM), 2015 IEEE International Conference on (pp. 1046-1050). IEEE.

2. Dong, Y., **Zhang, J.**, Shen, Y. C., Su, K., & Zeitler, J. A. (2015, August). Non-destructive characterization of automobile car paints using terahertz pulsed imaging and infrared optical coherence tomography. In Infrared, Millimeter, and Terahertz waves (IRMMW-THz), 2015 40th International Conference on (pp. 1-2). IEEE.

3. Lawman, S., **Zhang, J.**, Williams, B. M., Zheng, Y., & Shen, Y. C. (2017, June). Applications of optical coherence tomography in the non-contact assessment of automotive paints. In SPIE Optical Metrology (pp. 103290J-103290J). International Society for Optics and Photonics.

References

1. J. Allin, P. Cawley, and M. Lowe, “Adhesive disbond detection of automotive components using first mode ultrasonic resonance,” NDT & E International 36, 503–514 (2003).

2. S. A. Titov, R. G. Maev, and A. N. Bogachenkov, “Pulse-echo NDT of adhesively bonded joints in automotive assemblies,” Ultrasonics 48, 537–546 (2008).

3. B. Auld and J. Moulder, “Review of advances in quantitative eddy current nondestructive evaluation,” Journal of Nondestructive Evaluation 18, 3–36 (1999).

4. J. García-Martín, J. Gómez-Gil, and E. Vázquez-Sánchez, “Non-destructive techniques based on eddy current testing,” Sensors 11, 2525–2565 (2011).

5. Y.-C. Shen, T. Lo, P. Taday, B. Cole, W. Tribe, and M. Kemp, “Detection and identification of explosives using terahertz pulsed spectroscopic imaging,” Applied Physics Letters 86, 241116 (2005).

6. Y.-C. Shen, “Terahertz pulsed spectroscopy and imaging for pharmaceutical applications: a review,” International Journal of Pharmaceutics 417, 48–60 (2011).

7. A.C. Kak, and M. Slaney, *Principles of computerized tomographic imaging* (Society for Industrial and Applied Mathematics, 2001).

8. V. Cnudde and M.N. Boone, “High-resolution X-ray computed tomography in geosciences: A review of the current technology and applications,” Earth-Science Reviews 123, 1-17 (2013).

9. E. Warner, H. Messersmith, P. Causer, A. Eisen, R. Shumak, and D. Plewes, “Systematic Review: Using magnetic resonance imaging to screen women at high risk for breast cancer using MRI to screen women at high risk for breast cancer,” Annals of Internal Medicine 148(9), 671-679 (2008)

10. N. Houssami, S. Ciatto, P. Macaskill, S.J. Lord, R. M. Warren, J.M. Dixon, and L. Irwig, “Accuracy and surgical impact of magnetic resonance imaging in breast cancer staging: systematic review and meta-analysis in detection of multifocal and multicentric cancer,” Journal of Clinical Oncology 26(19), 3248-3258 (2008).

11. R. J. Antcliff, D. J. Spalton, M. R. Stanford, E. M. Graham, and J. Marshall, “Intravitreal triamcinolone for uveitic cystoid macular edema: an optical coherence tomography study,” Ophthalmology 108(4), 765-772 (2001).

12. M. Wojtkowski, V. Srinivasan, J. G. Fujimoto, T. Ko, J. S. Schuman, A. Kowalczyk, and J. S. Duker, “Threedimensional retinal imaging with high-speed ultrahigh-resolution optical coherence tomography,” Ophthalmology 112(10), 1734-1746 (2005).

13. M. Mogensen, L. Thrane, T. M. JÃ ÿrgensen, P. E. Andersen, and G. Jemec, “Optical coherence tomography for imaging of skin and skin diseases,” in Seminars in cutaneous medicine and surgery, (2009), pp. 196-202

14. J. Mauritz, R. S. Morrisby, R. S. Hutton, C. H. Legge, and C. F. Kaminski, “Imaging pharmaceutical tablets with optical coherence tomography,” Journal of Pharmaceutical Sciences 99(1), 385-391 (2010).

15. S. Zhong, Y.-C. Shen, L. Ho, R. K. May, J. A. Zeitler, M. Evans, P. F. Taday, M. Pepper, T. Rades, K. C. Gordon, and R. Müller, “Non-destructive quantification of pharmaceutical tablet coatings using terahertz pulsed imaging and optical coherence tomography,” Optics and Lasers in Engineering 49(3), 361-365 (2011).

16. C. Li, J. A. Zeitler, Y. Dong, and Y.-C. Shen, “Non-destructive evaluation of polymer coating structures on pharmaceutical pellets using full-field optical coherence tomography,” Journal of Pharmaceutical Sciences 103(1), 161-166 (2014).

17. J. Zhang, Y.-C. Shen, and Y. Zheng, “The application of full-field optical coherence tomography on evaluating film coating of pharmaceutical pellets,” in IEEE International Conference on Computer Science and Information Technology, (2015), pp. 1046-1050.

18. Y. Dong, S. Lawman, Y. Zheng, D. Williams, J. Zhang, and Y.-C. Shen, “Nondestructive analysis of automotive paints with spectral domain optical coherence tomography,” Applied Optics 55(13), 3695-3700 (2016).

19. S. Lawman, B. M. Williams, J. Zhang, Y. C. Shen, and Y. Zheng, “Scan-Less Line Field Optical Coherence Tomography, with Automatic Image Segmentation, as a Measurement Tool for Automotive Coatings,’’ Applied Sciences 7(4), 351(2017).

20. B. Richey and M. Burch, “Applications for decorative and protective coatings,” Polymer Dispersions and Their Industrial Applications, 123-161 (2002).

21. K. C. Shimpi, K. Ravindranath, A. K. Jani, D. C. Kothari and C. S. Harindranath, “Decorative coatings produced using combination of reactive arc evaporation and magnetron sputtering,” Surface and Coatings Technology 90(1-2), 115-122 (1997).

22. E. Budke, J. Krempel-Hesse, H. Maidhof and H. Schüssler, “Decorative hard coatings with improved corrosion resistance,” Surface and Coatings Technology 112(1), 108-113 (1999).

23. R. M. Burns and A. E. Schuh, “Protective coatings for metals,” Reinhold Publishing Corporation. New York (1939).

24. C. G. Munger and L. D. Vincent, “Corrosion prevention by protective coatings,” (1999).

25. J. E. Gray and B. Luan, “Protective coatings on magnesium and its alloys—a critical review,” Journal of alloys and compounds 336(1), 88-113 (2002).

26. K. H. Stern, “Metallurgical and ceramic protective coatings,” Springer Science & Business Media (1996).

27. A. Barbucci, M. Delucchi and G. Cerisola, “Organic coatings for concrete protection: liquid water and water vapour permeabilities,” Progress in Organic coatings 30(4), 293-297 (1997).

28. S. Duquesne, S. Magnet, C. Jama and R. Delobel, “Intumescent paints: fire protective coatings for metallic substrates,” Surface and Coatings Technology 180, 302-307 (2004).

29. C. Charitidis, A. Laskarakis, S. Kassavetis, C. Gravalidis and S. Logothetidis, “Optical and nanomechanical study of anti-scratch layers on polycarbonate lenses,” Superlattices and Microstructures 36(1), 171-179 (2004).

30. C. A. Gilligan, and A. Li Wan Po, “Factors affecting drug release from a pellet system coated with an aqueous colloidal dispersion,” International Journal of Pharmaceutics 73(1), 51–68 (1991).

31. N. Oman Kadunc, R. Šibanc, R. Dreu, B. Likar, and D. Tomaževič, “In-line monitoring of pellet coating thickness growth by means of visual imaging,” International Journal of Pharmaceutics 470(1–2), 8–14 (2014).

32. M.-J. Lee, D.-Y. Seo, H.-E. Lee, I.-C. Wang, W.-S. Kim, M.-Y. Jeong, and G. J. Choi, “In line NIR quantification of film thickness on pharmaceutical pellets during a fluid bed coating process,” International Journal of Pharmaceutics 403(1–2), 66–72 (2011).

33. M. Andersson, S. Folestad, J. Gottfries, M. O. Johansson, M. Josefson, and K.-G. Wahlund, “Quantitative analysis of film coating in a fluidized bed process by in-line NIR spectrometry and multivariate batch calibration,” Analytical Chemistry 72(9), 2099–2108 (2000).

34. L. Ho, Y. Cuppok, S. Muschert, K. C. Gordon, M. Pepper, Y. Shen, F. Siepmann, J. Siepmann, P. F. Taday, and T. Rades, “Effects of film coating

thickness and drug layer uniformity on in vitro drug release from sustained-release coated pellets: A case study using terahertz pulsed imaging," International Journal of Pharmaceutics 382(1–2), 151–159 (2009).

35. L. Ho, R. Müller, M. Römer, K. C. Gordon, J. Heinämäki, P. Kleinebudde, M. Pepper, T. Rades, Y. C. Shen, C. J. Strachan, P. F. Taday, and J. A. Zeitler, "Analysis of sustained-release tablet film coats using terahertz pulsed imaging," Journal of Controlled Release 119(3), 253–261 (2007).

36. J. A. Zeitler, P. F. Taday, D. A. Newnham, M. Pepper, K. C. Gordon, and T. Rades, "Terahertz pulsed spectroscopy and imaging in the pharmaceutical setting - a review," Journal of Pharmacy and Pharmacology 59(2), 209–223 (2007).

37. D. Markl, M. Zettl, G. Hannesschläger, S. Sacher, M. Leitner, A. Buchsbaum, and J. G. Khinast, "Calibration-free in-line monitoring of pellet coating processes via optical coherence tomography," Chemical Engineering Science 125, 200–208 (2015).

38. N. K. Akafuah, S. Poozesh, A. Salaimeh, G. Patrick, K. Lawler, and K. Saito, "Evolution of the automotive body coating process - a review," Coatings 6, 24 (2016).

39. M. Nichols and J. Tardiff, Active Protective Coatings (Springer Netherlands, 2016), chap. Automotive Coatings, 373–384.

40. B. Auld and J. Moulder, "Review of advances in quantitative eddy current nondestructive evaluation," Journal of Nondestructive Evaluation 18, 3–36

(1999).

41. J. García-Martín, J. Gómez-Gil, and E. Vázquez-Sánchez, “Non-destructive techniques based on eddy current testing,” Sensors 11, 2525–2565 (2011).

42. K. Su, Y.-C. Shen, and J. A. Zeitler, “Terahertz sensor for non-contact thickness and quality measurement of automobile paints of varying complexity,” IEEE Transactions on Terahertz Science and Technology 4, 432–439 (2014).

43. K. Su, Y.-C. Shen, and J. A. Zeitler, “Terahertz sensor for non-contact thickness and quality measurement of automobile paints of varying complexity,” IEEE Transactions on Terahertz Science and Technology 4, 432–439 (2014).

44. S. Krimi, J. Klier, J. Jonuscheit, G. von Freymann, R. Urbansky, and R. Beigang, “Highly accurate thickness measurement of multi-layered automotive paints using terahertz technology,” Applied Physics Letters 109, 021105 (2016).

45. M. Sudo, J. Takayanagi, and H. Ohtake, “Nondestructive thickness measurement system for multiple layers of paint based on femtosecond fiber laser technologies,” Journal of Infrared Millimeter and Terahertz Waves 37, 1139–1147 (2016).

46. M. Tang, A. Chen, Y. Li, and D. Huang, “Corneal power measurement with Fourier-domain optical coherence tomography,” Journal of Cataract & Refractive Surgery, 36(12), 2115–2122 (2010).

47. M. Zhao, A. N. Kuo, and J. A. Izatt, “3D refraction correction and extraction of clinical parameters from spectral domain optical coherence tomography of the cornea,” Optics Express, 18 (9), 8923 (2010).

Chapter 2. Background of optical coherence tomography

Optical coherence tomography (OCT) is a non-destructive cross-sectional imaging technique with micron scale resolution for optical scattering samples. This chapter introduces the history and development of optical coherence tomography as well as its principle, performance and serval important extensions.

2.1 Historical overview

The root of OCT lies in the early work on white-light interferometry that led to the development of optical coherence-domain reflectometry (OCDR), which is a one-dimensional optical ranging technique developed for detecting faults in optical cables and network components [1,2]. With superb optical sectioning ability of OCT, the first OCT system was introduced by Huang et. al in 1991 [3]. It uses low-coherence interferometry (LCI) to produce high-resolution 2D cross-sectional images of the internal microstructure of the human tissue by measuring backscattering or back-reflected lights from a reference arm and a sample arm in the time domain (TD). The interference occurs when the path lengths of two backscattering light beams from two arms are within the coherence length of the light source.

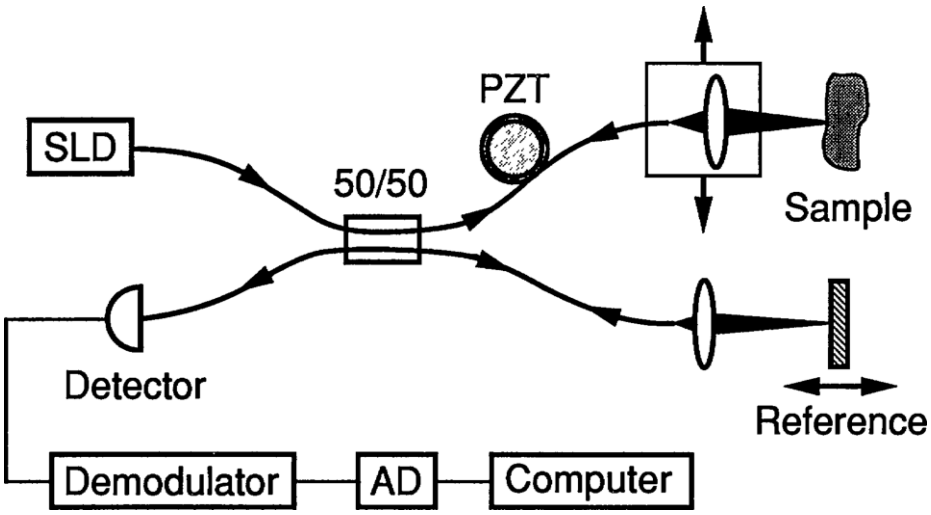

Figure 2.1: The schematic of the first OCT system by Huang et al. [3]. PZT: piezoelectric transducer; SLD: superluminescent diode; AD: digitized.

The first *in vivo* OCT was applied in ophthalmology by Fercher et. al [4] in 1993. In the same year, the first *in vivo* measurement of human retinal structure by OCT was obtain by the Fujimoto group [5]. They achieved a relative high acquisition speed in live patients less than 3 seconds and proved the clinical feasibility of OCT in various retinal imaging applications. Afterwards, OCT was applied to other clinical applications including dermatology [6,7], and tissue morphology [9-10]. The promising ability of non-destructive, high-resolution, micrometre-scale, cross-sectional imaging in biological systems made OCT an important non-excisional 'optical biopsy' technique in preliminary clinical practice.

However, early TD-OCT had a limitation in the scanning speed which was only about hundreds of A-scans/s because of its physical constraint of a moving reference mirror. In order to extract the depth profile of samples, TD-OCT obtains time-encoded signals with the depth scan of the reference mirror and

thus the changing location of the reference mirror allows OCT to detect the different depths in the sample. Therefore, the traditional TD-OCT is very slow in scanning speed.

One way to improve the acquisition speed is to detect backscattering signals in spectral domain without the movement of the reference mirror. The backscattered depth information can be encoded in frequency and transferred into time domain through an inverse Fourier transform (FT), which is Fourier-domain OCT(FD-OCT). FD-OCT detection can be achieved either by using a spectrometer (called spectral-domain OCT or SD-OCT) or by using a rapidly tunable laser (called swept-source OCT or SS-OCT). The first FD-OCT application was presented by Fercher et al. [11] in 1995 for corneal thickness measurement. Then a similar spectral interferometric instrument named spectral radar was invented for dermatological diagnosis. However, these early works on FD-OCT did not result in good quality of cross-sectional images, since they used relatively narrow spectral bandwidths. Until 2002, FD-OCT technology was demonstrated to obtain the first decent *in vivo* tomograms of human retina and allow a quantitative estimation of the thickness of different retinal layers [12]. Later studies demonstrated that FD-OCT has better sensitivity and signal-to-noise ratio (SNR) over traditional TD-OCT [13-15], which allows FD-OCT to perform better in fast dynamic physiologic processes. Nowadays, FD-OCT is able to achieve the high acquisition speed of 1 million A-scans/s [16].

Another solution to improve the acquisition speed is Full-field TD-OCT (FF-TD-OCT), which produces tomographic images in the *en-face* orientation without the lateral moving of sample [17-23]. The entire field of samples, rather

than a signal point, were illuminated with low coherence light and the tomographic images can be acquired by a two-dimensional (2D) detector, such as a charge-coupled device (CCD) or complementary metal-oxide-semiconductor (CMOS) camera. In other words, a number (dependent on the pixel number of detector) of A-scans in parallel could be obtained by the FF-TD-OCT technique and thus the acquisition speed is largely increased.

Currently, the OCT technique is not only applied to biological tissues for clinical imaging [24-28] but also non-biological areas to detect defects and measure film coating thickness, such as pharmacy [29-35], automotive paint [36-41], and electronic device [42-44]. OCT exhibits several outstanding properties that make it popular in non-destructive I imaging. Firstly, the axial resolution of OCT is decoupled from the lateral resolution and is only dependent on the light source spectrum. Therefore, axial resolution in the histological 1μm range is possible. High lateral resolution can be obtained by the numerical aperture (NA) beams as in classical imaging. Secondly, OCT can provide high dynamic range and sensitivity (>100dB) [45]. Thirdly, OCT has the ability to distinguish detailed layered structures in millimetre ranges beneath the surface of a sample. Last but not least, OCT is a non-invasive technique which uses non-ionizing radiation and allows minimum damage with *in vivo* testing and repeated measurements [45].

2.2 Principle of optical coherence tomography

Figure 2.2 shows a standard OCT Michelson interferometer which uses a low coherence light source. There are two basic scan procedures in OCT: a depth scan (axial scan or A-scan) performed by a reference mirror and a lateral

scan performed by moving samples or scanning probe beams. With a series of adjacent depth scans, OCT can create cross-sectional (B-scan) images [45].

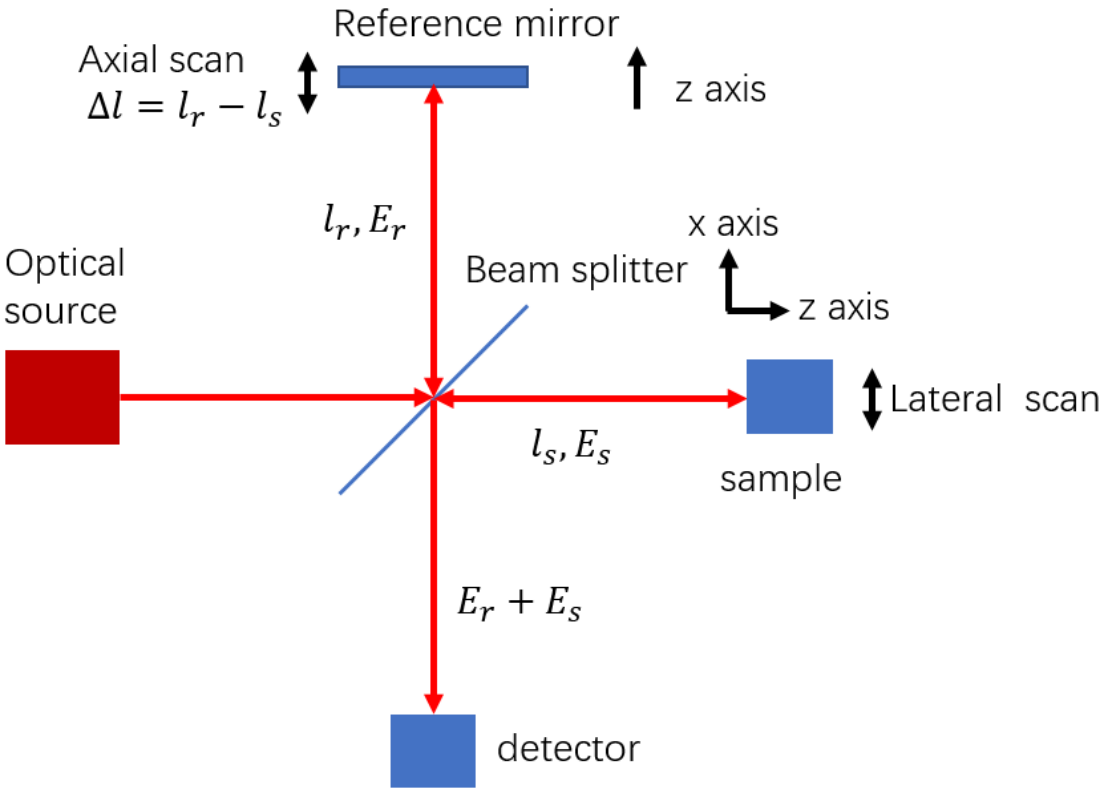

Figure 2.2: A standard OCT scheme based on a low coherence Michelson interferometer.

The light beam from source is divided by a beam splitter into sample and reference beams. l_r and l_s are the distances of the sample and reference mirror placed away from beam splitter respectively. The backscattering light from the sample and reference arm is recombined in the beam splitter and the interference occurs when the optical path difference $\Delta l = l_r - l_s$ is within the coherence length.

For a coherent light source, the electric fields of both arms E_r and E_s are collected at the detector exit and they can be expressed as [45]:

$$E_r = A_r \exp(-2j\beta_r l_r - j\omega t) \text{ and } E_s = A_s \exp(-2j\beta_s l_s - j\omega t) \quad (2.1)$$

, where ω is the frequency of the light source and β is a propagation constant. Since the light beams are reflected from the reference and sample, the propagation constant is multiplied by a factor of 2. After reflection and recombination at beam splitter, the time average photocurrent I_e at the detector exit can be expressed as [45]:

$$I_e = \langle \frac{\eta e}{h\nu} \cdot \frac{|E_r + E_s|^2}{2\eta_0} \rangle \quad (2.2)$$

, where η is the detector quantum efficiency, e is the electronic charge, $h\nu$ is the photon energy, η_0 is the intrinsic impedance of free space and the angle bracket $\langle \dots \rangle$ means the time average. For monochromatic fields, Equation (2.2) can be expressed as [45]:

$$I_e = \frac{\eta e}{2\eta_0 h\nu} [|A_r|^2 + |A_s|^2 + 2Re\{E_r E_s{}^*\}] \quad (2.3)$$

, where the real term

$$Re\{E_r E_s{}^*\} = A_r A_s \cos(2\beta_r l_r - 2\beta_s l_s) \quad (2.4)$$

In free space, the propagation constants are equal for both reference and sample arms $\beta_r = \beta_s = \frac{2\pi}{\lambda}$ and

$$Re\{E_r E_s{}^*\} = A_r A_s \cos\left(2\pi \cdot \frac{2\Delta l}{\lambda}\right) \quad (2.5)$$

, where $\Delta l = l_r - l_s$.

Equation (2.5) shows the photocurrent at detector exit contains a sinusoidally varying term representing the interference between the reference and sample fields.

For a low-coherent light source, the spectrum contains a limited bandwidth of frequencies rather than a single frequency. The reference and sample fields can be expressed as functions of frequency ω [45]:

$$E_r(\omega) = A_r(\omega)\exp(-2j\beta_r(\omega)l_r - j\omega t) \text{ and}$$

$$E_s(\omega) = A_s(\omega)\exp(-2j\beta_s(\omega)l_s - j\omega t) \quad (2.6)$$

The real part of $E_r E_s^*$ can be expressed as [45]:

$$Re\left\{\int_{-\infty}^{\infty} E_r(\omega)E_s(\omega)^* \frac{d\omega}{2\pi}\right\} = Re\left\{\int_{-\infty}^{\infty} S(\omega)\exp\left(-j\Delta\phi(\omega)\right)\frac{d\omega}{2\pi}\right\} \quad (2.7)$$

, where $\Delta\phi(\omega)$ is the phase difference between sample and reference arms [45]:

$$\Delta\phi(\omega) = 2\beta_s(\omega)l_s - 2\beta_r(\omega)l_r \quad (2.8)$$

and $S(\omega)$ is the power spectrum of light source [45]:

$$S(\omega) = A_r(\omega)A_s(\omega)^* \quad (2.9)$$

2.2.1 Noise sources

The dominating noise sources in OCT system are shot noise, thermal noise and excess intensity noise [46,47]:

Thermal noise

Thermal noise (Johnson-Nyquist noise) results from the random motion of electrons due to the thermal energy of a system [48-52]. It can be regarded as the transfer energy and temperature equilibrium between an ideal noisy resistor and its environment since resistors are the only element that exchange energy with the environment. Thus, the thermal noise power can be expressed as:

$$N_{th} = \frac{2KT}{R} \tag{2.10}$$

, where T is the temperature, K is the Boltzmann's constant and R is the resistance of the ideal resistor.

Shot noise

Shot noise (Poisson noise) results from the particle nature of light and discrete nature of electric charge [51,52]. The emission of charge in a photodetector is related to the photocurrent but the time intervals of charge emissions are random due to the Poisson distribution. The power of shot noise is associated with the detector photocurrent and can be expressed as:

$$N_{sh} = 2eB\langle i \rangle \tag{2.11}$$

, where B is the electronics bandwidth, $\langle i \rangle$ the mean detector photocurrent and e is the electronic charge.

Excess intensity noise

Excess intensity (spontaneous beating noise) noise results from the self-beating of broad-band light waves and is linearly proportional to the mean photocurrent power $\langle i \rangle^2$ [45,53]. The power of excess intensity noise can be modelled as:

$$N_{ex} = \zeta e B \langle i \rangle^2 \tag{2.12}$$

, where ζ is a noise parameter determined by experiment.

2.2.2 Sensitivity

The sensitivity is one of the main parameter of an OCT instrument. It is defined as the minimum detectable reflectivity of the OCT system. The sensitivity S of an OCT system can be regarded as the ratio of signal power generated by a perfectly reflecting reference mirror. The weakest sample reflectivity $R_{s,min}$ yields a signal power equal to the noise of the system [45]. Therefore, we have:

$$S = \frac{1}{R_{s,min}}\Big|_{SNR=1} \tag{2.13}$$

, where SNR is the signal to noise ratio. The sensitivity advantage is one of the most important key features of an OCT system because interference can amplify weak signals and increase sensitivity.

The effective signal photocurrent at the detector exit i_e can be expressed from the interference term:

$$i_e = \frac{\eta e}{h\nu}\sqrt{2P_sP_r} \tag{2.14}$$

, where P_s and P_r are the powers of the sample and reference reflection received by the detector. The SNR is the ratio of the mean power and the total noise power including thermal noise N_{th}, shot noise N_{sh} and excess intensity noise N_{ex}, given as:

$$\mathrm{SNR} = \frac{P_{signal}}{P_{noise}} = \frac{{i_e}^2}{N_{th}+N_{sh}+N_{ex}} = \frac{2\chi^2 P_sP_r}{\frac{2KT}{R}+2eB\langle i\rangle+\zeta eB\langle i\rangle^2} \tag{2.15}$$

, where $\chi = \frac{\eta e}{h\nu}$.

With an ideal and symmetric beam splitter, the powers of the sample and reference arm can be expressed as:

$$P_s = \frac{P_{source}R_s}{4}, P_r = \frac{P_{source}R_r}{4} \tag{2.16}$$

, where P_{source} is the output power of the light source and R_s and R_r are the reflectivity of the sample and reference mirror. Assume that the photocurrent $\langle i\rangle$ is only determined by the reference beam. Then we have the sensitivity S:

$$\mathrm{S} = \frac{\frac{1}{8}\chi^2{P_{source}}^2R_r}{\frac{2KT}{R}+\frac{1}{2}eB\chi P_{source}\sqrt{R_r}+\frac{1}{8}\zeta eB\chi^2{P_{source}}^2R_r} \tag{2.17}$$

We further assume that the reference mirror is perfect ($R_r = 1$) and the shot noise is the domination of system noise. Then, we have the sensitivity S:

$$\mathrm{S} = \frac{\chi P_{source}}{4eB} \tag{2.18}$$

, which means that the sensitivity is proportional to the source power and inversely proportional to the electronics bandwidth [45].

2.2.3 Resolution

Spatial resolution is one of the most important parameters in an OCT system. It is defined as the smallest distance between two points that can be distinguished as separate in an imaging system. The higher the resolution, the smaller the distance we can distinguish. Commonly, spatial resolution is divided into axial resolution and lateral resolution.

Axial resolution, also known as depth resolution, is the resolution in the direction of the light source beam. In an OCT system, the axial resolution is independent of the optics and defined by half of the coherence length of the light source, which is the propagation distance over which a coherent wave can maintain a specified degree of coherence. It can be determined as the full width at half maximum (FWHM) of the interference signal envelope [45,54]:

$$\mathrm{z} = \frac{l}{2} = \frac{2\ln 2}{\pi}\frac{\lambda^2}{\Delta\lambda} \tag{2.19}$$

, where z is the axial resolution, l is coherent length of the light source, λ and $\Delta\lambda$ are the centre wavelength and bandwidth of light source respectively.

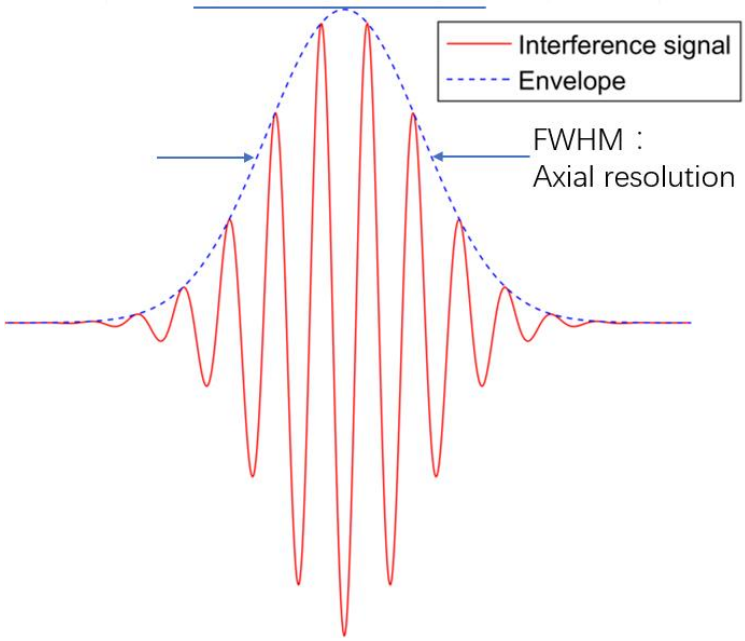

Figure 2.3: A typical interference signal and its envelope from the Hilbert transform. The Full-width at half of maximum (FWHM) intensity indicates the axial resolution in this OCT system.

Lateral resolution, or transverse resolution, in a single point scanning OCT system, is limited either by an insufficient lateral sampling rate or the diameter of the focus spot size of the probe beam. For a Gaussian sample beam, it can be defined as the FWHM of the beam waist [45, 55-57]:

$$d = 2\sqrt{\ln 2}\,\omega_0 = 2\sqrt{\ln 2}\,\frac{\lambda}{\pi\theta} \tag{2.20}$$

, where λ is the centre wavelength of the light source, ω_0 is the beam waist, θ is the angular spread of the Gaussian beam, and $\sin\theta$ is the numerical aperture (NA).

The lateral resolution of an FF-TD-OCT system is also limited by the pixel size of 2D the detector since the FF-TD-OCT system capture a series of *en-face* images. The lateral resolution should be no smaller than twice the pixel size.

2.2.4 Depth of field

The depth of field (DoF) is defined as double of the Rayleigh length which is the distance along the propagation from the waist to the place where the area is doubled. Therefore, we have the DoF:

$$\mathrm{DoF} = 2\frac{\lambda}{\pi\theta^2} \tag{2.21}$$

From Equation (2.20) and (2.21), a high lateral resolution is associated with a large NA, while the higher NA will reduce the DoF dramatically. Hence, a compromise has to be found between the desired lateral resolution and DoF in OCT experiment. Figure 2.4 shows a typical Gaussian beam with the beam width of $w(z)$ as a function of distance z along the beam.

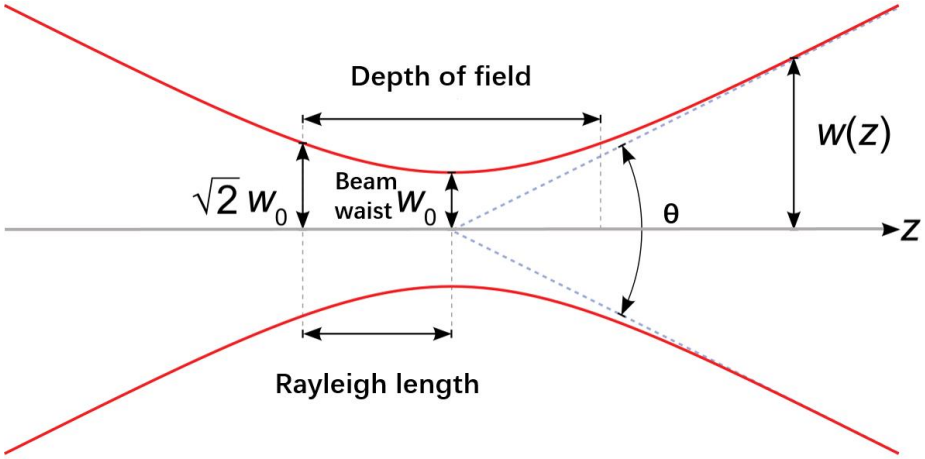

Figure 2.4: A typical Gaussian beam with the bean width $w(z)$ as a function of distance z along the beam.

2.3 Time-domain optical coherence tomography

In TD-OCT, the optical path length within a sample's structure is transferred to the time delay between back-reflected light by the axial displacement of a reference mirror. Figure 2.5a shows the schematic diagram of a typical TD-OCT system. The light beam from a low-coherence light source is split between a reference arm and a sample arm by a beam splitter. The scattered light from the sample and the reflected light from the reference mirror are collected by a single pixel photodiode, which is the interference signal (A-scan). Through the axial scan (depth scan) of the reference mirror, the depth profile of samples can be generated as shown in Figure 2.5b. 3D OCT data can be generated through the lateral scanning of samples.

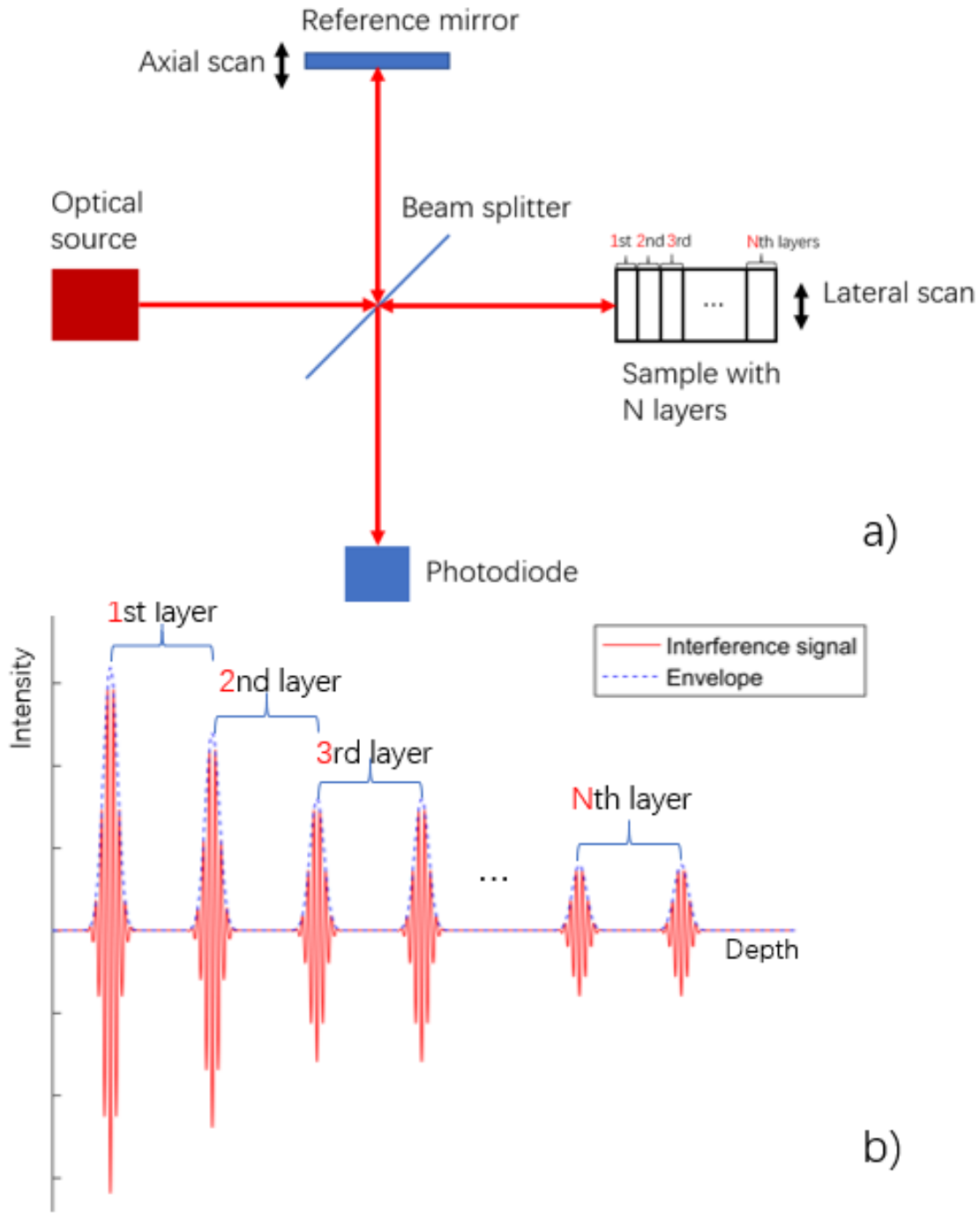

Figure 2.5: a) Schematic diagram of a typical TD-OCT system and b) one A-scan signal. Each peak in the A-scan signal represents the interface between adjacent layers within the target sample. This is known as the sample's depth profile.

On the photodetector side, the resultant light intensity I_e can be expressed as the superposition of light intensity I_r and I_s from the reference mirror and the sample object [45], considering the splitting ratios of the beam splitter:

$$I_e = k_r I_r + k_s I_s + 2\sqrt{k_r I_r k_s I_s} Re\big(\Gamma(\tau)\big) \tag{2.22}$$

, where k_r and k_s represents the splitting ratio of the beam splitter, $\Gamma(\tau)$ is called the complex degree of coherence and τ denotes the time delay between the sample and reference beams. τ can be expressed as $\tau = l/c$, where l is the optical path difference (OPD) between two beams. The complex degree of coherence can be expressed as a Gaussian function [58]:

$$\Gamma(\tau) = \exp\left[-\left(\frac{\pi \Delta f \tau}{2\sqrt{ln2}}\right)^2\right] \cdot \exp(-j2\pi f_0 \tau) \tag{2.23}$$

, where f_0 is the centre frequency of the optical source and Δf is its bandwidth. Therefore, the interferogram term ($2\sqrt{k_r I_r k_s I_s} Re\big(\Gamma(\tau)\big)$) of I_e can be simplified as $\mathrm{A}(l)\cos\big(\varphi_0 - \varphi(l)\big)$ and the time-domain A-scan signal can be expressed as a function of OPD l:

$$I_e(l) = I_{dc} + \mathrm{A}(l)\cos\big(\varphi_0 - \varphi(l)\big) \tag{2.24}$$

, where I_{dc} is the DC intensity received by the photodetector, $\mathrm{A}(l)$ is the analytical signal of the interferogram signal, φ_0 is a constant phase and $\varphi(l)$ is the phase delay between the sample and the reference beam. The envelope of this function can be extracted in order to present the inner structures of samples, as shown in Figure 2.5b. A Hilbert transform is normally applied to the interference signal to extract the envelope [59-63].

By moving the sample in both lateral directions, the 3D data of samples can be constructed. While effective, this method is very time-consuming compared with the later FD-OCT. Full-field time-domain OCT (FF-TD-OCT) was introduced by using a 2D detector to capture a series of *en-face* images through a single axial scan of a reference mirror. This means that multiple A-scans can be generated through one depth scan, which improves the scanning speed and efficiency of TD-OCT.

2.4 Fourier-domain optical coherence tomography

In FD-OCT, the interference signal from the system is acquired with a spectral detector. Compared to traditional TD-OCT, FD-OCT only needs the lateral scans to generate structural information of samples, as shown in Figure 2.6a. The power spectrums of back-reflected light are transfer to A-scans in the time-domain through an inverse Fourier-Transform (FT), as shown in Figure 2.6b.

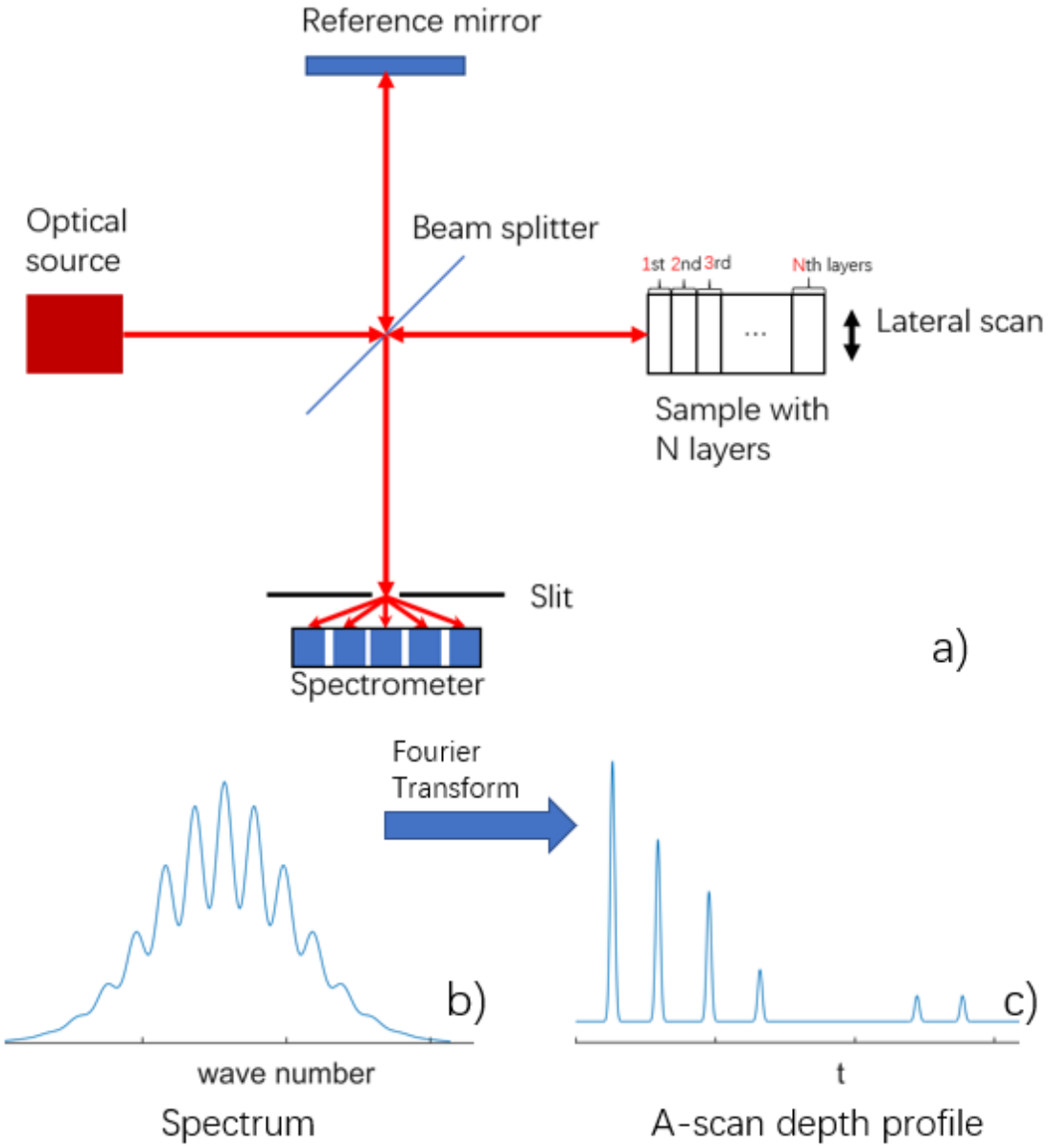

Figure 2.6: a) Schematic diagram of a typical FD-OCT system. b) Spectrum acquired from the spectrometer in the FD-OCT system. c) The corresponding A-scan signal after Fourier transform.

Unlike TD-OCT, FD-OCT uses a line camera based spectrometer as the detector, instead of a single photodiode. Figure 2.6a shows the schematic

diagram of a typical FD-OCT system. The spectral intensity at the spectrometer exit could be expressed as [45]:

$$I_e(v) = k_r I_r(v) + k_s I_s(v) + 2\sqrt{k_r I_r(v) k_s I_s(v)} Re\left(\mu(v) e^{i[\Phi_s(v) - \Phi_r(v)]}\right) \quad (2.25)$$

, where $I_r(v)$ and $I_s(v)$ are the spectral intensities of the reference beam and sample beam respectively; $\mu(v)$ is the spectral degree of coherence; $\Phi_s(v)$ and $\Phi_r(v)$ are the spectral phase of the sample wave and reference wave respectively. The spectral interferogram requires a Fourier transform to convert from the spectral-domain to the time-domain in order to present the A-scan depth profile.

The main advantage of FD-OCT technique is that no axial scan is needed and thus the data acquisition speed can be very fast. Meanwhile, FD-OCT has a large sensitivity advantage over TD-OCT, even in situations of low light levels, and high-speed detection [13,14].

2.5 Full-field optical coherence tomography

Full-field time-domain OCT is an improvement on traditional TD-OCT [17-22]. The first FF-TD-OCT system was presented in 1998, named full-field optical coherence microscopy (OCM) [23], which is a microscopy system combining optical low-coherence reflectometry (as shown in Figure 2.7). A 2D detector (CCD camera) was used instead of a single pixel photodiode. Most traditional OCT systems required 2D lateral scanning of samples. This strategy normally sacrifices the lateral resolution of images and requires a long scanning time for 3D measurement. By avoiding lateral scanning, FF-TD-OCT increases the acquisition speed of TD-OCT considerably and produces *en-face*

tomographic images with the lateral resolution only dependent on the optics and pixel size of the 2D detector.

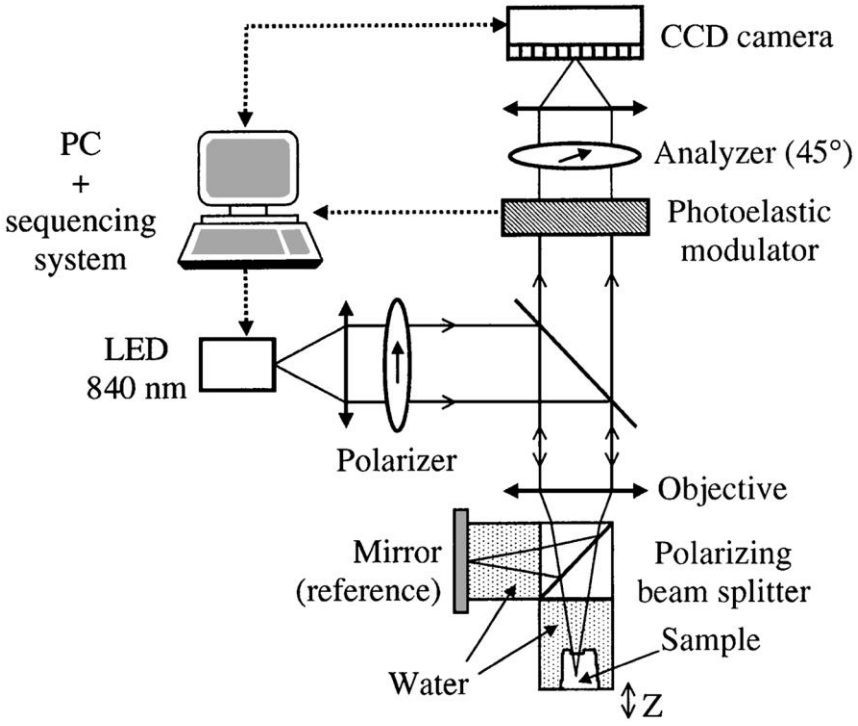

Figure 2.7: Overview of the OCM system and image of one point through the optical part. In reality, an *en-face* image is generated in parallel [19].

In histology, most biopsies are not suitable for frozen section analysis in routine clinical practice, since freezing and sectioning can lead to freezing artefacts, physical destruction and significant wastage of tissue. High resolution optical biopsy techniques for biological tissues are preferred, such as FF-TD-OCT, in order to overcome the drawbacks of frozen analysis and perform quick diagnoses. FF-TD-OCT has proven its ability to obtain cellular-level images from rat organs (heart, lung, liver skin, stomach, kidney, urinary bladder, prostate and testis); the normal histology of these organs can be recapitulated

by identifying various tissue microstructures from OCT image [64]. As for human tissue, both *ex vivo* and *in vivo*, including ocular tissue and human breast tissue were proven to be capable of being imaged by FF-OCT [65-75]. These experiments demonstrated that FF-OCT can be very crucial for clinicians and surgeons as it could allow them to evaluate the nature and architecture of biological tissue, which may be difficult to be observed by traditional histology procedures. 3D OCT data provides the clinicians the possibility of combining images in different orientations as well as complementary information of biological tissues. The volumetric reconstruction of 3D OCT images can even provide more information by analysing data in multiple angles.

In addition to biological applications, the capacity of FF-OCT has also been demonstrated in evaluating multi-layer polymer coating structures on pharmaceutical pellets. The coating thickness of pellets, the diameter of which is less than 1mm, can be precisely determined and their internal structure can clearly be resolved. The inexpensive setup and better spatial resolution, compared with other non-destructive analysis techniques, make FF-OCT a potential analytical tool for commercial applications in the pharmaceutical industry [31].

2.6 Other modalities of optical coherence tomography

Polarization-sensitive OCT

Polarization-sensitive OCT (PS-OCT) is an extension of OCT that uses the polarization properties of light to measure the depth-resolved phase retardation caused by biological tissue samples and calculate the birefringence of tissue [76,77]. Birefringence is an optical property of biological tissue, such as muscle,

cartilage and tendons, which provides a useful contrast mechanism in tissue. PS-OCT can reveal the structural information of birefringent turbid tissue while other OCT systems cannot. Figure 2.8 shows a typical PS-OCT system.

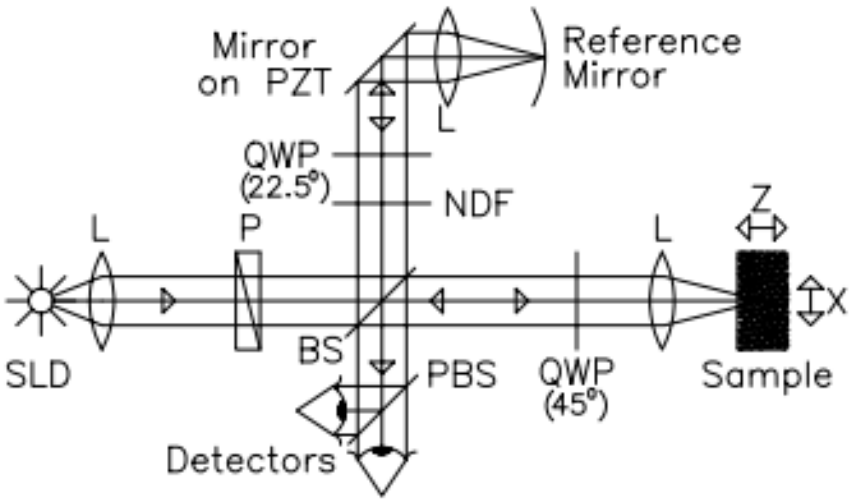

Figure 2.8: Schematic of the PS-OCT system. SLD: superluminescent diode, L: lens, P: polarizer, BS: beam splitter, QWP: quarter wave plate, NDF: neutral density filter, PBS: polarizing beam splitter, PZT: Piezoelectric transducer. [77]

Spectroscopic OCT

Spectroscopic OCT (SOCT) is able to perform cross-sectional tomographic and spectroscopic imaging and obtain spectral information of backscattering light in OCT systems [78,79]. This system uses a broadband light source and performs a depth-resolved spectroscopy study through time-frequency analysis. Imaging spectral absorption and spectral scattering can be achieved and thus used to detect either endogenous molecules or exogenous agents.

Doppler OCT

Doppler OCT (DOCT) aims to obtain high-resolution tomographic images of static and moving constituents in biological tissue, such as tissue structure and blood flow, simultaneously [79-85]. The segmentation and visualization of blood vessels from DOCT measurements is named OCT angiography. The principle DOCT is the combination of the Doppler effect and OCT system such that the speed of a moving particle in the samples can be determined by the measurement of the frequency shift of the backscattered light from this moving particle. In TD, the Doppler frequency shift is obtained by the analysis of the spectrum of measured A-scans. In FD, the Doppler frequency shift is obtained by the analysis of the spectral interferogram. Given the nature of non-invasion, non-destruction, high spatial resolution and velocity sensitivity, DOCT has demonstrated its great potential for biomedical and clinical research.

Optical coherence elastography

Optical coherence elastography (OCE) is another extension of OCT based on elastography, which maps the elastic properties and stiffness of soft tissue [86-91]. OCE can detect the cross-sectional biomechanical properties of biological tissue when mechanical stimulations are applied to the sample. The micrometre-scale resolution, millimetre-scale penetration and non-invasive 3D imaging ability give OCE great potential in the field of dermatology [86-91].

Swept-source OCT

Swept-source OCT (SS-OCT) has become popular in recent years. It is a variation of FD-OCT that obtains time-encoded spectral information by sweeping a narrow-bandwidth laser and using a point photo detector to detect the signal [95,96]. The main advantage of SS-OCT over traditional SD-OCT are

its higher scanning speed (~100k A-scans/s) without the reduction of sensitivity. The high robustness makes it perfect against sample motion and rapid lateral scanning which improves the detection efficiency of OCT. Another advantage is that the usage of a photodetector extends the penetration depth since the depth of scanning relies on the pixel size of spectrometer in camera-based SD-OCT. SS-OCT is regarded as the future of OCT technology and has been applied to *in vivo* ophthalmic diagnosis [95,97-100].

The following Table 2.1 shows an outline of different modalities of OCT.

Table 2.1: Different modalities of OCT and their advantages.

Modality of OCT	Description	Advantages
FF-TD-OCT	An improvement on traditional TD-OCT using 2D detector to capture *en-face* tomographic images.	By avoiding lateral scanning, FF-TD-OCT increases the acquisition speed of TD-OCT considerably and produces en-face tomographic images.
PS-OCT	One kind of functional OCT that use polarization properties of light to measure the depth-resolved phase retardation of biological tissues and calculate the birefringence of tissues.	PS-OCT can reveal the structural information of birefringent turbid tissue while other OCT systems cannot.
SOCT	One kind of functional OCT that perform spectroscopic imaging	SOCT system performs a depth-resolved spectroscopy study and achieves spectral absorption and spectral scattering information to detect either endogenous molecules or exogenous agents.
DOCT	One kind of functional OCT that combine the Doppler effect and OCT system to measure moving particle.	DOCT is able to obtain high-resolution tomographic images of static and moving constituents in biological tissue, such as tissue structure and blood flow, and is named OCT angiography.
OCE	One kind of functional OCT to measure elastic properties.	OCE is able to map the elastic properties and stiffness of soft tissue and has great potential in the field of dermatology.
SS-OCT	A time-encoded spectral-domain OCT using tunable swept light source.	High scanning speed (~100k A-scan/s); High sensitivity (>100dB); High detection efficiency.

Reference

1. R. C. Youngquist, S. Carr, and D. E. N. Davies, “Optical coherence domain reflectometry: A new optical evaluation technique,” Optics Letter 12, 158–160 (1987).

2. K. Takada, I. Yokohama, K. Chida, and J. Noda, “New measurement system for fault location in optical waveguide devices based on an interferometric technique,” Applied Optics 26, 1603–1606 (1987).

3. D. Huang, E. A. Swanson, C. P. Lin, J. S. Schuman, W. G. Stinson, W. Chang, M. R. Hee, T. Flotte, K. Gregory, C. A. Puliafito, and J. G. Fujimoto, “Optical coherence tomography,”. Science 254(5035), 1178 (1991).

4. A. F. Fercher, C. K. Hitzenberger, W. Drexler, G. Kamp, and H. Sattmann, “In vivo optical coherence tomography,” American Journal of Ophthalmology 116, 113–114 (1993).

5. E. A. Swanson, J. A. Izatt, C. P. Lin, J. G. Fujimoto, J. S. Schuman, M. R. Hee, D. Huang, and C. A. Puliafito, "In vivo retinal imaging by optical coherence tomography," Opt. Lett. 18, 1864-1866 (1993)

6. J. M. Schmitt, M. Yadlowsky, and R. F. Bonner, “Subsurface imaging if living skin with optical coherence tomography,” Dermatology 191, 93–98 (1995).

7. J. Welzel, E. Lankenau, R. Birngruber and R. Engelhardt, “Optical coherence tomography of the human skin,” Journal of the American Academy of Dermatology, 37(6), 958-963 (1997).

8. G. J. Tearney, M. E. Brezinski, B. E. Bouma, M. R. Hee, J. F. Southern, and J. G. Fujimoto, "Determination of the refractive index of highly scattering human tissue by optical coherence tomography," Optics Letters 20, 2258-2260 (1995).

9. G. J. Tearney, M. E. Brezinski, B. E. Bouma, S. A. Boppart, C. Pitris, J. F. Southern and J. G. Fujimoto, “In vivo endoscopic optical biopsy with optical coherence tomography,” Science 276(5321), 2037-2039 (1997).

10. J. G. Fujimoto, M. E. Brezinski, G. J. Tearney, S. A. Boppart, B. E. Bouma, M. R. Hee, J. F. Southern, and E. A. Swanson, “Optical biopsy and imaging using optical coherence tomography,” Nature Medicine 1, 970–972 (1995).

11. A. F. Fercher, C. K. Hitzenberger, G. Kamp and S. Y. El-Zaiat, “Measurement of intraocular distances by backscattering spectral interferometry,” Optics communications 117(1-2), 43-48(1995).

12. M. Wojtkowski, R. Leitgeb, A. Kowalczyk, T. Bajraszewski and A. F. Fercher, "In vivo human retinal imaging by Fourier domain optical coherence tomography," Journal of Biomedical Optics 7(3), (2002)

13. R. Leitgeb, C. K. Hitzenberger, and A. F. Fercher, “Performance of fourier domain vs. time domain optical coherence tomography,” Optics express 11(8), 889-894 (2003).

14. J. F. De Boer, B. Cense, B. H. Park, M. C. Pierce, G. J. Tearney, and B. E. Bouma, “Improved signal-to-noise ratio in spectral-domain compared with time-domain optical coherence tomography,” Optics letter 28(21), 2067-

2069 (2003).

15. M. A. Choma, M. V. Sarunic, C. Yang, J. A. Izatt, “Sensitivity advantage of swept source and Fourier domain optical coherence tomography,” Optics Express 11, 2183–2189 (2003).

16. J. Barrick, A. Doblas, P. R. Sears, L. E. Ostrowski and A. L. Oldenburg, “High-sensitivity supercontinuum-based parallel line-field optical coherence tomography with 1 million A-lines/s,” In SPIE BiOS (pp. 100531S-100531S). International Society for Optics and Photonics (2017).

17. A. Dubois, and A. C. Boccara, Full-field optical coherence tomography (Springer Berlin Heidelberg, 2008), Optical Coherence Tomography, 565-591.

18. H. D. Ford, and P. T. Ralph, "Full-field optical coherence tomography." (2005).

19. A. Dubois, L. Vabre, A. C. Boccara, and E. Beaurepaire, “High-resolution full-field optical coherence tomography with a Linnik microscope,” Applied optics 41(4), 805-812 (2002).

20. A. Dubois, K. Grieve, G. Moneron, R. Lecaque, L. Vabre, and C. Boccara, “Ultrahigh-resolution full-field optical coherence tomography,” Applied optics 43(14), 2874-2883 (2004).

21. M. Akiba, K. P. Chan, and N. Tanno. "Full-field optical coherence tomography by two-dimensional heterodyne detection with a pair of CCD cameras," Optics letters 28(10), 816-818 (2003).

22. A. Dubois, G. Moneron, K. Grieve, and A. C. Boccara, "Three-dimensional cellular-level imaging using full-field optical coherence tomography," Physics in medicine and biology 49(7), 1227 (2004).

23. E. Beaurepaire, A. C. Boccara, M. Lebec, L. Blanchot, and H. Saint-Jalmes, "Full-field optical coherence microscopy," Optics Letter 23, 244-246 (1998)

24. R. F. Spaide, J. M. Klancnik and M. J. Cooney, “Retinal vascular layers imaged by fluorescein angiography and optical coherence tomography angiography,” JAMA ophthalmology 133(1), 45-50 (2015).

25. Y. Jia, S. T. Bailey, D. J. Wilson, O. Tan, M. L. Klein, C. J. Flaxel, B. Potsaid, J. J. Liu, C. D. Lu, M. F. Kraus and J. G. Fujimoto, “Quantitative optical coherence tomography angiography of choroidal neovascularization in age-related macular degeneration,” Ophthalmology 121(7), 1435-1444 (2014).

26. Y. Jia, S. T. Bailey, T. S. Hwang, S. M. McClintic, S. S. Gao, M. E. Pennesi, C. J. Flaxel, A. K. Lauer, D. J. Wilson, J. Hornegger and J. G. Fujimoto, “Quantitative optical coherence tomography angiography of vascular abnormalities in the living human eye,” Proceedings of the National Academy of Sciences 112(18), E2395-E2402 (2015).

27. H. Jia, F. Abtahian, A. D. Aguirre, S. Lee, S. Chia, H. Lowe, K. Kato, T. Yonetsu, R. Vergallo, S. Hu and J. Tian, “In vivo diagnosis of plaque erosion and calcified nodule in patients with acute coronary syndrome by intravascular optical coherence tomography,” Journal of the American College of Cardiology 62(19), 1748-1758 (2013).

28. M. D. Tibbetts, E. Reichel and A. J. Witkin, “Vision loss after intravitreal ocriplasmin: correlation of spectral-domain optical coherence tomography and electroretinography,” JAMA ophthalmology 132(4), 487-490 (2014).

29. S. Zhong, Y. C. Shen, L. Ho, R. K. May, J. A. Zeitler, M. Evans, P. F. Taday, M. Pepper, T. Rades, K. C. Gordon and R. Müller, “Non-destructive quantification of pharmaceutical tablet coatings using terahertz pulsed imaging and optical coherence tomography,” Optics and Lasers in Engineering 49(3), 361-365 (2011).

30. Y. Dong, H. Lin, V. Abolghasemi, L. Gan, J. A. Zeitler and Y. C. Shen, “Investigating intra-tablet coating uniformity with spectral-domain optical coherence tomography,” Journal of pharmaceutical sciences 106(2), 546-553 (2017).

31. C. Li, J. A. Zeitler, Y. Dong, and Y. C. Shen. "Non-Destructive Evaluation of Polymer Coating Structures on Pharmaceutical Pellets Using Full-Field Optical Coherence Tomography," Journal of pharmaceutical sciences 103(1), 161-166 (2014).

32. H. Lin, Y. Dong, D. Markl, Z. Zhang, Y. Shen and J. A. Zeitler, “Pharmaceutical film coating catalogue for spectral-domain optical coherence tomography,” Journal of Pharmaceutical Sciences 106(10), 3171-3176 (2017)

33. H. Lin, Y. Dong, Y. Shen and J. A. Zeitler, “Quantifying pharmaceutical film coating with optical coherence tomography and terahertz pulsed imaging: an evaluation,” Journal of pharmaceutical sciences 104(10), 3377-3385

(2015).

34. H. Lin, Y. Dong, C. Pei, B. M. Williams, D. Markl, Y. Zheng, J. A. Elliott, Y. Shen and J. A. Zeitler, “Studying the pharmaceutical film coating process with terahertz sensing, optical coherence tomography and numerical modelling,” In Infrared, Millimeter, and Terahertz waves (IRMMW-THz), 2016 41st International Conference on (pp. 1-2). IEEE.

35. H. Lin, Y. Dong, D. Markl, B. M. Williams, Y. Zheng, Y. Shen and J. A. Zeitler, “Measurement of the Intertablet Coating Uniformity of a Pharmaceutical Pan Coating Process With Combined Terahertz and Optical Coherence Tomography In-Line Sensing,” Journal of pharmaceutical sciences 106(4), 1075-1084 (2017).

36. S. Lawman, J. Zhang, B. M. Williams, Y. Zheng and Y. C. Shen, “Applications of optical coherence tomography in the non-contact assessment of automotive paints,” In Optical Measurement Systems for Industrial Inspection X (Vol. 10329, p. 103290J). International Society for Optics and Photonics (2017).

37. S. Lawman, B. M. Williams, J. Zhang, Y. C. Shen and Y. Zheng, “Scan-Less Line Field Optical Coherence Tomography, with Automatic Image Segmentation, as a Measurement Tool for Automotive Coatings,” Applied Sciences 7(4), 351 (2017).

38. N. Zhang, C. Wang, Z. Sun, H. Mei, W. Huang, L. Xu, L. Xie, J. Guo, Y. Yan, Z. Li and X. Xu, “Characterization of automotive paint by optical coherence tomography,” Forensic science international 266, 239-244 (2016).

39. Y. Dong, S. Lawman, Y. Zheng, D. Williams, J. Zhang and Y. C. Shen, “Nondestructive analysis of automotive paints with spectral domain optical coherence tomography,” Applied optics 55(13), 3695-3700 (2016).

40. C. Wang, N. Zhang, Z. Sun, Z. Li, Z. Li, and X. Xu, “Recovering hidden sub-layers of repainted automotive paint by 3D optical coherence tomography,” Australian Journal of Forensic Sciences, 1-9 (2017).

41. M. Lenz, C. Mazzon, C. Dillmann, N. C. Gerhardt, H. Welp, M. Prange and M. R. Hofmann, “Spectral Domain Optical Coherence Tomography for Non-Destructive Testing of Protection Coatings on Metal Substrates,” Applied Sciences 7(4), 364 (2017).

42. S. H. Kim, J. H. Kim and S. W. Kang, “Nondestructive defect inspection for LCDs using optical coherence tomography,” Displays 32(5), 325-329 (2011).

43. N. H. Cho, U. Jung, S. Kim and J. Kim, “Non-destructive inspection methods for leds using real-time displaying optical coherence tomography,” Sensors 12(8), 10395-10406 (2012).

44. N. H. Cho, K. Park, J. Y. Kim, Y. Jung and J. Kim, “Quantitative assessment of touch-screen panel by nondestructive inspection with three-dimensional real-time display optical coherence tomography,” Optics and Lasers in Engineering 68, 50-57 (2015).

45. A. F. Fercher, W. Drexler, C. K. Hitzenberger, and T. Lasser, “Optical coherence tomography-principles and applications,” Reports on progress in physics 66(2), 239 (2003).

46. X. Zhu, Y. Liang, Y. Mao, Y. Jia, Y. Liu and G. Mu, “Analyses and calculations of noise in optical coherence tomography systems,” Frontiers of Optoelectronics in China 1(3), 247-257 (2008).

47. J. A. Izatt, M. A. Choma and A. H. Dhalla, “Theory of optical coherence tomography,” Optical Coherence Tomography: Technology and Applications, 65-94 (2015).

48. P. R. Saulson, “Thermal noise in mechanical experiments,” Physical Review D 42(8), 2437 (1990).

49. T. B. Gabrielson, “Mechanical-thermal noise in micromachined acoustic and vibration sensors,” IEEE transactions on Electron Devices 40(5), 903-909 (1993).

50. T. J. Hofler and S. L. Garrett, “Thermal noise in a fiber optic sensor,” The Journal of the Acoustical Society of America 84(2), 471-475 (1988).

51. W. B. Davenport and W. L. Root, “An introduction to the theory of random signals and noise,” (Vol. 159). New York: McGraw-Hill (1958).

52. R. H. Barker, “Information Transmission, Modulation, and Noise,” Physics Bulletin 11(2), 55 (1960).

53. A. M. Rollins and J. A. Izatt, "Optimal interferometer designs for optical coherence tomography," Optics Letters 24, 1484-1486 (1999)

54. B. Povazay, K. Bizheva, A. Unterhuber, B. Hermann, H. Sattmann, A. F. Fercher, W. Drexler, A. Apolonski, W. J. Wadsworth, J. C. Knight and P. S.

J. Russell, “Submicrometer axial resolution optical coherence tomography,” Optics letters 27(20), pp.1800-1802 (2002).

55. A. B. Miguel and C. G. Julio, "Ince–Gaussian beams," Optics Letters 29, 144-146 (2004)

56. F. Pampaloni and J. Enderlein, “Gaussian, hermite-gaussian, and laguerre-gaussian beams: A prime,” arXiv preprint physics/0410021 (2004).

57. L. Mandel, and E. Wolf, Optical Coherence and Quantum Optics. Cambridge: Cambridge University Press. ISBN 0-521-41711-2. Chapter 5, "Optical Beams,” 267 (1995).

58. A. F. Fercher, K. Mengedoht, and W. Werner, “Eye-length measurement by interferometry with partially coherent light,” Optics letters 13(3), 186-188 (1988).

59. Z. K. Peng, W. T. Peter and F. L. Chu, “An improved Hilbert–Huang transform and its application in vibration signal analysis,” Journal of sound and vibration 286(1), 187-205 (2005).

60. D. Benitez, P. A. Gaydecki, A. Zaidi and A. P. Fitzpatrick, “The use of the Hilbert transform in ECG signal analysis,” Computers in biology and medicine 31(5), 399-406 (2001).

61. K. G. Larkin, “Efficient nonlinear algorithm for envelope detection in white light interferometry,” JOSA A 13(4), 832-843 (1996).

62. S. Schimmel and L. Atlas, “Coherent envelope detection for modulation

filtering of speech," In Acoustics, Speech, and Signal Processing, 2005. Proceedings. (ICASSP'05). IEEE International Conference on (Vol. 1, pp. I-221). IEEE.

63. J. Dugundji, "Envelopes and pre-envelopes of real waveforms," IRE Transactions on Information Theory 4(1), 53-57 (1958).

64. M. Jain, N. Shukla, M. Manzoor, S. Nadolny, and S. Mukherjee, "Modified full-field optical coherence tomography: A novel tool for rapid histology of tissues," Journal of pathology informatics, 2 (2011).

65. A. Latrive and A. C. Boccara, "In vivo and in situ cellular imaging full-field optical coherence tomography with a rigid endoscopic probe," Biomedical Optics Express 2, 2897-2904 (2011)

66. O. Assayag, K. Grieve, B. Devaux, F. Harms, J. Pallud, Chretien, F., C. Boccara, and P. Varlet, "Imaging of non-tumorous and tumorous human brain tissues with full-field optical coherence tomography," NeuroImage: Clinical 2, 549-557 (2013).

67. O. Assayag, M. Antoine, B. Sigal-Zafrani, M. Riben, F. Harms, A. Burcheri, K. Grieve, E. Dalimier, B. Le Conte de Poly, and C. Boccara, "Large field, high resolution full-field optical coherence tomography: a pre-clinical study of human breast tissue and cancer assessment," Technology in cancer research & treatment 13(5), 455-468 (2014).

68. K. Grieve, M. Paques, A. Dubois, J. Sahel, C. Boccara, and J.F. Le Gargasson, "Ocular tissue imaging using ultrahigh-resolution, full-field

optical coherence tomography," Investigative ophthalmology & visual science, 45(11), 4126-4131 (2004).

69. S. Guerrieri, G. Di Maggio, M. Pisa, F. Vitali, R. Santangelo, S. Medaglini, L. Moiola, U. Del Carro, V. Martinelli, G. Comi, and L. Leocani, "Optical Coherence Tomography, full-field Visual Evoked Potentials and multifocal Visual Evoked Potentials to monitor and predict Optic Nerve damage and Clinical Outcome after Acute Optic Neuritis in Clinical Practice (P5. 201)," Neurology, 88(16 Supplement), P5-201 (2017).

70. L. van Manen, P. L. Stegehuis, A. Fariña-Sarasqueta, L. M. de Haan, J. Eggermont, B. A. Bonsing, H. Morreau, B. P. Lelieveldt, C. J. van de Velde, A. L. Vahrmeijer, and J. Dijkstra, "Validation of full-field optical coherence tomography in distinguishing malignant and benign tissue in resected pancreatic cancer specimens," PloS one, 12(4), p.e0175862 (2017).

71. S. Nandy, M. Sanders, and Q. Zhu, "Classification of human ovarian tissue using full field optical coherence tomography," SPIE BiOS. International Society for Optics and Photonics, 2017.

72. V. Mazlin, E. Dalimier, K. Grieve, K. Irsch, J. Sahel, M. Fink, and C. Boccara, "Non-Contact Full-Field Optical Coherence Tomography: A Step Towards In-Vivo Cellular-Level Imaging of the Human Cornea," Imaging Systems and Applications. Optical Society of America, 2016.

73. K. Grieve, K. Mouslim, O. Assayag, E. Dalimier, F. Harms, A. Bruhat, C. Boccara, and M. Antoine. "Assessment of sentinel node biopsies with full-field optical coherence tomography," Technology in cancer research &

treatment 15(2), 266-274 (2016).

74. J. Lopater, P. Colin, F. Beuvon, M. Sibony, E. Dalimier, F. Cornud, and N.B. Delongchamps. "Real-time cancer diagnosis during prostate biopsy: ex vivo evaluation of full-field optical coherence tomography (FFOCT) imaging on biopsy cores," World journal of urology 34(2), 237-243 (2016).

75. I. T. Peters, P. L. Stegehuis, R. Peek, F. L. Boer, E. W. van Zwet, J. Eggermont, J. R. Westphal, P. J. Kuppen, J. B. Trimbos, C. G. Hilders, and B. P. Lelieveldt, "Noninvasive detection of metastases and follicle density in ovarian tissue using full-field optical coherence tomography," Clinical Cancer Research 22(22), 5506-5513 (2016).

76. M. R. Hee, D. Huang, E. A. Swanson, and J. G. Fujimoto, “Polarization sensitive low coherence reflectometer for birefringence characterization and ranging,” Journal of the Optical Society of America. B 9, 903–908 (1992)

77. J. F. de Boer, S. M. Srinivas, A. Malekafzali, Z. Chen, and J. S. Nelson, “Imaging thermally damaged tissue by polarization sensitive optical coherence tomography,” Optics Express 3, 212–218 (1998)

78. U. Morgner, W. Drexler, F. X. Kärtner, X. D. Li, C. Pitris, E. P. Ippen, and J. G. Fujimoto, "Spectroscopic optical coherence tomography," Optics Letter 25, 111-113 (2000)

79. M. D. Kulkarni and J. A. Izatt, “Spectroscopic optical coherence tomography,” In Lasers and Electro-Optics, 1996. CLEO'96., Summaries of papers presented at the Conference on (pp. 59-60). IEEE.

80. R. A. Leitgeb, R.M. Werkmeister, C. Blatter, and L. Schmetterer, "Doppler optical coherence tomography," Progress in retinal and eye research 41, 26-43 (2014).

81. Z. Chen, and J. Zhang. "Doppler optical coherence tomography," Optical Coherence Tomography: Technology and Applications, 1289-1320 (2015).

82. R. A. Leitgeb, L. Schmetterer, W. Drexler, A. F. Fercher, R. J. Zawadzki and T. Bajraszewski, “Real-time assessment of retinal blood flow with ultrafast acquisition by color Doppler Fourier domain optical coherence tomography,” Optics Express 11(23), 3116-3121 (2003).

83. S. Yazdanfar, A. M. Rollins and J. A. Izatt, “In vivo imaging of human retinal flow dynamics by color Doppler optical coherence tomography,” Archives of ophthalmology 121(2), 235-239 (2003).

84. V. Westphal, S. Yazdanfar, A. M. Rollins and J. A. Izatt, “Real-time, high velocity-resolution color Doppler optical coherence tomography,” Optics Letters, 27(1), 34-36 (2002).

85. M. D. Kulkarni, T. G. van Leeuwen, S. Yazdanfar and J. A. Izatt, “Velocity-estimation accuracy and frame-rate limitations in color Doppler optical coherence tomography,” Optics Letters 23(13), 1057-1059 (1998).

86. C. Sun, B. Standish, and V.X. Yang. "Optical coherence elastography: current status and future applications," Journal of biomedical optics 16(4), 043001-043001 (2011).

87. B. F. Kennedy, X. Liang, S. G. Adie, D. K. Gerstmann, B. C. Quirk, S. A.

Boppart, and D. D. Sampson, "In vivo three-dimensional optical coherence elastography," Optics express 19(7), 6623(2011).

88. R. K. Wang, S. Kirkpatrick and M. Hinds, “Phase-sensitive optical coherence elastography for mapping tissue microstrains in real time,” Applied Physics Letters 90(16), 164105 (2007).

89. B. F. Kennedy, K. M. Kennedy, A. L. Oldenburg, S. G. Adie, S. A. Boppart and D. D. Sampson, “Optical coherence elastography,” Optical Coherence Tomography: Technology and Applications, 1007-1054 (2015).

90. H. J. Ko, W. Tan, R. Stack and S. A. Boppart, “Optical coherence elastography of engineered and developing tissue,” Tissue engineering, 12(1), 63-73 (2006).

91. B. F. Kennedy, K. M. Kennedy and D. D. Sampson, “A review of optical coherence elastography: fundamentals, techniques and prospects,” IEEE Journal of Selected Topics in Quantum Electronics, 20(2), 272-288 (2014).

92. X. Liang, and S. A. Boppart, "Biomechanical properties of in vivo human skin from dynamic optical coherence elastography," IEEE Transactions on Biomedical Engineering 57(4), 953-959 (2010).

93. J. Welzel, "Optical coherence tomography in dermatology: a review," Skin Research and Technology 7(1), 1-9 (2001).

94. Li, C., Guan, G., Reif, R., Huang, Z. and Wang, R.K., 2012. Determining elastic properties of skin by measuring surface waves from an impulse mechanical stimulus using phase-sensitive optical coherence tomography.

Journal of The Royal Society Interface, 9(70), pp.831-841.

95. Y. Yasuno, VD. Madjarova, S. Makita, M. Akiba, A. Morosawa, C. Chong, T. Sakai, KP. Chan, M. Itoh, and T. Yatagai, "Three-dimensional and high-speed swept-source optical coherence tomography for in vivo investigation of human anterior eye segments," Optics Express 13, 10652-10664 (2005).

96. M. A. Choma, K. Hsu, and J. A. Izatt. "Swept source optical coherence tomography using an all-fiber 1300‐nm ring laser source." Journal of biomedical optics 10(4), 044009-044009 (2005).

97. D. Ferrara, K. J. Mohler, N. Waheed, M. Adhi, J. J. Liu, I. Grulkowski, M. F. Kraus, C. Baumal, J. Hornegger, J. G. Fujimoto, J. S. Duker, "En face enhanced-depth swept-source optical coherence tomography features of chronic central serous chorioretinopathy," Ophthalmology 121(3), 719-726 (2014).

98. W. Choi, E. M. Moult, N. K. Waheed, M. Adhi, B. Lee, C. D. Lu, E. Talisa, V. Jayaraman, P. J. Rosenfeld, J. S. Duker, and J. G. Fujimoto, “Ultrahigh-speed, swept-source optical coherence tomography angiography in nonexudative age-related macular degeneration with geographic atrophy,” Ophthalmology 122(12), 2532-2544 (2015).

99. C. D. Lu, M. F. Kraus, B. Potsaid, J. J. Liu, W. Choi, V. Jayaraman, A. E. Cable, J. Hornegger, J. S. Duker, and J. G. Fujimoto, "Handheld ultrahigh speed swept source optical coherence tomography instrument using a MEMS scanning mirror," Biomedical Optics Express 5, 293-311 (2014).

100. Y. Li, C. D. Lu, Y. Jia, B. Lee, M. F. Kraus, J. Hornegger, J. G. Fujimoto, and D. Huang, “Anterior segment angiography with 1050 nm swept-source optical coherence tomography,” Investigative Ophthalmology & Visual Science 56(7), 4512-4512 (2015).

Chapter 3. Implementation of FF-TD-OCT configurations

As an improvement of traditional TD-OCT system, FF-TD-OCT utilises 2D detector, such as charge-coupled device (CCD) or complementary metal-oxide semiconductor (CMOS) camera, instead of a single photodiode to acquire interference signals between a reference mirror and samples from OCT system. As discussed in the previous chapter, FF-TD-OCT inherits the advantages of traditional TD-OCT including high spatial resolution and also has a higher scanning speed and efficiency in acquiring 3D OCT data by capturing a series of *en-face* images through depth scan [1-3]. The full-field illumination setup avoids the mechanical motion of samples in lateral direction which is crucial for long-time measurement or tissue samples *in vivo*. This chapter presents the configuration of our FF-TD-OCT system as well as its imaging performance including the axial and lateral resolution.

3.1 Description of the experimental FF-TD-OCT system

The schematic diagram of the built FF-TD-OCT setup is presented in Figure 3.1. The light beam from light source is split between a reference arm and a sample arm by a non-polarizing 50/50 beam splitter. The collimated light beam after lens (L1) illuminates both the sample and the reference mirror. The scattered light from the sample and the reflected light from the reference mirror are collected and then focused onto a 2D detector using a pair of achromatic lenses (L2 and L3). Interference fringes occur when the difference in optical path length between the sample and reference arm is within the coherence

length. A set of *en-face* images of a sample is captured by the high-speed 2D detector. Lens L2 (Focus length: 50mm) and L3 are placed such that the distance between them is the sum of their focus length and the 2D detector is placed at the focus point of the lens (L3). The magnification power is given by the ratio of the focus lengths of L2 and L3. So L3 has the choices of focus length from 50 mm to 250 mm to have the magnification power from 1 to 5. The magnification power has effect on the final lateral resolution of *en-face* images, since the lateral resolution should at least two times of image pixel size. To be noticed, the higher magnification of this setup is possible but it requires an increasing distance among L2, L3 and 2D detector, which is limited by the length of optic table.

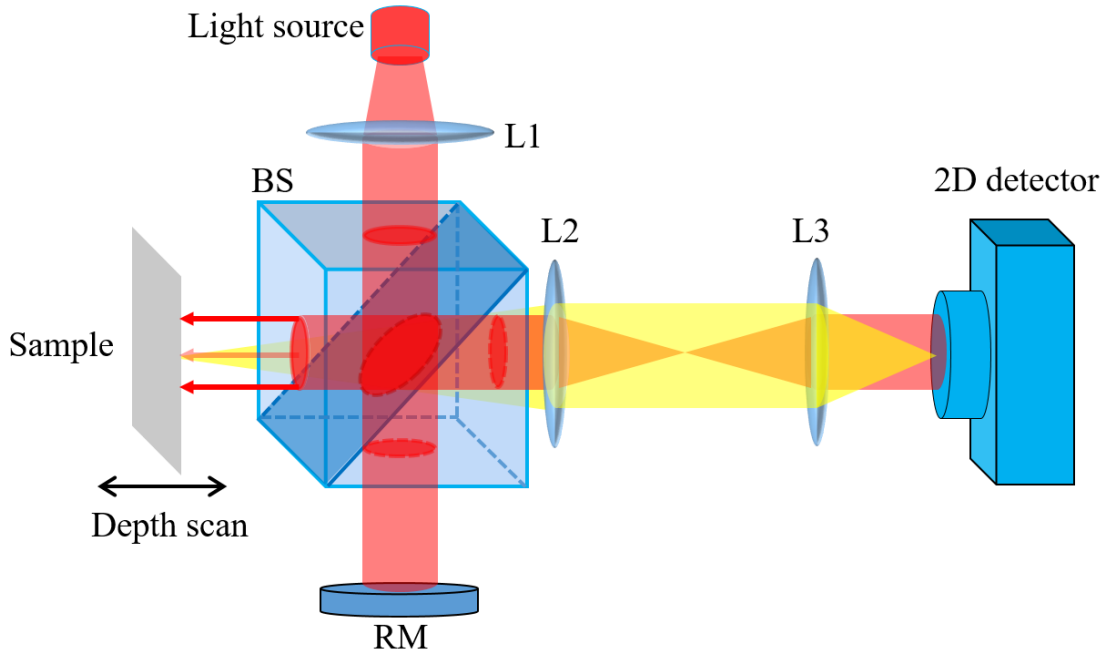

Figure 3.1: Schematic of our FF-OCT system showing the beam splitter (BS), plano-convex lenses (L1, L2, L3).

Figure 3.2 shows the operation procedure of our FF-TD-OCT system. A reference A-scan signal between two identical mirrors was recorded by the 2D detector firstly (the same mirror was placed at sample arm and applied depth scan). In the process of data acquisition, the reference mirror is fixed at the focal point of L2, the samples were fixed on a motorized stage for depth scan and the 2D detector can collect *en-face* images simultaneously. Then the 3D OCT data cube was stored in 16-bit '.mat' format and upload to operating computer. In order to recover the sample depth profile, each A-scan was convoluted with the reference A-scan signal and the Hilbert transform [4] was applied to it to remove the oscillation waves and extract the envelope. Further data processing could be applied to the 3D depth profile data of samples to get the structural information, such as layer thickness and particle size, number within samples.

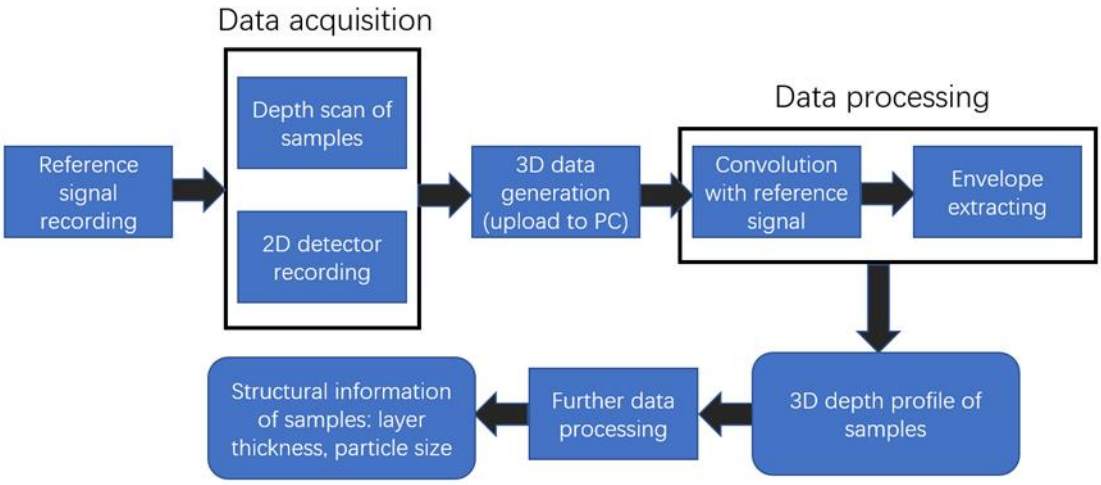

Figure 3.2: The flow chart of the operation of our FF-TD-OCT system.

3.2 System components

3.2.1 Light source

The white light illumination used is a Quartz Tungsten-Halogen light source band-passing through a filter for imaging thin layers or surface structures. Figure 3.3 shows the power spectrum of the white light source through a band-passing filter (FGS900, 315-700nm).

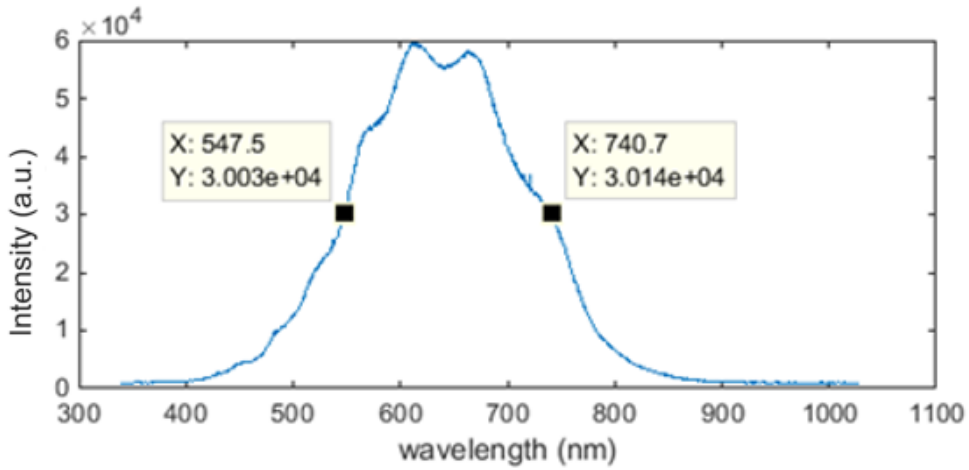

Figure 3.3 : Power spectrum of the white light Tungsten-Halogen light source through a band-passing filter (315 - 700nm). The central wavelength is λ_0 = 613 nm and the bandwidth is $\Delta\lambda$ = 185nm.

Another light source used was a Near-infrared light emitting diode (LED). In addition to its long central wavelength and broad-band bandwidth, it also provides a large penetration depth for layer structural measurement beneath sample surfaces. Figure 3.4 shows its power spectrum.

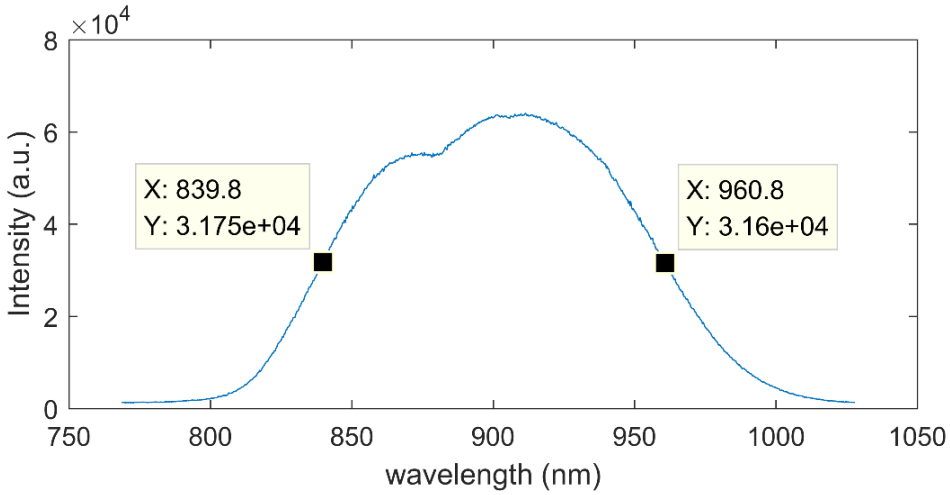

Figure 3.4**:** Power spectrum of the infrared light source. The central wavelength is λ_0 = 900 nm and the bandwidth is $\Delta\lambda$ = 121nm.

3.2.2 CMOS camera

The high frame rate camera used in our experiments is Point Grey Grasshopper 3 USB 3.0 camera GS3-U3-23S6M-C. It has the maximum pixel of 1920x1200 with the pixel size of 5.86μm. It can provide a 10-bit or 12-bit mono formatted digital data recording and sense a width spectral from 320nm to 880nm. The maximum frame rate is 162 fps at full pixel number but the frame rate can go higher when the acquired pixel number is smaller.

3.2.3 Motorized stage

The single-axis motorized stage used in our FF-TD-OCT system is a linear piezo positioning stage (Physik Instrumente, LPS-65) with a high precision and load capacity. The unidirectional repeatability can be down to 0.005μm and the maximum load capacity is 2kg which is sufficient to load our experimental samples. The piezo driven motor steps with a sub-nanometre resolution and

thus ensure a smooth and high accurate movement during the depth scan of demanded samples.

3.3 Performance of FF-TD-OCT

3.3.1 Lateral resolution

In theory, the lateral resolution of OCT system is defined by the FWHM of the beam waist [5-7]. In an optical imaging system, the 1951 USAF resolution test target is normally used to measure the resolution. The largest bar cannot be resolved by an optical imaging system is its resolving power. Figure 3.5a shows a standard 1951 USAF resolution target and Figure 3.5b shows the *en-face* image by our FF-TD-OCT system. The largest bar cannot be resolved is group 7, element 6, which 2.2μm width. Therefore, our system lateral resolution is 4.4μm.

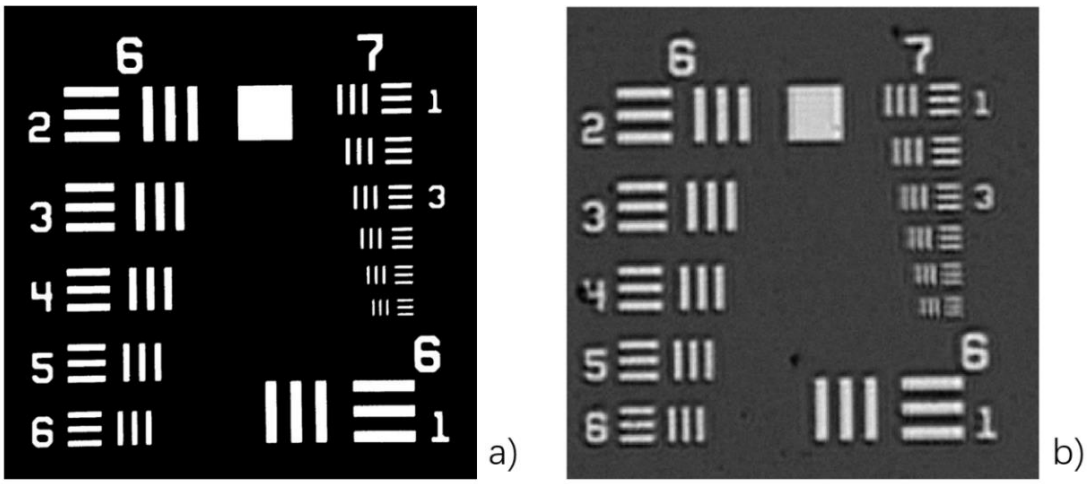

Figure 3.5: a) An image of 1951 USAF resolution target with the element group of 6 and 7. b) An OCT *en-face* image of USAF resolution target measured by our FF-TD-OCT system.

3.3.2 Axial resolution

As mentioned in the Chapter 2, section 2.2.3, the axial resolution is determined by the central wavelength and bandwidth of light source [8,9]. In practice, the FWHM of the interference signal obtained from OCT system can be regarded as the axial resolution of this OCT system. Figure 3.6 shows the axial resolution under two light sources FF-TD-OCT system. In the near-infrared system, the achieved axial resolution is 3.9μm. In the white light illumination system, the achieved axial resolution is 1.6μm.

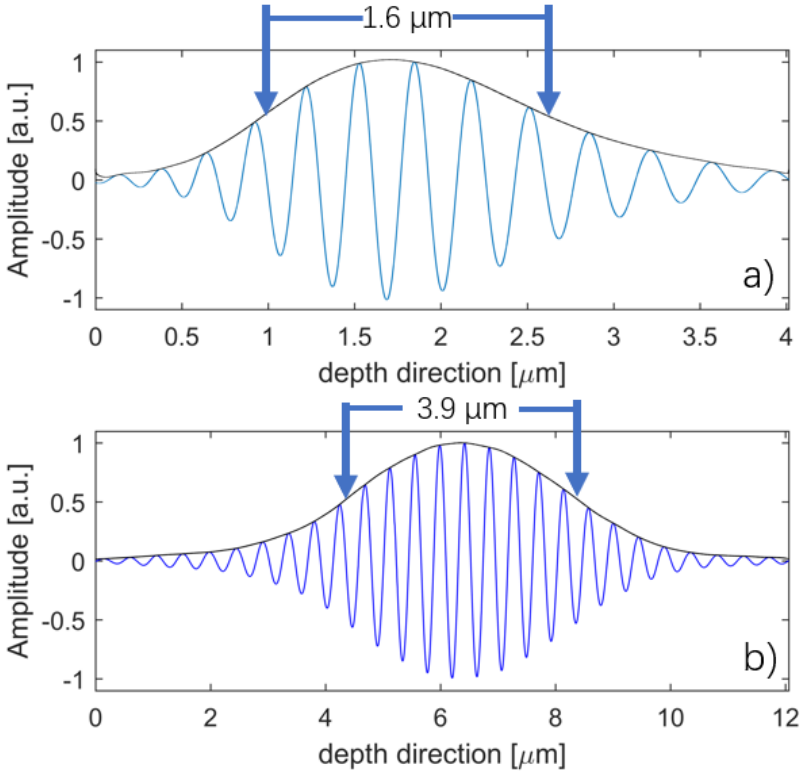

Figure 3.6: a) The FWHM of the interference signal in white illumination FF-TD-OCT system, which indicates the axial resolution of 1.6μm. b) The FWHM of the interference signal in the FF-TD-OCT system with near infrared light source, which indicates the axial resolution of 3.9μm.

3.3.3 Testing images

Pellet layer structure

Figure 3.7 shows an example of the cross-section image of a small pharmaceutical pellet with one-layer coating. The image size is 0.2x0.7mm^2 and the coating structure of this pellet sample can be clearly resolved.

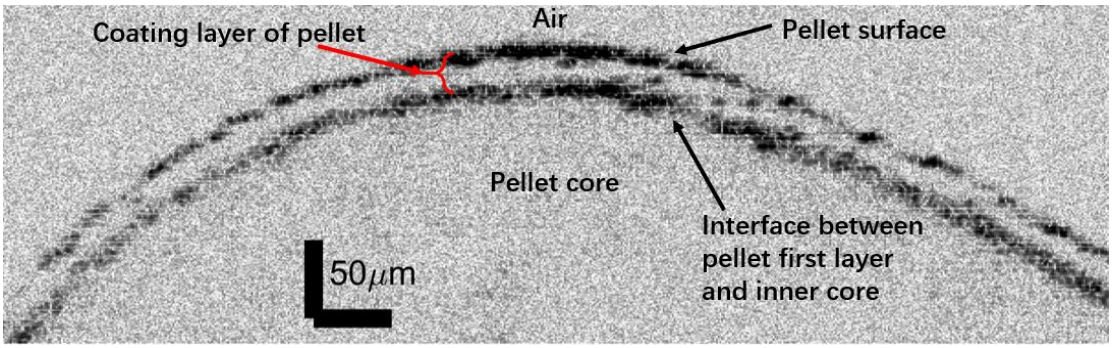

Figure 3.7: A cross-section image of a small pellet sample by our FF-TD-OCT system.

Laser Assisted in Situ Keratomileusis (LAISK) polymethyl-methacrylate (PMMA) model

LAISK is a laser vision correction technique commonly used in corneal power correction surgery. Figure 3.8a shows a cross-section OCT image of a LASIK model with the shape of saddle. This model was scanned by our FF-TD-OCT system and the generated 3D OCT data were reconstructed and shown in Figure 3.8b.

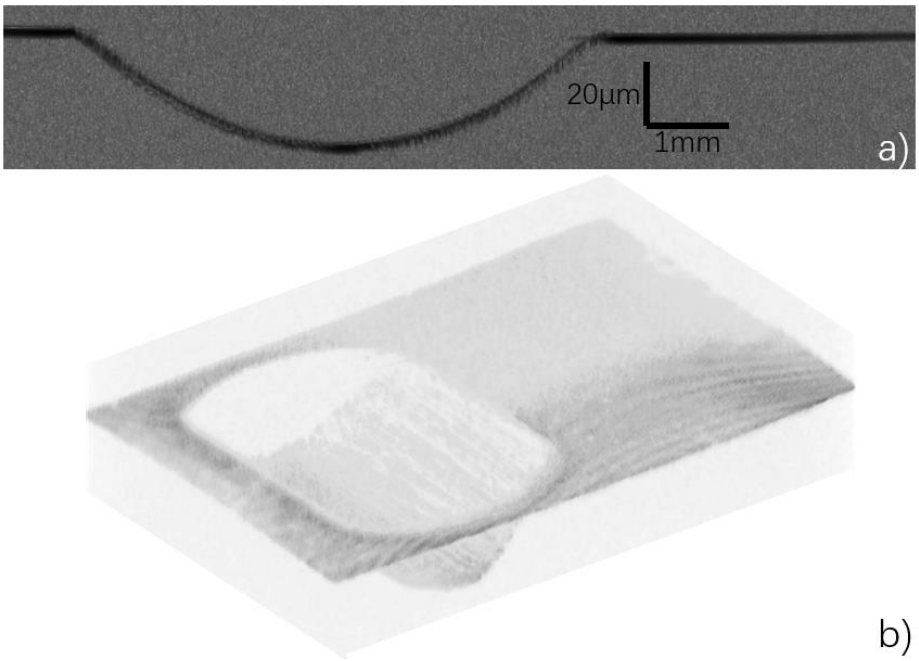

Figure 3.8: a) A cross-section image of a LASIK PMMA model with the shape of saddle by our FF-TD-OCT system. b) The 3D construction image this LASIK model generated from the OCT data.

3.4 Summary

In summary, this chapter presents the configuration of our FF-TD-OCT system and describes the operation procedure of it. Both white Quartz Tungsten-Halogen light bulb and near-infrared LED were used as the light source in the FF-TD-OCT system for different measurement purpose: the white light source was meant for thin layer and surface measurement; the near-infrared light source was meant for evaluation of thick multi-layer structure and particle within layers. The CMOS camera with high frame rate of 200 fps was synchronized with the motorized stage with sub-nanometre step movement in order to capture a series of *en-face* images of samples and generate 3D OCT

data. The best lateral resolution can be achieved by our FF-TD-OCT is 4.4μm and the axial resolution is 1.6μm for white light source and 3.9μm for near-infrared light source. The testing images demonstrated the capability of our FF-TD-OCT system in coating layer analysis and reconstructing 3D models. The following three chapters will present the combination of our FF-TD-OCT system and certain analytic algorithms to analyse multi-layer coating structure of pellets, surface power of cornea and properties of small flakes within automotive panel layer in detail.

Reference

1. A. Dubois, K. Grieve, G. Moneron, R. Lecaque, L. Vabre, and C. Boccara, “Ultrahigh-resolution full-field optical coherence tomography,” Applied optics 43(14), 2874-2883 (2004).

2. A. Dubois, and A. C. Boccara, Full-field optical coherence tomography (Springer Berlin Heidelberg, 2008), Optical Coherence Tomography, 565-591.

3. H. D. Ford, and P. T. Ralph, "Full-field optical coherence tomography." (2005).

4. J. Dugundji, “Envelopes and pre-envelopes of real waveforms,” IRE Transactions on Information Theory 4(1), 53-57 (1958).

5. T. S. Ralston, D. L. Marks, F. Kamalabadi, and S. A. Boppart, “Gaussian beam deconvolution in optical coherence tomography,” In Three-Dimensional and Multidimensional Microscopy: Image Acquisition and Processing XII, 5701, 1-12 (2005).

6. A. B. Miguel and C. G. Julio, "Ince–Gaussian beams," Optics Letters 29, 144-146 (2004)

7. F. Pampaloni and J. Enderlein, “Gaussian, hermite-gaussian, and laguerre-gaussian beams: A prime,” arXiv preprint physics/0410021 (2004).

8. W. Drexler, M. Liu, A. Kumar, T. Kamali, A. Unterhuber, and R. A. Leitgeb, “Optical coherence tomography today: speed, contrast, and multimodality,”

Journal of Biomedical Optics 19(7), 071412–071412 (2014).

9. A. F. Fercher, W. Drexler, C. K. Hitzenberger, and T. Lasser, “Optical coherence tomography-principles and applications,” Reports on progress in physics 66(2), 239 (2003).

Chapter 4. Pharmaceutical pellets analysis with FF-TD-OCT

In the pharmaceutical industry, the film coating of pellets is an important way of controlling the release of active pharmaceutical ingredients (API) in the human body. Pellets have a coating structure with multiple layers and the thickness of the film coating is significant to ensuring drug absorption and avoiding dose dumping problems. The accurate measurement of film coatings will help to control the release rate of pellets in the human body. In this chapter, we developed the FF-TD-OCT system to measure the coating thickness of multi-layer coated pharmaceutical pellet samples non-destructively. A set of *en-face* images from pellet samples were captured to form volumetric three-dimensional OCT data. Afterwards, we automatically characterized the coating thickness accurately by dividing the 3D data in several cells in lateral direction, calculating their individual thickness from the depth profile of average A-scans of each cell. This demonstrates the potential of our FF-OCT system as a non-destructive and non-contact imaging tool for analyzing film coatings of pharmaceutical pellet samples.

4.1 Introduction to pellet coating thickness measurement

In order to control the release process in the production of solid dosage forms in the pharmaceutical industry, layered coatings are designed for pellets as diffusion barriers and coated pellets are enclosed into capsules or compressed into tablets [1]. Additionally, film coatings are used for the purpose

of masking taste, improving drug stability and the physical separation of incompatible components in the same dosage form [2,3]. The release rate of a drug depends on hydrostatic pressure within the pellet, the thickness and viscosity of the coating layer [4]. Meanwhile, the thickness of a pellet's coating has an effect on the filling mechanism by which pellets are filled into hard shell capsules [5]. Coating thickness is one of the most important attributes of the film coating process. Its thickness is normally from 10μm to 200 μm. Thick film coatings will result in delayed drug dissolution while thin film coatings will result in low anticipated protection, which may disable the function of drug. Therefore, it is significant to control the coating thickness of pharmaceutical pellets precisely in order to ensure the high quality of solid dosage form products.

Fluorescence microscopy has been proposed for characterizing pharmaceutical pellets and their coatings geometrically [6]. This analysis procedure requires cutting an individual pellet and photographing the cross-section with fluorescence microscopy. Several models of pellet shape were made to evaluate the coating thickness of pharmaceutical pellets. The usage of this method in predicting variations in the release rate of drugs due to geometrical variations in pellets was demonstrated in [6]. However, this method is destructive in nature and it is also based on mathematical models rather than direct measurement, which may introduce errors for different irregular pellets.

Various non-destructive analytical imaging techniques have recently been applied to evaluate the coating thickness of pellets: near-infrared (NIR) spectroscopy [3,7], Raman spectroscopy [8], terahertz pulsed imaging (TPI) [9-11]. In previous studies, OCT has also been applied to characterize coating thickness and evaluate the coating structure of pharmaceutical pellets [12] and

tablets [13-15] and to the in-line monitoring of their coating process [16-20]. Most of this research involved analysing 2D cross-section images of pellet samples to evaluate the thickness distribution. In this chapter, our FF-TD-OCT system is developed to generate 3D data of pellet samples and we use these data to evaluate the thickness distribution in 3D to get a more accurate result.

4.2 Materials and methodology

4.2.1 Materials preparation of pellet samples

The core of the two-layer pellet sample is a microcrystalline cellulose (MCC) sphere (Celphere MCC seed core cp-507, Asahi Kasei Corp., Tokyo, Japan). The outer coating layer contains a combination of ethyl cellulose and hydroxypropyl methylcellulose (HPMC). The inner coating layer is a drug-loaded layer with 10% of active pharmaceutical ingredient (API) and 90% of hydroxypropyl methylcellulose [12]. The information of the three-layer pellet sample is unknown but is similar to the two-layer pellet sample and the lack of this information will not affect the following thickness distribution results as the refractive index difference between coating layers is minor.

Figure 4.1 shows a cross-section image of a cut-through pellet sample with two coating layers captured by the same CMOS camera used for the OCT measurements. This pellet sample has an approximately spherical shape with a diameter of about 850μm. In Figure 4.1, the centre bright part is the core and at the edge are two different coatings including one drug-loaded layer and one clear coating layer.

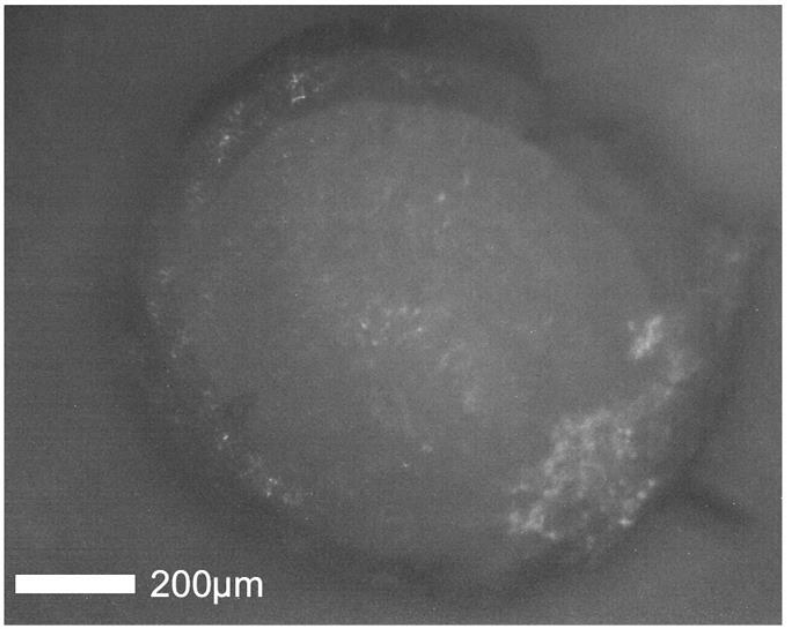

Figure 4.1: A cross-section image of a halved pellet sample which has approximately spherical shape with a diameter of about 850µm.

4.2.2 Pellet thickness analysis method in 3D

Current method of calculating coating thicknesses is to analyse single A-scans or averaging A-scans in a cross-section image by determining the first signal intensity peak position to (*N+1)*th peak position automatically. In this experiment, we try to divide the 3D OCT data of pellets into several cells in lateral direction. Each cell can provide an average A-scan signal and its depth profile and coating thickness information of *N*th layers. Therefore, we can get a mean value of this pellet from the averaging A-scan signals from all cells, which is more accurate than previous method. We also consider the geometry location of each A-scan, since the pellet shape is approximate to a sphere, the depth profile from each A-scan is not the true coating thickness.

In order to calculate the coating thickness of the two-layer pellet sample more precisely, a centre area of 600×50μm^2 within the total area of 700×50μm^2 was selected in the X-Y plane (transverse plane) (as shown in Figure 4.2). This area was divided into 48 square cells with each cell covering an area of 25×25μm^2 (1μm^2 per pixel). The average tomography signal of a single cell area can be measured by analysing the 625 A-scans within it. Therefore, the coating thickness of the two layers in each cell can be measured from the average A-scans and a total of 48 (24×2) groups of thickness values in an area of 600×50μm^2 can be extracted and tabled automatically. The mean value and standard deviation of the coating thickness of the entire area were then calculated from the averaging signal results in order to get an accurate value of coating thickness and its consistency.

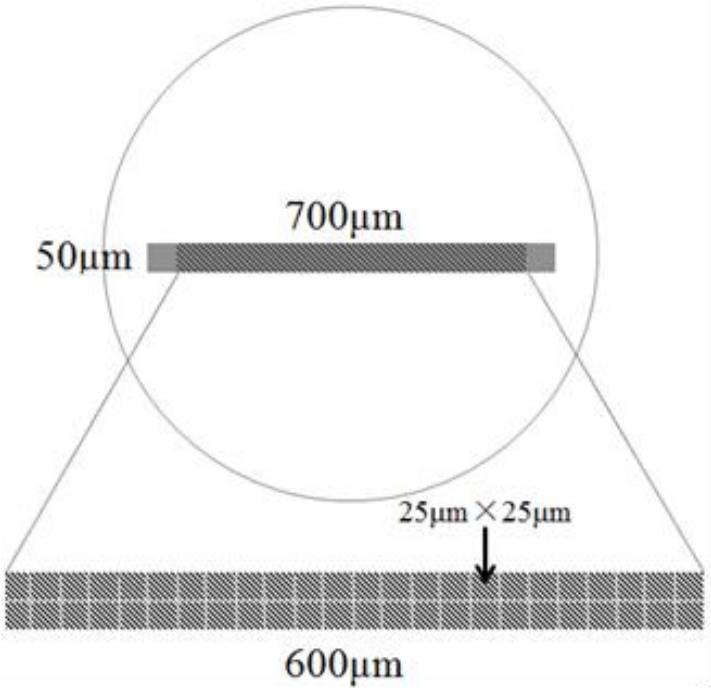

Figure 4.2: Sketch of the top view of a two-layer pellet sample with a diameter of about 850µm. The grey area, which covers an area of 700×50µm^2, is the area scanned by the FF-TD-OCT system. The shaded area, which covers 600×50µm^2, is the selected area for measuring the coating thickness. The selected area was divided into 24×2 (48) cells. Each cell covers an area of 25×25µm^2.

In the case of the three-layer pellet sample, the section division is a bit different since we want to demonstrate whether it is possible to evaluate coating thickness with smaller divisions. A centre area of 48×48µm^2 within the total area 992×50µm^2 was selected in the X-Y plane (transverse plane) (as Figure 4.3a). This area was divided into 36 square cells with each cell having 8×8 pixels covering an area of 8×8µm^2, as shown in Figure 4.3b. The average tomography signal of a single cell area can be measured by averaging 64 A-scans the in

8×8-pixel block. The coating thickness of the three layers in each cell can be measured from the average A-scan and a total of 36 (6×6) groups of thickness values can be extracted and tabulated. As same as the two-layer pellet sample, the mean value and standard deviation of the coating thickness were calculated and are presented in the results section in order to get an accurate value of coating thickness and its consistency.

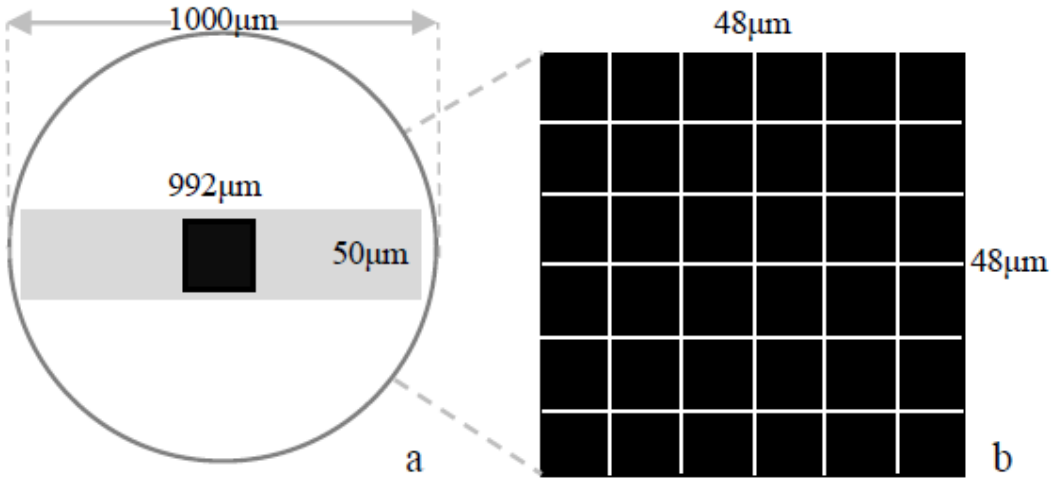

Figure 4.3: a) Top view of a three-layer pellet sample of diameter 1000µm. The grey area, which covers 992×50µm^2, is the area scanned with the FF-OCT system. The black area, which covers 48×48µm^2, is the selected area for measuring coating thickness. b) The selected area was divided into 6×6 (36) cells. Each cell covers an area of 8×8µm^2.

This thickness calculation method relies on the analysis of A-scans which is in the axial direction. However, pellet samples are supposed to be near-sphere and the coating thickness should be in radius direction. In this case, we assume that each pellet is a perfect sphere and different coefficients were given to each cell to calibrate the difference between lengths in axial direction and

radius direction. This coefficient depends on the size of the pellet sample and the distance from the cell to the centre of the pellet.

4.3 Pellet coating thickness evaluation

Figure 4.4 shows a typical raw OCT waveform obtained from a two-layer pellet sample. This signal contains background noise and interferogram signal. After the convolution process with the mirror interference signal, the signal to noise ratio of the interference signal can be significantly improved (>40dB). In order to produce the depth profile of the sample, the interferogram signal was further demodulated by using a Hilbert Transform to extract its envelope. This demodulated interferogram signal is regarded as the depth profile at a particular location of the pellet sample and the peak feature of the tomography signal corresponds to changes in the refractive index within the sample in the depth direction.

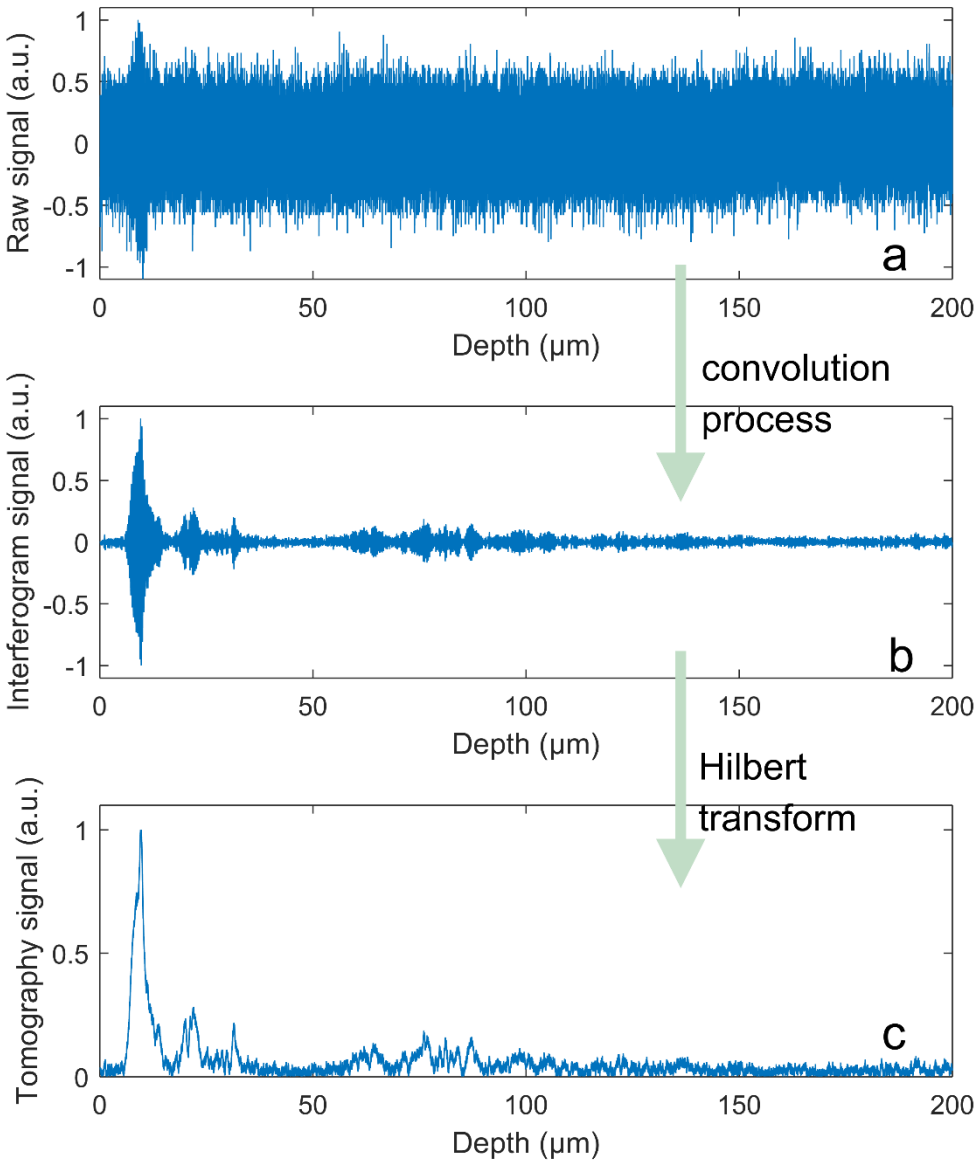

Figure 4.4: a) A raw interferogram signal of a two-layer pellet sample acquired from a single pixel in the CMOS camera. b) An interferogram signal of a two-layer pellet after convolution between the raw signal and mirror interferogram signal. c) A tomography signal of the two-layer pellet after Hilbert Transform with the interferogram signal. It reveals the envelope of this interferogram signal and is regarded as an “A-scan” in this work.

4.3.1 A two-layer pellet thickness analysis

A cross-section map (B-scan) was reconstructed by a series of A-scans in the same x-axis (lateral) in order to demonstrate the internal structure of this pellet sample. As shown in Figure 4.5, the B-scan covers an area of 700×200μm^2 in x (lateral) – z (depth) plane. The dark parts indicate the high intensity of the tomography signal while the bright parts indicate low intensity. Two coating layers can be clearly distinguished; the first layer is a relatively clean coating and the second layer contains particle-like features.

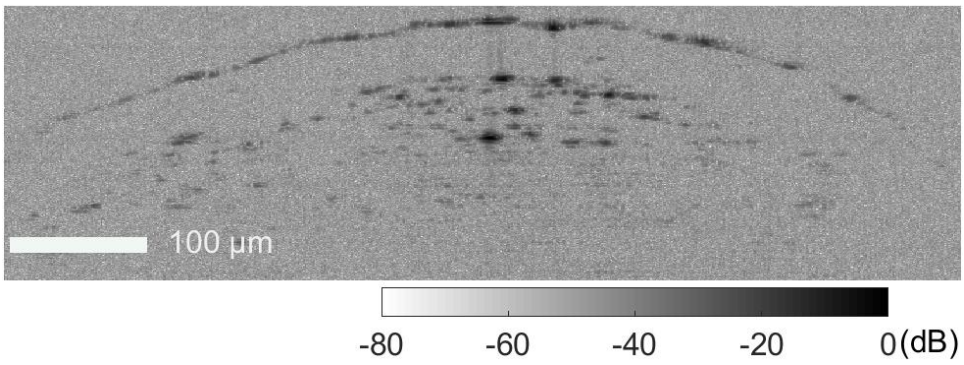

Figure 4.5: A cross-section map (B-scan) of a two-layer pellet sample. The B-scan covers an area of 700×200μm^2 in X-Z plane. Colour bar shows that the black means high intensity and the white means low intensity.

In order to accurately measure the coating thickness, 48 groups of thickness values were calculated automatically and presented in Table 4.1. For each averaged A-scan, the pellet surface was firstly determined by the first peak; then the second peak indicated the interface between the first layer and the second layer; the last peak indicated the interface between the second layer and pellet core. Therefore, two coating thicknesses can be automatically

calculated by determining the three depth positions: the surface, the first interface and the second interface. The thicknesses of the 34 cells can be computed, which yield the mean coating thickness of 39.7±7.3μm for the outer layer and 49.1±7.0μm for the inner layer respectively. This result matches well with the result previously reported by Li et. al. [17], which is 40μm and 50μm, respectively. However, there was problem in calculating the thickness in the other 14 cells (no layer can be resolved in 12 cells and only the outer layer can be resolved in the other 2 cells). This may be due to coating defects or faults during data acquisition, such as mechanical motion of samples, which will be studied in the future.

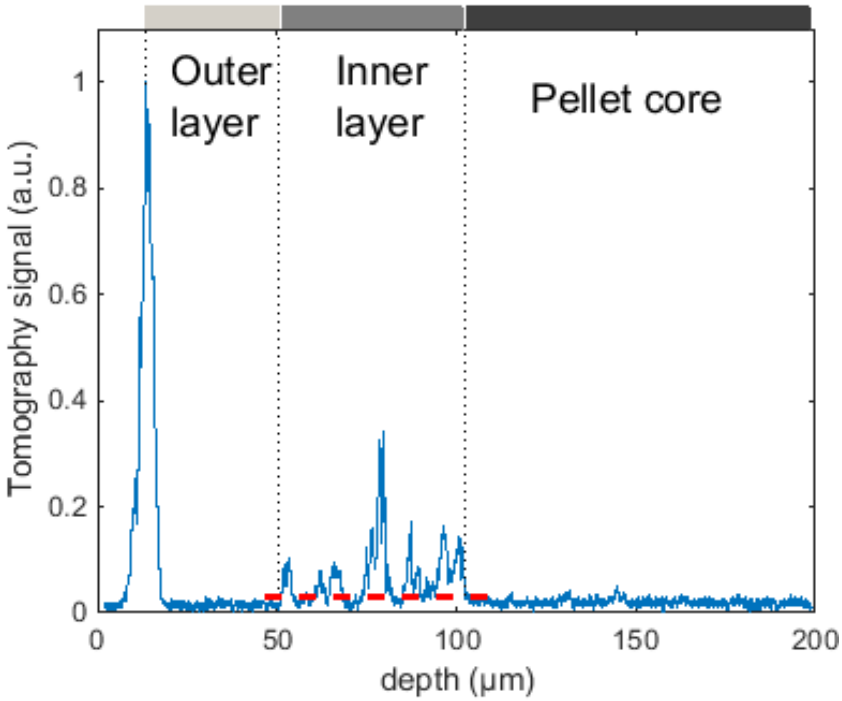

Figure 4.6: An averaged tomography signal of a typical cell within the selected area. The drug-loaded layer (inner layer) contains multiple peaks. The relative clean coating (outer layer) is between the drug-loaded layer and the maximum peak, which is the surface of this coated pellet sample.

In order to present the internal structure of the three-layer pellet sample, a cross-section map (B-scan) was reconstructed by a series of A-scans in the same x-axis. As shown in Figure 4.7, the B-scan covers an area of 992 × 200μm^2 in the X-Z plane. In this graph, three coating layers can be clearly distinguished, two of which contain particle–like features and the other one is relatively clean. The coating thicknesses of the three layers can only be roughly read from the A-scan graph (Figure 4.6), which are approximately 20μm, 20μm, and 50μm respectively.

Table 4.1: Coating thickness of the two-layer pellet sample (NA means that the thickness calculation is invalid.)

Cell No.	**Two-layer pellet Thickness (μm)**							
	Outer layer	***Inner layer***	***No.***	***Outer layer***	***Inner layer***	***No.***	***Outer layer***	***Inner layer***
#1	NA	NA	#18	41.9	42.4	#35	40.8	59.0
#2	NA	NA	#19	43.3	43.3	#36	38.9	47.7
#3	31.1	39.2	#20	NA	NA	#37	40.5	48.7
#4	36.6	38.1	#21	NA	NA	#38	36.1	63.4
#5	37.2	50.2	#22	51.2	46.2	#39	36.1	49.1
#6	NA	NA	#23	NA	NA	#40	44.1	43.6
#7	NA	NA	#24	NA	NA	#41	41.4	51.8
#8	36.2	47.2	#25	NA	NA	#42	35.0	45.3
#9	35.4	50.2	#26	NA	NA	#43	NA	NA
#10	24.9	64.3	#27	39.2	NA	#44	43.2	36.7
#11	45.5	43.0	#28	38.4	48.2	#45	56.9	NA
#12	39.0	49.5	#29	55.3	39.7	#46	45.0	50.1
#13	40.6	48.5	#30	40.2	47.0	#47	31.0	45.3

Cell No.	Two-layer pellet Thickness (μm)							
	Outer layer	***Inner layer***	***No.***	***Outer layer***	***Inner layer***	***No.***	***Outer layer***	***Inner layer***
#14	37.1	51.2	#31	54.1	46.8	#48	NA	NA
#15	35.6	54.6	#32	35.1	52.6	Mean	39.7	49.1
#16	21.2	65.4	#33	35.2	56.7	std	7.3	7.0
#17	44.7	51.6	#34	41.0	53.4			

4.3.2 A three-layer pellet thickness analysis

The same thickness distribution calculation method was applied to a three-layer pellet sample. The centre area 48x48μm^2 was divided into 6x6 cells, which is less than the two-layer pellet sample. The 36 groups of thickness value are presented in Table 4.2. The mean coating thickness of the 36 cells area can be calculated with the first layer 26.5±2.3μm, second layer 20.6±3.4μm and third layer 57.3±7.2μm respectively. With the smaller selected area at the centre of the pellet sample, there were no invalid groups of data, which suggested that it is better to calculate the thickness distribution around the centre area in order to avoid invalid results and possible faults during data acquisition.

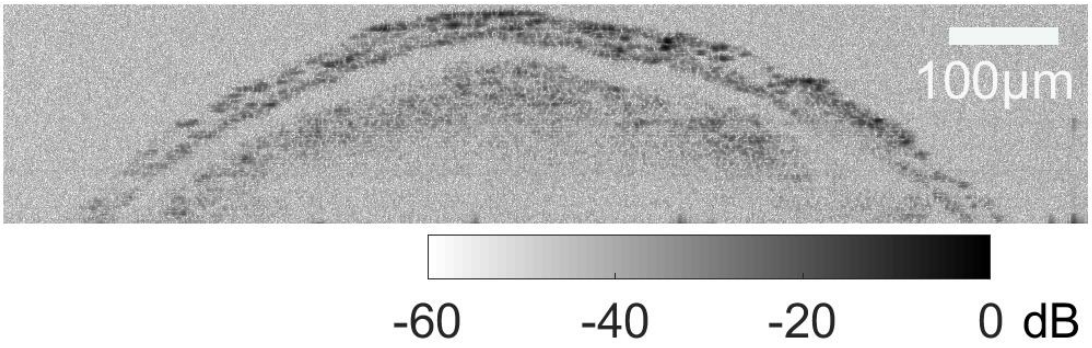

Figure 4.7: A cross-section map (B-scan) of a three-layer pellet sample. The B-scan covers an area of 992×200 μm^2 in X-Z plane. Colour bar indicates that the black means high intensity and the white means low intensity.

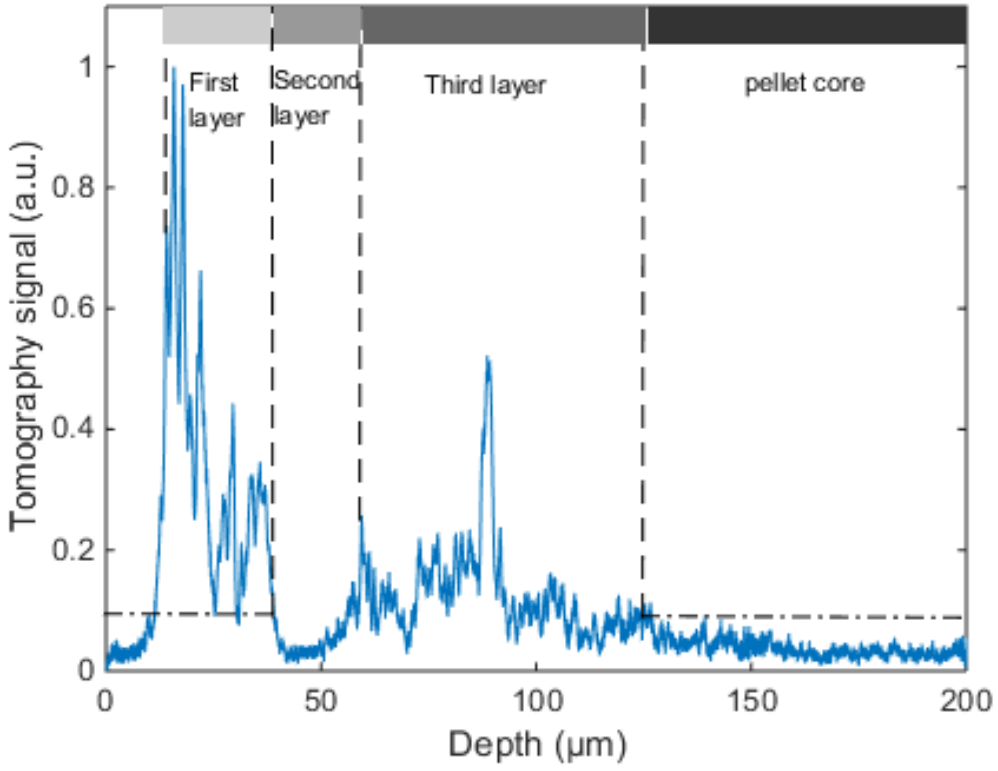

Figure 4.8: An average tomography signal of a typical cell in the selected area. The two drug-loaded layers contain multiple peaks. Therefore, the drug-loaded layers were

set to start at the first peak and end at 10% of the maximum signal after the last peak. The clean coating is between the two drug-loaded layers.

Table 4.2: Coating thickness of the three-layer pellet sample

Cell No.	**Three-layer pellet thickness** (μm)						
	1st layer	***2nd layer***	***3rd layer***	**No.**	***1st layer***	***2nd layer***	***3rd layer***
#1	25.0	27.2	54.1	#20	30.8	14.4	66.7
#2	24.5	26.7	41.1	#21	29.4	20.2	60.1
#3	27.0	22.5	49.8	#22	24.8	20.5	59.5
#4	28.0	21.7	53.5	#23	24.4	20.9	49.7
#5	23.9	21.7	62.2	#24	23.8	23.5	61.3
#6	25.0	18.4	69.2	#25	29.7	23.6	52.2
#7	26.5	24.0	58.6	#26	30.4	14.0	70.1
#8	26.1	23.9	42.5	#27	31.4	16.1	66.1
#9	25.0	26.2	52.6	#28	24.8	16.6	63.5
#10	27.1	18.0	62.3	#29	23.9	21.5	53.4
#11	24.8	20.6	62.4	#30	25.8	17.3	66.4
#12	27.1	19.0	60.1	#31	27.9	22.1	58.1
#13	30.2	22.0	41.4	#32	29.3	22.1	60.5
#14	25.7	23.9	54.4	#33	25.4	21.8	52.5
#15	28.0	19.4	59.5	#34	27.1	16.2	61.9
#16	24.1	22.8	60.4	#35	24.2	17.2	52.0
#17	25.1	20.3	62.2	#36	26.3	14.1	57.2
#18	22.4	23.1	56.3	Mean	26.5	20.6	57.3
#19	29.4	16.8	47.3	Std	2.3	3.4	7.2

Compared to the previous FF-OCT application on evaluating pellet coatings [17], this FF-OCT system focused on the automatic data analysis of coating thickness of a two-layer and a three-layer pharmaceutical pellet by averaging A-scan signals in 3D rather than analysing cross-section images. The larger areas of the pellet samples were imaged and quantified. By dividing the scanned areas into several sections, several groups of thickness distribution data were calculated from the mean A-scan signal and the mean thickness values for different layers were evaluated from these groups of data accurately. This method also considered the geometry of different sections. Different coefficients of all sections were given according to the sample size and the distance from the centre of each section to the centre of the pellet sample. The limitation is that the pellet samples were considered as perfect spheres in this experiment to simplify the calculation, but this is not the case with the pharmaceutical pellet production process. Better mathematical models of pellet shapes can be established to analyse effect on the thickness distribution in future studies.

4.4 Summary

In this study, it has been demonstrated that the FF-TD-OCT system has the promising capability of visualising the coating thickness of small multi-layer pellet samples and then we can quantify the thickness by averaging A-scan signals in 3D OCT data. The mean thickness of a two-layer pellet was precisely determined automatically as 39.7±7.3μm and 49.1±7.0μm for the outer and inner layers respectively. The mean thickness of a three-layer pellet were 26.5±2.3μm, 20.6±3.4μm and 57.3±7.2μm respectively. Additionally, particle-like features in the inner layer can be clearly resolved from the cross-section

images. These results demonstrate the potential of our FF-OCT imaging technique as an analytical tool for evaluating coating thickness distributions of pharmaceutical pellets.

Reference

1. C. A. Gilligan, and A. Li Wan Po, “Factors affecting drug release from a pellet system coated with an aqueous colloidal dispersion,” International Journal of Pharmaceutics, 73(1), 51–68, (1991).

2. N. Oman Kadunc, R. Šibanc, R. Dreu, B. Likar, and D. Tomaževič, “In-line monitoring of pellet coating thickness growth by means of visual imaging,” International Journal of Pharmaceutics, 470(1–2), 8–14, (2014).

3. M.-J. Lee, D.-Y. Seo, H.-E. Lee, I.-C. Wang, W.-S. Kim, M.-Y. Jeong, and G. J. Choi, “In line NIR quantification of film thickness on pharmaceutical pellets during a fluid bed coating process,” International Journal of Pharmaceutics, 403(1–2), 66–72, (2011).

4. P. W. S. Heng, L. W. Chan, and S. H. Chew, “Mechanism of pellet coat rupture and its effect on drug release,” Chemical & Pharmaceutical Bulletin, 47(7), 939–943, (1999).

5. R. Chopra, F. Podczeck, J. M. Newton, and G. Alderborn, “The influence of pellet shape and film coating on the filling of pellets into hard shell capsules,” European Journal of Pharmaceutics and Biopharmaceutics, 53(3), 327–333, (2002).

6. M. Andersson, B. Holmquist, J. Lindquist, O. Nilsson, and K.-G. Wahlund, “Analysis of film coating thickness and surface area of pharmaceutical pellets using fluorescence microscopy and image analysis,” Journal of Pharmaceutical and Biomedical Analysis, 22(2), 325–339, (2000).

7. M. Andersson, S. Folestad, J. Gottfries, M. O. Johansson, M. Josefson, and K.-G. Wahlund, “Quantitative analysis of film coating in a fluidized bed process by in-line NIR spectrometry and multivariate batch calibration,” Anal. Chem., 72(9), 2099–2108, (2000).

8. A. Bogomolov, M. Engler, M. Melichar, and A. Wigmore, “In-line analysis of a fluid bed pellet coating process using a combination of near infrared and Raman spectroscopy,” J. Chemometrics, 24(7–8), 544–557, (2010).

9. L. Ho, Y. Cuppok, S. Muschert, K. C. Gordon, M. Pepper, Y. Shen, F. Siepmann, J. Siepmann, P. F. Taday, and T. Rades, “Effects of film coating thickness and drug layer uniformity on in vitro drug release from sustained-release coated pellets: A case study using terahertz pulsed imaging,” International Journal of Pharmaceutics, 382(1–2), 151–159, (2009).

10. L. Ho, R. Müller, M. Römer, K. C. Gordon, J. Heinämäki, P. Kleinebudde, M. Pepper, T. Rades, Y. C. Shen, C. J. Strachan, P. F. Taday, and J. A. Zeitler, “Analysis of sustained-release tablet film coats using terahertz pulsed imaging,” Journal of Controlled Release, 119(3), 253–261, (2007).

11. J. A. Zeitler, P. F. Taday, D. A. Newnham, M. Pepper, K. C. Gordon, and T. Rades, “Terahertz pulsed spectroscopy and imaging in the pharmaceutical setting - a review,” Journal of Pharmacy and Pharmacology, 59(2), 209–223, (2007).

12. C. Li, J. A. Zeitler, Y. Dong, and Y.-C. Shen, “Non-destructive evaluation of polymer coating structures on pharmaceutical pellets using full-field optical coherence tomography,” J. Pharm. Sci., 103(1), 161–166, (2014).

13. J. Mauritz, R. S. Morrisby, R. S. Hutton, C. H. Legge and C. F. Kaminski, “Imaging pharmaceutical tablets with optical coherence tomography,” Journal of pharmaceutical sciences 99(1), 385-391 (2010).

14. J. A. Zeitler, Y. Shen, C. Baker, P. F. Taday, M. Pepper and T. Rades, “Analysis of coating structures and interfaces in solid oral dosage forms by three-dimensional terahertz pulsed imaging,” Journal of pharmaceutical sciences 96(2), 330-340 (2007).

15. H. Lin, Y. Dong, Y. Shen and J. A. Zeitler, “Quantifying pharmaceutical film coating with optical coherence tomography and terahertz pulsed imaging: an evaluation,” Journal of pharmaceutical sciences 104(10), 3377-3385 (2015).

16. D. Markl, M. Zettl, G. Hannesschläger, S. Sacher, M. Leitner, A. Buchsbaum, and J. G. Khinast, “Calibration-free in-line monitoring of pellet coating processes via optical coherence tomography,” Chemical Engineering Science, 125(200–208), (2015).

17. D. Markl, G. Hannesschläger, S. Sacher, M. Leitner and J. G. Khinast, “Optical coherence tomography as a novel tool for in-line monitoring of a pharmaceutical film-coating process,” European Journal of Pharmaceutical Sciences 55, 58-67 (2014).

18. Y. Dong, H. Lin, V. Abolghasemi, L. Gan, J. A. Zeitler and Y. C. Shen, “Investigating intra-tablet coating uniformity with spectral-domain optical coherence tomography,” Journal of pharmaceutical sciences 106(2), 546-553 (2017).

19. D. Markl, M. Zettl, G. Hannesschläger, S. Sacher, M. Leitner, A. Buchsbaum, and J. G. Khinast, “Calibration-free in-line monitoring of pellet coating processes via optical coherence tomography,” Chemical Engineering Science 125, 200-208 (2015).

20. D. Markl, G. Hannesschläger, S. Sacher, M. Leitner, A. Buchsbaum, R. Pescod, T. Baele and J. G. Khinast, “In‐Line Monitoring of a Pharmaceutical Pan Coating Process by Optical Coherence Tomography,” Journal of pharmaceutical sciences 104(8), 2531-2540 (2015).

Chapter 5. FF-OCT for surface power measurement

Fast, reliable and accurate measurement of corneal lens power is important in the management of a wide spectrum of eye disease, such as astigmatism. In this chapter, we propose a novel method of determining and calculating the shape and localised optical power of the anterior surface of cornea using our FF-TD-OCT technique. The FF-TD-OCT device was purposely designed and extensively validated for accurately imaging the cornea. The shape of the cornea is then determined automatically by segmenting its anterior surface from the acquired FF-TD-OCT data. A special focal power calculation algorithm, which considers the incidence angle of the light as an independent variable was developed and applied to it instead of a simple algorithm based on paraxial approximation and thus avoid the errors introduced by it. Given this, a focal power map of the anterior corneal surface was generated in which feature on a formalin-fixed cornea could be clearly resolved. In order to refine and evaluate the proposed technique, experiments were performed on laboratory lenses and accurate laser cut shapes. Finally, the capability of the proposed technique was demonstrated by performing experiments on fixed human corneas. The measured powers of the plano-convex lenses were found to match the theoretical values which verified the accuracy. Repeated measurements of the laser cut plastic models verified the consistency and repeatability of our FF-TD-OCT system. The power maps of six fixed corneas and two fresh corneas were generated in which small features of the corneas could be resolved. In addition to the 3D power map measurement experiments, surface degradation of a cornea was monitored during the scanning process including the surface

position and power change. Future work will focus on power measurements of human corneas in vivo. The corneal internal structure was assumed as consistent in the optical power calculation, despite small differences in the refractive index between the layers. The effect of these different layers on the refractive power will be the focus of my future research.

5.1 Introduction to cornea power measurement

It is important to precisely measure and analyse the shape and power of the cornea for undertaking many therapeutic and surgical treatments such as correction of the corneal shape or refractive errors using laser vision correction (LVC) in ophthalmology. The precise shape and power information of the corneal surface will be of significant benefit in planning any corrective procedures to the cornea and facilitating the design and fitting of contact lenses.

Early approaches to the measurement of intraocular lens (IOL) refractive power were based on mathematical models to calculate a cornea's refractive power from its anterior curvature [1]. Several theory-based IOL power calculations formulas were developed in order to obtain higher accuracy [2-6]. Errors in these calculations come from the measurement of the axial length, corneal power and the estimation of the pseudophakic anterior chamber depth [7]. The calculation of corneal power assumes that corneal sections may be described by a hyperbola, parabola, ellipse or circle model. By keratometry and topographic keratoscopy, the radius of corneal curvature can be measured and converted into corneal dioptric power [8]. Later research on IOL power calculations focus on the eyes after corneal refractive surgery [9-12]. Most of these methods rely on a keratometer which is a diagnostic instrument for

measuring the curvature of the anterior surface of the cornea and assessing the extent and axis of astigmatism. However, such calculations rely on a pre-defined corneal shape and introduce significant approximation errors. Theoretically, the most accurate method of obtaining the net corneal power is to determine the corneal surface curvature and calculate this at each location in each individual eye. Therefore, a measurement of corneal power requires a more direct method which can provide detailed information of the curvature of the corneal surface.

Previous research related to corneal measurements using OCT have focused on corneal microarchitecture and regional thickness profiles [13,14]. Compared to other imaging systems for corneal measurement, including Scheimpflug rotating cameras and ultrasound bio-microscopy, OCT has proved to be more accurate and precise in measuring corneal thickness because of its high axial resolution and high intra-individual repeatability [15,16]. OCT is capable of providing 3D images of biological tissue with micrometre resolution [17]. Recent research has reported a method for the segmentation and alignment of anterior segment OCT images almost as accurate as manual segmentation. From this, surface maps of the anterior segment of human eyes could be produced from rotational cross-sectional images [18]. Fourier-domain OCT systems were used in mapping the corneal surface with a conventional radial scan pattern consisting of several meridians and the net corneal power was calculated using the mean optical power for each meridian [19].

5.2 Materials and methodology

5.2.1 Materials preparation of lenses, plastic models and human corneas

In this study, three different kinds of near-spherical samples were scanned with our FF-OCT system, including uncoated plano-convex lenses, laser assisted in-situ keratomileusis (LAISK) polymethyl-methacrylate (PMMA) models, six formalin-fixed human corneas and two fresh corneas.

Four uncoated plano-convex spherical lenses, including item #LA1509 (focal length f=100 mm), #LA1708 (f=200 mm), #LA1484 (f=300 mm), #LA1172 (f=400 mm), were fabricated from RoHS-compliant BK7 glass (N-BK7) and have a long wavelength range from 350nm – 2.0μm. According to the specification, the refractive index of these lenses is 1.515 at 633nm and the surface irregularity is within a quarter of the wavelength, which makes them perfect for surface tomography.

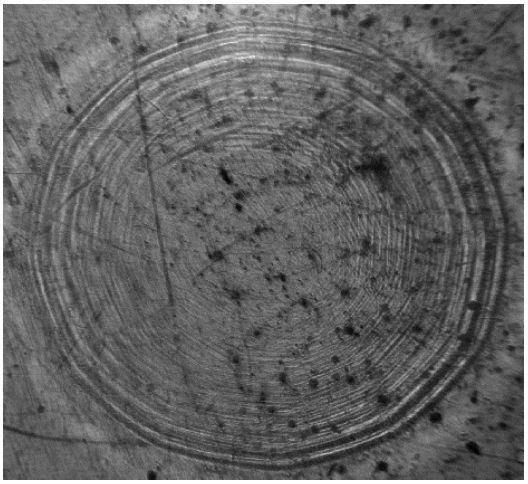

Figure 5.1: LAISK PMMA model. Artefacts on the surface of model caused by laser cuts are clearly seen.

Laser assisted in-situ keratomileusis is a laser vision correction technique commonly used in corneal power correction surgery. Three LAISK PMMA models were produced using the same laser cutting process to have a near-spherical shape, as shown in Figure 5.1. Each model was measured repeatedly three times to verify the consistency and repeatability of our FF-OCT system. Additionally, there are visible laser cut artefacts on the surface inevitably, but the laser cut artefacts made it better for our FF-OCT system to image the feature. A refractive index for these models was assumed to be 1.5 in the power calculation.

Cornea samples (shown in Figure 5.2b), including two fresh cornea samples and six formalin-fixed cornea samples were attached to the artificial chamber and thus kept in contact with a standard balanced sterile saline solution, which is specialized for intraocular irrigation. The anterior corneal surface was exposed to air while the posterior surface was in contact with the

saline solution in order to maintain the shape of corneas during measurement and keep the water pressure equivalent to that of a human eye.

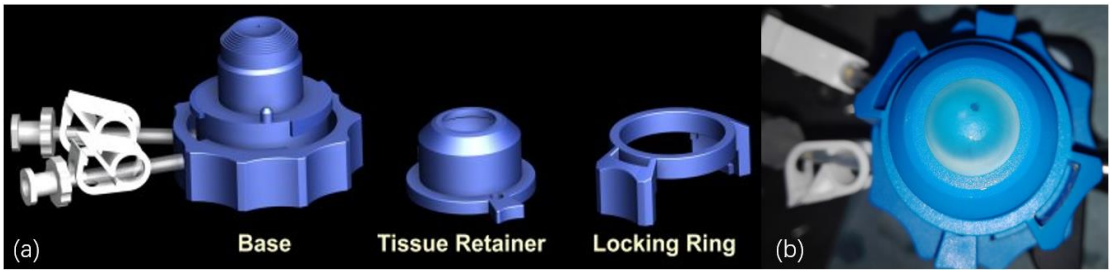

Figure 5.2: (a) The Barron artificial chamber[1]. It is comprised of three pieces: base, tissue retainer and locking ring. (b) Photo of a cornea attached to the artificial chamber, which was fixed onto the sample arm of the OCT system. The posterior surface is in contact with standard balanced sterile saline solution specialized for intraocular irrigation.

5.2.2 Surface individual power calculation method

The whole experiment process can be split into two parts: 1) we use our FF-OCT system to obtain 3D data set of samples; 2) we extract surface profiles of the samples from the 3D data sets and calculate the individual powers of the surfaces.

Human corneas were fixed in an artificial chamber, which was fixed on the sample arm of our FF-TD-OCT system, as shown in Figure 5.2b. For each cornea, a total data volume of 896x900x100,000 voxels, which covers 4.95 x4.92x0.4mm^3, was captured by our time domain OCT system. A refractive

[1] The Barron artificial anterior chamber: http://www.bpic.com/Products/aac.htm

index of 1.376 from previous study was used as the mean index for the human corneas in this experiment [20].

Firstly, each A-scan of the 3D OCT data of a LASIK PMMA sample (as shown in Figure 5.3a) was fitted to a one-term Gaussian model to determine the peak position of each signal which corresponds to the surface position at each pixel (as shown in Figure 5.3b). Given this, 3D surface maps of the samples were then generated from the peak positions of Gauss fitting signals. After generating surface maps of the samples, a median filter and disk averaging filter of radius of 5 pixels were applied. Each 3D surface was divided into a series of medians across the vertex point of the surface, covering each pixel on the surface of the LASIK model (as shown in Figure 5.3c). The individual focal power calculation method was introduced to calculate the back-vertex and power for a specified section of a defined surface (as shown in Figure 5.3d) [21,22].

As shown in Figure 5.3d, the incident light ray passes from medium n_1 to medium n_2 at (x_i, y_i) on a defined surface S with the vertex at (x_0, y_0). The back-vertex focal length is from the vertex of the surface to the focal point which is the intersection of the extension cord of the refracted ray with the optical axis passing through the vertex.

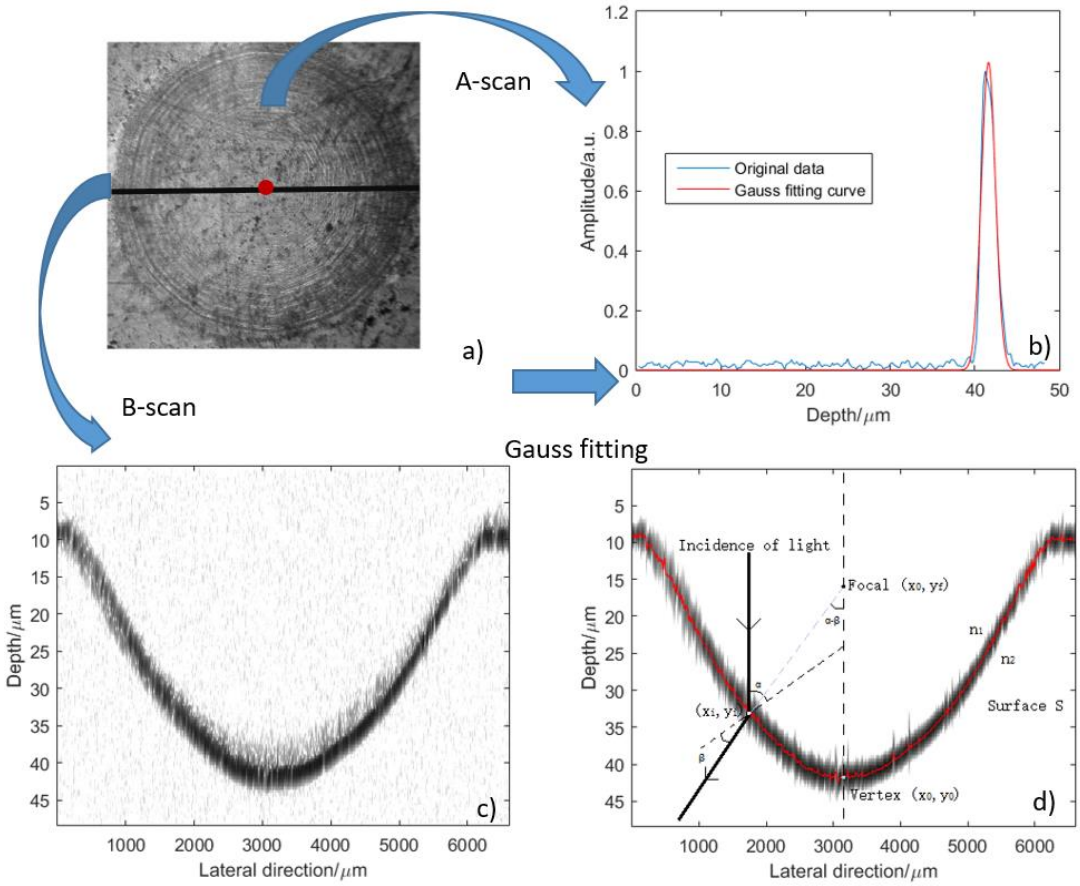

Figure 5.3: a) An *en-face* image of a LASIK PMMA sample. The red point indicates the pixel of the A-scan signal in b). The black line indicates the location of the B-scan image in c). b) Time-domain OCT signal depth scan (A-scan) and its one-term Gauss fitting result. The 3D OCT data can be regarded as a combination of A-scans at each pixel in the lateral directions. Each A-scan can be fitted with Gaussian function in order to determine the peak position of the surface position at each particular pixel. The surface profile of the whole 3D OCT data can be extracted by finding the peak position at each pixel. c) Cross-section image (B-scan) of surface of this sample. d) Gauss fitting result of B-scan in c) and optical power calculation of this surface S with the vertex at (x0, y0) and refractive index of n2. The incident light ray from a medium with refractive index n1, with an incidence angle α, meets the surface at (xi, yi) and is refracted at an angle

β. The reverse extension cord of the refracted light ray meets the optical axis passing through the vertex at focal point (x0, yi) with angle (α-β). The distance between the vertex and focal points (y0-yi) is the focal length at the incident point (xi, yi) considering the incident angle α. The power at (xi, yi) is the reciprocal of the focal length.

The distance between the vertex point (x_0, y_0) and the focal point (x_0, y_f) is:

$$y_0 - y_f = (y_0 - y_i) + (y_i - y_f)$$

Since $$\tan(\alpha - \beta) = \frac{(x_0 - x_i)}{(y_i - y_f)}$$

$$(y_i - y_f) = \frac{(x_0 - x_i)}{\tan(\alpha - \beta)}$$

Therefore $$y_0 - y_f = (y_0 - y_i) + \frac{(x_0 - x_i)}{\tan(\alpha - \beta)}$$

And the back-vertex focal length *f* from medium n_1 to medium n_2 at incident point (x_i, y_i) is:

$$f = \frac{n_1}{n_2}\left((y_0 - y_i) + \frac{(x_0 - x_i)}{\tan(\alpha - \beta)}\right) \quad (5.1)$$

The power *P* is the reciprocal of the focal length *f*:

$$P = \frac{1}{f} = \frac{n_2}{n_1}\left(\frac{1}{(y_0 - y_i) + \frac{(x_0 - x_i)}{\tan(\alpha - \beta)}}\right) \quad (5.2)$$

Note that the incident angle α is the angle between the incident vector (0, 1) and the normal vector (-dy, dx) at the incident point. The refracted angle β follows Snell's law:

$$n_1 \sin\alpha = n_2 \sin\beta$$

$$\beta = \sin^{-1}\left(\frac{n_1}{n_2}\sin\alpha\right)$$

As for the power calculation of a 3D surface, we took the maximum principle curvature of each point to calculate its individual power.

By taking the incident light into account, this method has the advantage of determining the optical power of a defined surface at any point on the surface of a sample without relying on the errors introduced during paraxial approximations for areas outside the central corneal region and loss of information regarding optical higher order aberrations.

5.3 Results

3D OCT data has the capability to provide surface profile and internal information of samples including layered structures, thickness and distribution. In order to verify the repeatability and accuracy of my method, this experiment focused on the surface profile of samples including spherical lenses, LASIK PMMA models and a formalin-fixed cornea. Firstly, all samples were placed vertically at the sample arm and scanned in depth with our FF-OCT system to generate 3D OCT data. Afterwards, the surface profile of the sample's surface was extracted and finally the power calculation method was applied to calculate the individual power and generate power distribution maps.

5.3.1 Laser assisted in situ keratomileusis (LAISK) polymethyl-methacrylate (PMMA) models measurement

In order to verify the consistency and repeatability of the system, three PMMA models with the same LAISK process were measured repeatedly three times. Figure 5.4a showed a B-scan of this PMMA model and its surface height profile. Small saw-tooth features were caused by laser cut in LASIK process and it was more obvious in power distribution map in the extreme value in Figure 5.4d. Mean power within the circular area in Figure 5d was calculated

for each model each time. The mean power is about 3.6 dioptres with the assumed refractive index of 1.5. Table 5.1 shows the consistency of mean power results of three groups of PMMA model with same LASIK process and the measurement process repeated three times in order to verify the repeatability of the FF-OCT system in measuring surface optical power.

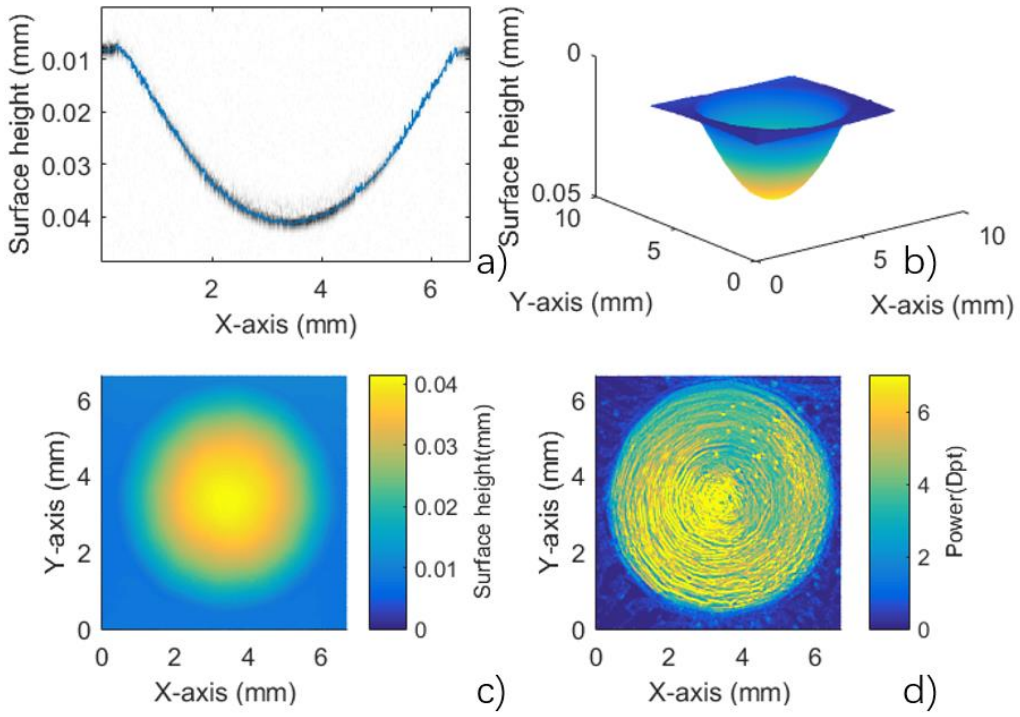

Figure 5.4: Surface profile and power distribution of LAISK PMMA model. a) A B-scan image of this PMMA model and the surface profile (blue line) by Gauss fitting each A-scan. b) 3D surface tomography of this LAISK PMMA model. This model has a maximum surface height of 33μm. c) Top view of LAISK PMMA models generated from 3D OCT data. The colour bar indicates surface height of the model. d) Power distribution of the LAISK PMMA model. Artefacts caused by the laser cut result in extreme power values at certain pixels.

Table 5.1: Mean power of each group of model with three repeated measurements.

Group No. of model	Times	Mean power (dioptres)
Group #1	#1	3.6 ± 1.9
	#2	3.6 ± 1.9
	#3	3.6 ± 1.9
Group #2	#1	3.5 ± 1.6
	#2	3.5 ± 1.7
	#3	3.5 ± 1.7
Group #3	#1	3.6 ± 1.7
	#2	3.6 ± 1.6
	#3	3.6 ± 1.6

5.3.2 Uncoated plano-convex spherical lenses measurement

In order to verify the accuracy of our FF-OCT system, four uncoated plano-convex spherical lenses, were measured; their power distributions were calculated along with the radii of fitting spherical surfaces. The experimental calculated mean powers of all four lenses matches with the theoretical power (shown in Table 5.2), which proved the accuracy of this time-domain OCT system in surface mapping power calculations.

Table 5.2: Theoretical and experimental powers and surface radii of uncoated N-BK7 plano-convex spherical lenses.

Spherical Lenses	Focal length (mm)	Theoretical power (Dioptre)	Theoretical surface radius (mm)	Experimental power (Dioptre)	Experimental surface radius (mm)
#LA1509	100	+10.0	51.5	9.1 ± 1.5	54.3
#LA1708	200	+5.0	103.0	4.9 ± 0.7	104.5
#LA1484	300	+3.3	154.5	3.3 ± 0.5	153.4
#LA1172	400	+2.5	206.0	2.5 ± 0.4	203.5

5.3.3 Formalin-fixed and fresh human corneas measurement

Human cornea contains epithelium, Bowman's layer, stroma, endothelium and Descemet's membrane. Figure 5.5 shows a cross-section image of corneal anterior surface generated from our FF-TD-OCT system. The thin Bowman's layer is clearly resolved. Although the refractive index of each layer is different, only the anterior surface of the cornea is considered to calculate the surface power of the cornea, because of the difficulties of segmenting each layer from 3D OCT data, especially the Bowman's layer. Then six formalin-fixed cornea samples (#1~#6) and two fresh cornea samples (#1&#2).

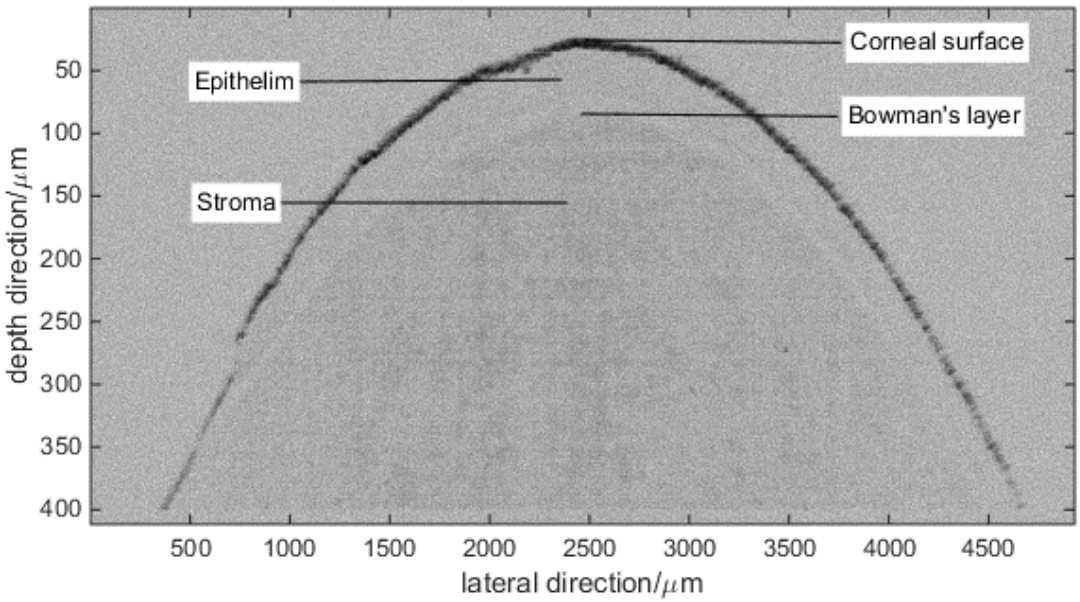

Figure 5.5: A cross-section image of a cornea generated from our OCT device. The epithelium layer and Bowman's layer can be clearly resolved. The layer beneath Bowman's layer is the stroma.

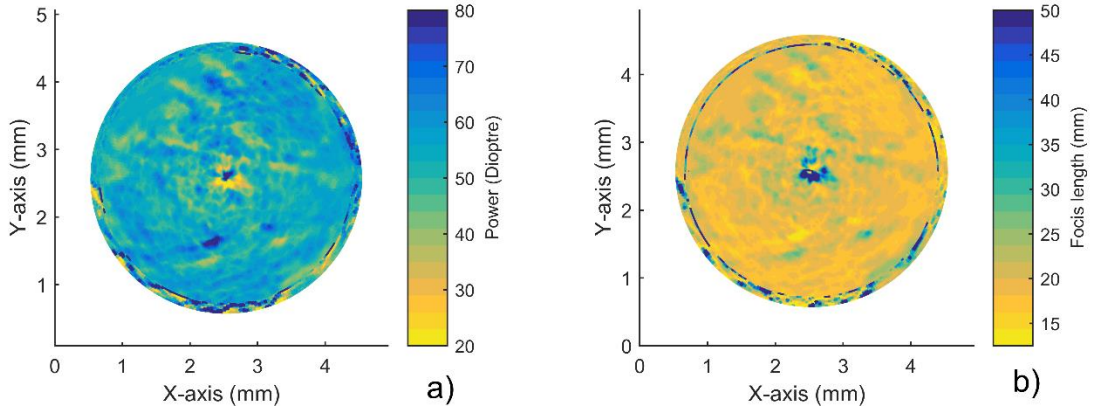

Figure 5.6: Individual power map and focus length map of fresh cornea sample #1.

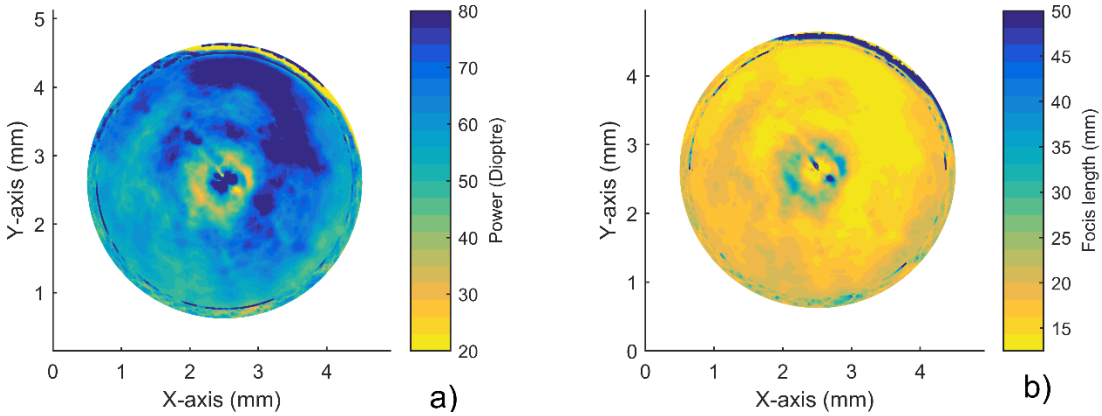

Figure 5.7: Individual power map and focus length map of fresh cornea sample #2.

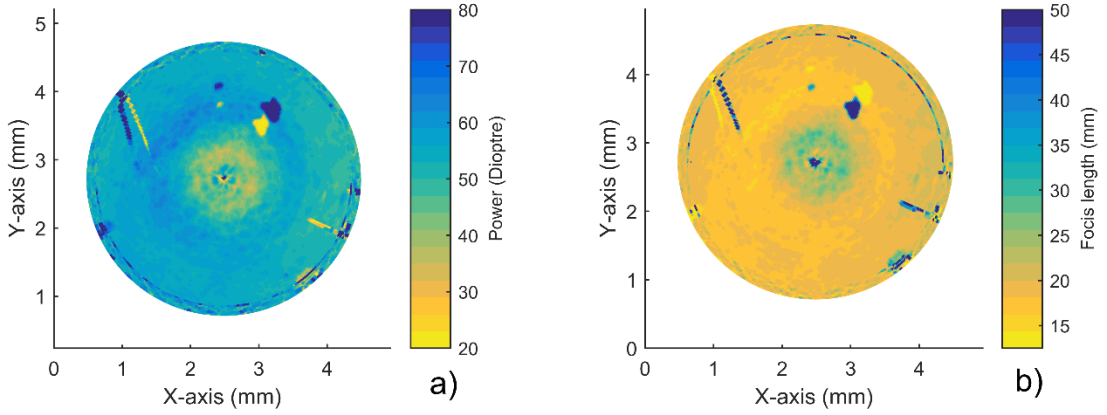

Figure 5.8: Individual power map and focus length map of fixed cornea sample #1.

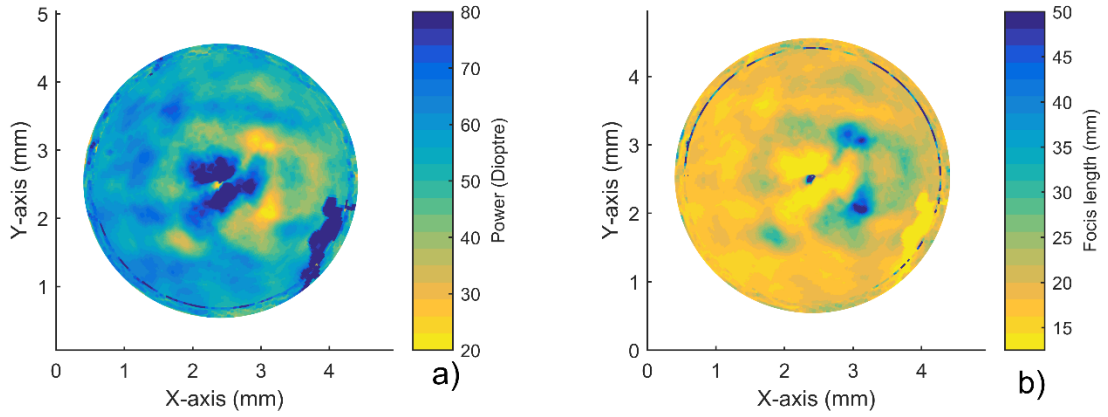

Figure 5.9: Individual power map and focus length map of fixed cornea sample #2.

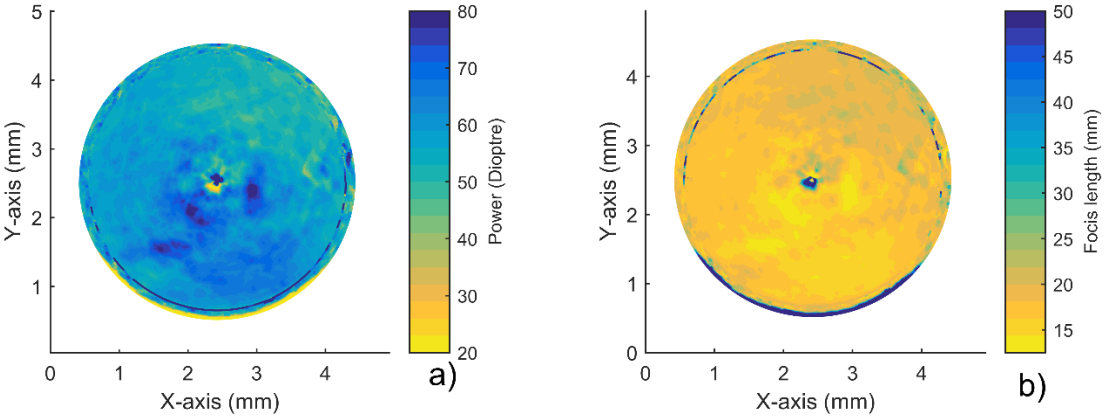

Figure 5.10: Individual power map and focus length map of fixed cornea sample #3.

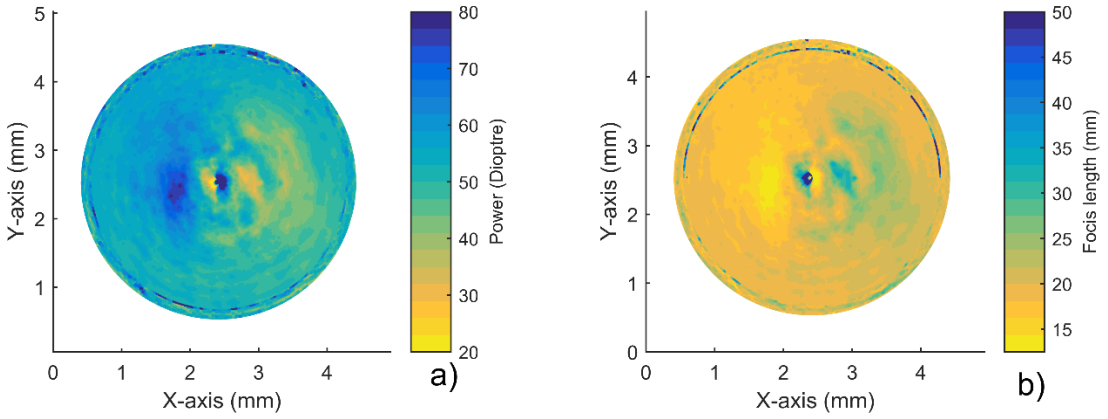

Figure 5.11: Individual power map and focus length map of fixed cornea sample #4.

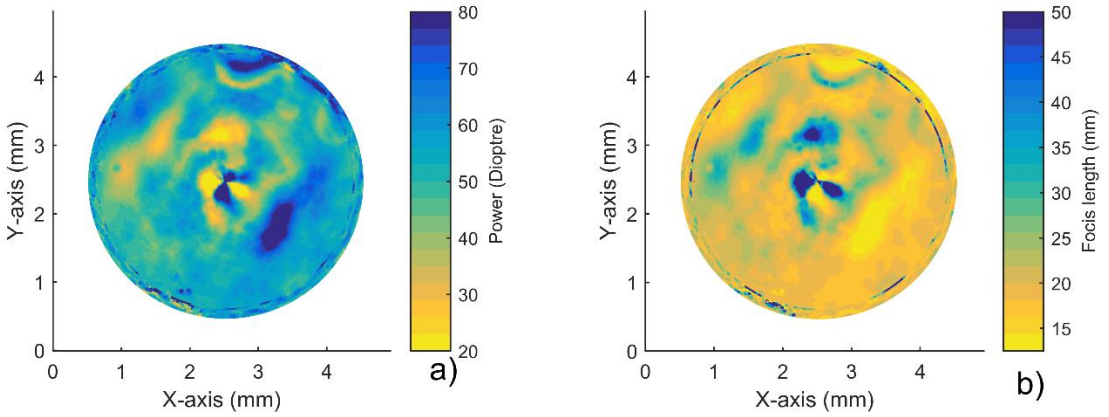

Figure 5.12: Individual power map and focus length map of fixed cornea sample #5.

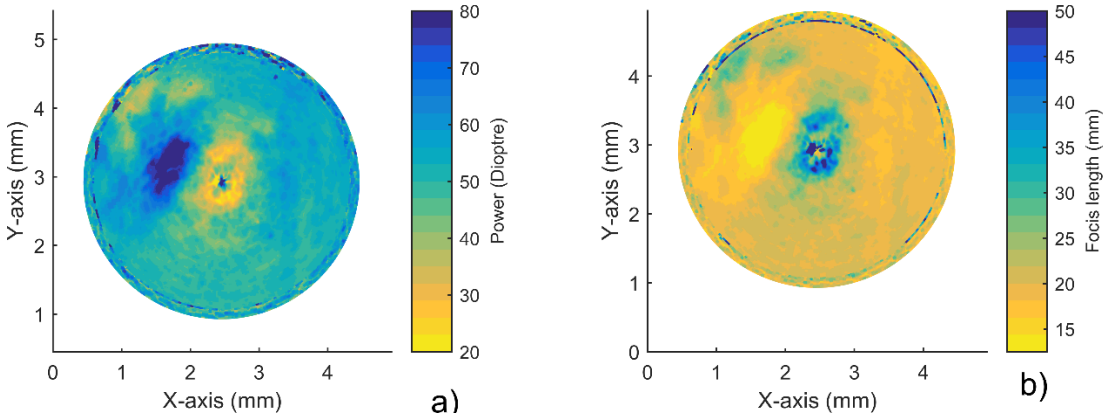

Figure 5.13: Individual power map and focus length map of fixed cornea sample #6.

Figure 5.6~5.13 show the corneal power maps and corneal focus length maps of six formalin-fixed cornea samples and two fresh cornea samples. These corneas were scanned by our FF-OCT system and their individual powers were calculated at each point by our power calculation method. With a depth scan of 400μm in axial axis, a series of *en-face* images covering an area of 4.95 x 4.92mm^2 were captured and generated into a 3D OCT data cube. By Gauss fitting of each A-scan at each pixel, the surface profile was determined at the peak position of the Gauss fitting signals. With the average refractive

index of the cornea assumed as 1.376 [20], the mean power of anterior corneal surface at the centre region are shown in Table 5.3. Meanwhile, the estimated curvature radius values and theoretical power values of all corneal samples were calculated by fitting perfect spheres to the 3D surface of the corneal samples.

Table 5.3: Mean power, estimated radius and estimated power of measured cornea samples.

Samples	Mean power (dioptre)	Estimated Radius (mm)	Estimated Power (dioptre)
Fresh cornea #1	52.6	7.1	53.1
Fresh cornea #2	62.6	5.8	64.3
Fixed cornea #1	50.2	6.9	54.9
Fixed cornea #2	59.7	7.2	51.9
Fixed cornea #3	63.9	6.4	58.5
Fixed cornea #4	56.6	7.3	51.8
Fixed cornea #5	50.6	7.3	51.8
Fixed cornea #6	48.6	6.9	54.8

In addition to the corneal power measurements, we also carried out an experiment on monitoring corneal surface power changes during a long period without pressure outside. The purpose of this experiment is to prove the capability of our FF-TD-OCT system for monitoring power changes of human corneas and the potential for future diagnostic usage. In this experiment, the constant water pressure, which maintained the shape of cornea, starts to decrease, while the supply of saline solution in artificial chamber is shut off. The cross-section images (B-scans) of corneal surface were captured under decreasing water pressure over a total period of 102 minutes, as shown in Figure 5.14. The time interval between each B-scan image is 6 minutes. The corneal surface position shifted 340μm and mean corneal power varied from 58 to 70 dioptres over the total time of measurement (as shown in Figure 5.15 (b)).

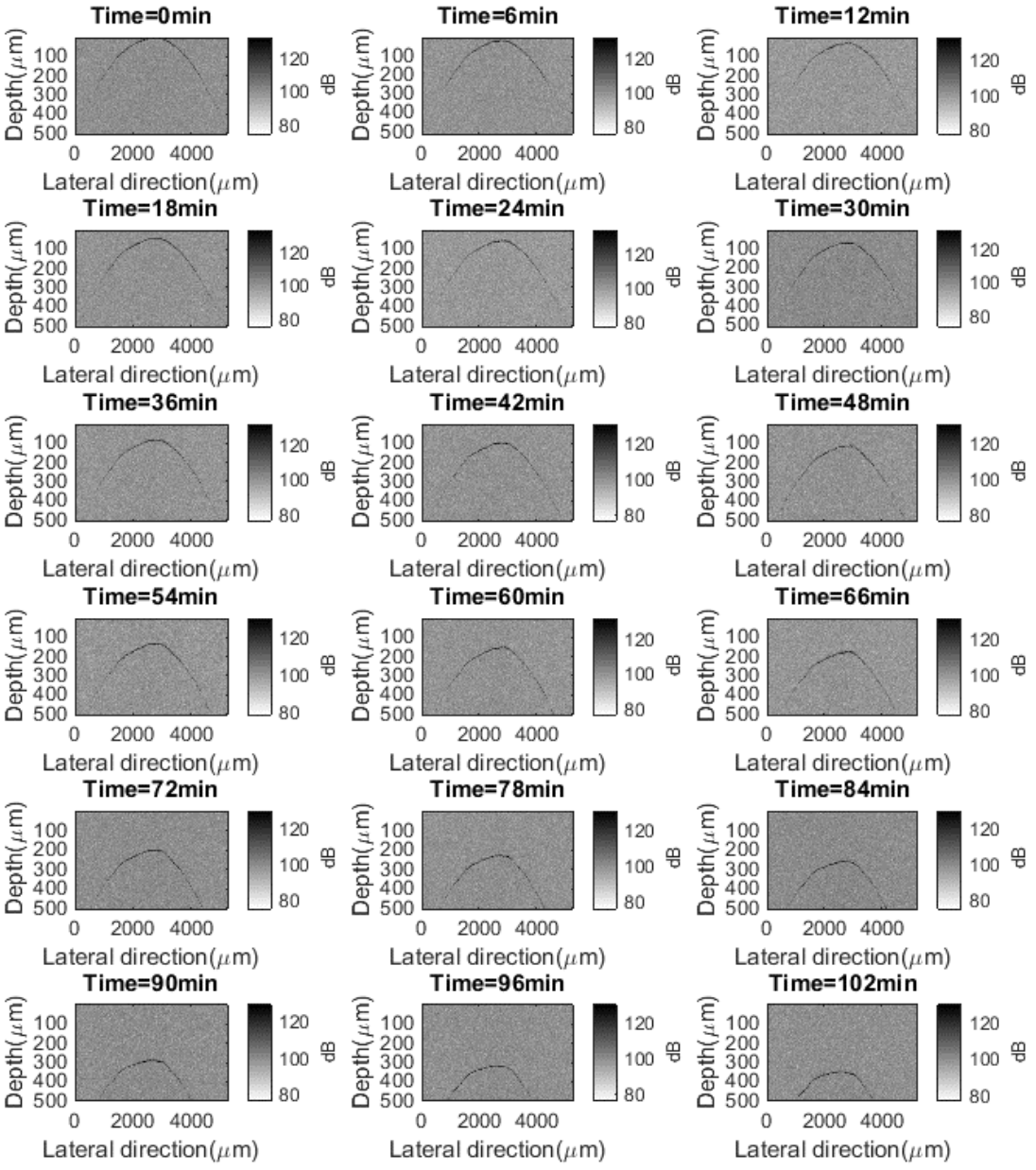

Figure 5.14: The formalin-fixed corneal surface change over a total duration of 102 minutes (18 cross-section images) in saline solution but without constant water pressure (The shutter of the artificial chamber, which controls the saline solution supply, was closed during scanning). The total corneal surface shift was 340μm in the depth direction.

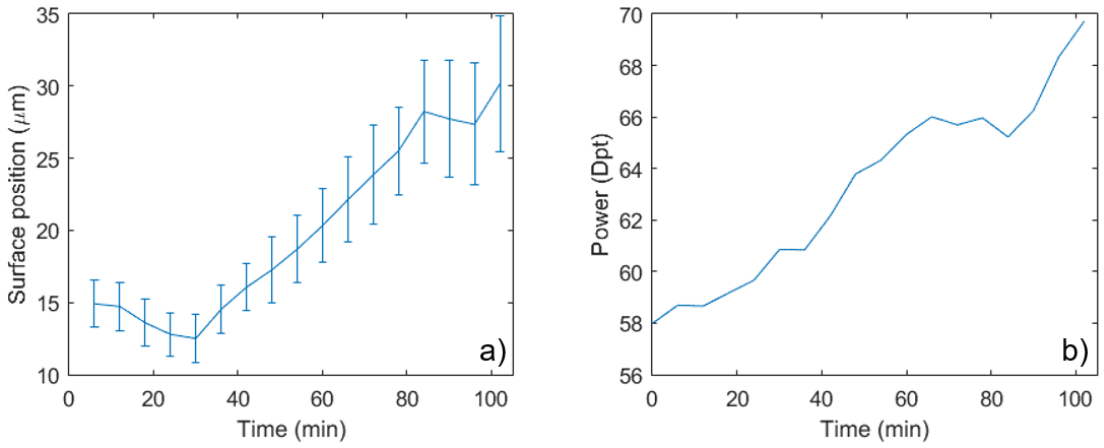

Figure 5.15: a) The formalin-fixed corneal surface change over time. The speed of surface change was increasing varying with time. b) Mean power change of the formalin-fixed corneal surface over the whole period of 102 minutes. The mean power increases from 58 dioptres to 70 dioptres.

In practice, the internal structure of the cornea is more complicated than a single layer structure. Each layer has a slightly different refractive index from the mean refractive index. It would bring in the cornea power calculation error if corneal structure is assumed as a constant structure in calculation. Therefore, future work should focus on the segmentation of the layers within cornea and how these layers will have effect on the refractive power of cornea.

5.4 Discussion

These experiments relied on 3D OCT data scanned by our FF-OCT system and the individual power calculation process which considers the incidence of light as an important parameter. Three different kinds of sample were measured and their power maps were generated including four plano-convex lenses, three LASIK PMMA models and six formalin-fixed and two fresh human corneas. The

measurements of the lenses and PMMA models were aimed at verifying the consistency, accuracy and repeatability of the FF-OCT system and the power calculation method. The individual power at each pixel on the anterior surface of the fixed cornea was then calculated.

Previous work on measuring refractive power of intraocular lens relied on the mathematical estimation and modelling of the anterior surface of the corneal. Errors occurred because of its indirect measurement of the corneal lens and estimation of important parameters. Comparing with previous methods of measuring lens power, such as keratometers and ultrasound bio-microscopy, tomographic imaging techniques, such as OCT, have the advantage of being direct, non-destructive and accurate, and are capable of imaging surface tomography of the corneal surface in three dimensions with high resolution.

Previous OCT applications in corneal power measurement has focused on the net power instead of individual optical power at each location [10,12,23]. Due to the limitation of scan-point OCT system, the surface of cornea was scanned radially, which were a series of meridians across the vertex point and each meridional image can provide the refractive power of corneal anterior surface. However, the surface map of cornea should be corrected with 3D construction and numerical recursive half searching algorithm due to the motion of human eye *in vivo* and possible errors in non-telecentric scan deformation [24].

By using FF-OCT system in this experiment, the non-telecentric scan problem can be solved because time-domain FF-OCT performs a depth scan instead of lateral direction scan, which does not result in the centre shift error

in the lateral directions. In this experiment, six formalin-fixed corneas and two fresh corneas were scanned with the time-domain OCT system to study its surface tomography profile. With an average back-vertex focal length and average power calculation algorithm on the defined surface [21], the power of the surface can also be accurately calculated, especially the individual optical power at each point of the surface. Small features on the cornea surface caused the extreme high value of power at certain pixels which increase the standard deviation. Meanwhile, the same OCT measurement and optical power calculation processes were applied to four groups of plano-convex spherical lenses and near-spherical LASIK PMMA models, which proved the consistency and accuracy of this OCT system and the optical power calculation method.

For corneal tomography, the paraxial approximation, which is a small-angle approximation used in Gaussian optics and makes a small angle to optic axis, is not accurate outside the central corneal region and significant errors were introduced when calculating individual power. In order to solve the problem of calculating the focal length and power without the limitation of paraxial approximations, we model the back-vertex focal length and use the angle of incidence as an independent variable. This method may do help to avoid the significant error introduced by using paraxial approximation. The ability of calculating individual power will be of significant benefit in planning any corrective procedures to the cornea and also will facilitate the design and fitting of contact lenses.

In another experiment, the formalin-fixed cornea was placed without a constant water pressure to monitor its surface and optical power change over a period of 102 minutes. The results showed that the surface shrank with an

increasing speed during a long term exposed to air and the optical power increased continuously.

The B-scan image of cornea generated from our OCT device showed its structure including epithelium, Bowman's layer and stroma clearly and also the features of the stroma. It is important to note that the corneal structure is assumed to be a consistent structure in power calculation, but it actually contains several layers with different refractive indices. Despite the difference in refractive index being much smaller than that between air and the corneal surface, the optical power effect from multiply layers should be studied in the future.

The current limitation of this method is that time-domain OCT system takes a long time to carry out a depth scan and large a quantity of data needs to be processed after 3D scanning. The depth scan process took 20 minutes with the camera frame rate of 100 fps but storing data took nearly 2 hours because of the large quantity of data. Therefore, the scanning process *in vivo* will be affected by the motion of the human eye. Possible solutions for issue include on using higher speed cameras as 2D detector and pre-processing the OCT data before storing it to disk. Another limitation is that fresh cornea and fixed cornea samples are not the same as cornea samples in vivo because of the tear film in front of human cornea. The real cornea power measurements may be different from the corneal power maps we have in this experiment. In addition, only the maximum median curvature of the surface was considered and had its power calculated in the case of measuring the focal power of 3D surface in the power calculation process. When taking the incident light into

account, the power calculation of the 3D surface is still problematic which will be further studied in the future.

5.5 Summary

In summary, we have proposed a novel method combining OCT imaging and a focal power calculation method to measure and calculate individual power of each point at the surface of the human cornea. A large area (4.95 x 4.92mm^2) of the corneal surface was captured in 3D by our FF-OCT system with a high resolution and both individual and mean optical powers were calculated by considering the angle of incident light, which reduced error from paraxial approximation. Meanwhile, plano-convex lenses and LASIK PMMA models were also measured repeatedly which verified the consistency, accuracy and repeatability of our FF-OCT system. The shrinking process of a formalin-fixed cornea was monitored over a long period, during which significant surface shifts in the depth direction and refractive power increases of the anterior corneal surface was observed. The corneal structure was assumed to be a consistent structure because of the small refractive index difference between each layer. Therefore, optical power effect across the different layers should be considered in future work. Meanwhile, this method can be applied to contact lens and in vivo corneal power measurement. Being able to calculate the accurate shape and focal power of corneas and lenses, it will be of significant benefit to corneal surgery.

Reference

1. T. Olsen, “On the calculation of power from curvature of the cornea”. British journal of ophthalmology, 70(2), 152-154 (1986).

2. J. T. Holladay, K. H. Musgrove, T. C. Prager, J. W. Lewis, T. Y. Chandler, and R. S. Ruiz, “A three-part system for refining intraocular lens power calculations,” Journal of Cataract & Refractive Surgery, 14(1),17–24 (1988).

3. J. A. Retzlaff, D. R. Sanders, and M. C. Kraff, “Development of the SRK/T intraocular lens implant power calculation formula,” Journal of Cataract & Refractive Surgery, 16(3), 333–340 (1990).

4. T. Olsen, K. Thim, and L. Corydon, “Accuracy of the newer generation intraocular lens power calculation formulas in long and short eyes,” Journal of Cataract & Refractive Surgery, 17(2), 187–193 (1991).

5. J. T. Holladay, “Refractive power calculations for intraocular lenses in the phakic eye,” American Journal of Ophthalmology, 116(1), 63–66 (1993).

6. T. Olsen, L. Corydon, and H. Gimbel, “Intraocular lens power calculation with an improved anterior chamber depth prediction algorithm,” Journal of Cataract & Refractive Surgery, 21(3), 313–319 (1995).

7. T. Olsen, “Sources of error in intraocular lens power calculation,” Journal of Cataract & Refractive Surgery, 18(2), 125–129 (1992).

8. C. Edmund, “Posterior corneal curvature and its influence on corneal dioptric power,” Acta Ophthalmologica,72(6), 715–720, (1994).

9. J. Aramberri, “Intraocular lens power calculation after corneal refractive surgery: Double-K method,” Journal of Cataract & Refractive Surgery, 29(11), 2063–2068 (2003).

10. W. Haigis, “Corneal power after refractive surgery for myopia: contact lens method,” Journal of Cataract & Refractive Surgery, 29(7), 1397–1411, (2003).

11. E. Borasio, J. Stevens, and G. T. Smith, “Estimation of true corneal power after keratorefractive surgery in eyes requiring cataract surgery: BESSt formula,” Journal of Cataract & Refractive Surgery, 32(12), 2004–2014 (2006).

12. K. A. Walter, M. R. Gagnon, P. C. Hoopes Jr., and P. J. Dickinson, “Accurate intraocular lens power calculation after myopic laser in situ keratomileusis, bypassing corneal power,” Journal of Cataract & Refractive Surgery, 32(3), 425–429 (2006).

13. K. M. Rocha, E. Perez-Straziota, R. D. Stulting, and J. B. Randleman, “SD-OCT analysis of regional epithelial thickness profiles in keratoconus, postoperative corneal ectasia, and normal eyes,” Journal of Refractive Surgery, 29(3), 173–179 (2013).

14. V. Jhanji, B. Yang, M. Yu, C. Ye, and C. K. Leung, “Corneal thickness and elevation measurements using swept-source optical coherence tomography and slit scanning topography in normal and keratoconic eyes,” Clin Experiment Ophthalmol, 41(8), 735–745 (2013).

15. S. Chen, J. Huang, D. Wen, W. Chen, D. Huang, and Q. Wang, “Measurement of central corneal thickness by high-resolution Scheimpflug imaging, Fourier-domain optical coherence tomography and ultrasound pachymetry,” Acta Ophthalmologica, 90(5), 449–455 (2012).

16. J. Huang, X. Ding, G. Savini, C. Pan, Y. Feng, D. Cheng, Y. Hua, X. Hu, and Q. Wang, “A Comparison between Scheimpflug Imaging and Optical Coherence Tomography in Measuring Corneal Thickness,” Ophthalmology, 120(10), 1951–1958 (2013).

17. A. Nahas, M. Bauer, S. Roux, and A. C. Boccara, “3D static elastography at the micrometer scale using Full Field OCT,” Biomedical Optics Express, 4(10), 2138 (2013).

18. D. Williams, Y. Zheng, P. G. Davey, F. Bao, M. Shen, and A. Elsheikh, “Reconstruction of 3D surface maps from anterior segment optical coherence tomography images using graph theory and genetic algorithms,” Biomedical Signal Processing and Control, 25, 91–98 (2016).

19. R. P. McNabb, S. Farsiu, S. S. Stinnett, J. A. Izatt, and A. N. Kuo, “Optical coherence tomography accurately measures corneal power change from laser refractive surgery,” Ophthalmology, 122(4), 677–686 (2015).

20. S. Patel, J. Marshall, and F. W. Fitzke, “Refractive index of the human corneal epithelium and stroma,” J Refract Surg, 11(2), 100–105 (1995).

21. S. B. Kaye, “Average focal length and power of a section of any defined surface,” Journal of Cataract & Refractive Surgery, 36(4), 665–670 (2010).

22. S. B. Kaye, “Approximating lens power,” Optometry and Vision Science, 86(4), 382–394 (2009).

23. M. Tang, A. Chen, Y. Li, and D. Huang, “Corneal power measurement with Fourier-domain optical coherence tomography,” Journal of Cataract & Refractive Surgery, 36(12), 2115–2122 (2010).

24. M. Zhao, A. N. Kuo, and J. A. Izatt, “3D refraction correction and extraction of clinical parameters from spectral domain optical coherence tomography of the cornea,” Optics Express, 18 (9), 8923 (2010).

Chapter 6. Automotive metallic flakes analysis with FF-TD-OCT

Automotive coating systems are designed to protect vehicle bodies from corrosion and enhance their aesthetic value. The number, size and orientation of small metallic flakes in the base coat of the paint has a significant effect on the appearance of automotive bodies. It is important for quality assurance (QA) to be able to measure the properties of these small flakes, which are approximately 10μm in radius, yet current QA techniques are limited to measuring layer thickness. In this chapter, we design and develop a time-domain (TD) full-field (FF) optical coherence tomography (OCT) system to scan automotive panels volumetrically, non-destructively and without contact. We develop and integrate a segmentation method to automatically distinguish flakes and allow measurement of their properties, including size, number and orientation for the first time. We test our integrated system on nine sections of five panels and demonstrate that this integrated approach can characterise small flakes in automotive coating systems in 3D, calculating the desired properties accurately and consistently. Our FF-TD-OCT system achieves a high lateral resolution of 4.4μm, which is higher than conventional scanning point scan OCT setups and, thus, better suited to resolving small flakes. Additionally, our segmentation method may also be applied to other OCT setups and other 3D imaging techniques such as confocal microscopy. This has the potential to significantly impact QA testing in the automotive industry.

6.1 Introduction to metallic flakes analysis in automotive panel

6.1.1 Motivation

The purpose of applying paint coating to automotive bodies is not only for corrosion protection but also aesthetic enhancement [1]. The majority of modern automotive paint systems consist of four layers: electro-coat (E-coat), primer coat, base coat and clear coat [1, 2]. The base coat of paint, which is the most expensive layer in the automotive paint system [2], provides various choices of colour to vehicle buyers. This layer consists of a mixture of primary colouring pigment and metallic or mica flakes. Both materials are compressed into a base coat binder, which is formulated either of acrylic or polyester polymers together with melamine. The industrial paint process requires spray-painting with significant manual craftsmanship or automated computer-controlled spray guns. Important parameters, such as spraying pistol type, spraying speed, spraying pattern, nozzle size, air pressure and distance between pistol and object, have key effects on controlling flake orientation. Meanwhile, the flake size, weight and geometry along with the viscosity of surrounding media also influence the flake orientation since flakes are hard sediments in coating formulations [3]. The small flakes, which are approximately 10μm in radius, are dispersed in the base coat and give the metallic sparkle effect of the paint system. The alignment of these flakes has a critical effect on achieving the desired appearance from all angles. Light hitting the base coat results in specular reflection at the centre of the flakes and diffusive scattering at the edge. Each individual flake will have a different size

and orientation; the statistical distribution of these parameters over the whole population of flake determines the macroscopic appearance. Hence, the measurement of these parameters can be used in the process to achieve a desired appearance. In addition, three-dimensional construction of measured data with a high spatial (axial and lateral) resolution is required to resolve and calculate the size and orientation of flakes within the base coat layer of automotive paint system. The high spatial resolution assures that each flake can be clearly resolved and distinguished from other flakes.

6.1.2 Measurement methods of automotive panel

The most common industrial method for the measurement of automotive paint layers is ultrasound testing [4,5], which relies on acoustic echo waves to determine the layer surface position and thus calculate the thickness of layers. This technique is based on contact measurements with hand-held scanners and is very powerful for use since it is easy to use, portable and fast. However, this contact measurement requires a smooth, flat, hard surface for the ultrasonic sensor head to get high precision results and so non-smooth surfaces have the potential to result in measurement error. Additionally, the spatial resolution for ultrasound testing is not sufficient for resolving small individual flakes such as those present in car paint of radius approximately 10μm. Another commercial method for measuring paint layer thickness, eddy-current testing [6,7], uses a coil of conductive wire with an electrical current to produce a magnetic field. This is used to sense defects in conductive samples by approaching them and monitoring phase and amplitude change of the eddy current. Because eddy-current testing can only be applied to non-conductive and non-magnetisable coatings on electrical conducting substrate material and

the film builds of automotive paint are all non-magnetisable, this method can only measure the overall coating thickness of automotive paint layers [8] and it is impossible for it to resolve small flakes. Both handheld ultrasound and eddy current instruments involve contact with the surface, which may not be suitable for online in-situ quality control, and neither achieves sufficient spatial resolution to resolve small flakes.

Recently, non-contact terahertz pulsed imaging (TPI) has been applied to automotive coating measurements [8-10]. TPI focuses a terahertz pulse onto a sample and then collects and characterises the reflected and backscattered terahertz pulse [11-13]. By measuring the time delay between terahertz pulses reflected on the sample surface and its inner structure, the layer thickness can be determined. It has been demonstrated as a tool for measuring the thickness of individual paint layers and mapping the thickness distribution of multi-layered automotive paint samples [8-10]. However, the lateral resolution of TPI is limited, by its wavelength, to no lower than 150 – 250μm [13]. Thus, TPI is not suitable for characterising the small flakes (radius of typically 10μm) in automotive base coats.

Confocal laser scanning microscopy (CLSM) [14] can achieve suggesting high lateral resolution (better than 1μm) to resolve flakes. It is a non-destructive and non-invasive optical imaging technique and uses a spatial pin hole placed at the confocal plane of a lens to remove out-of-focus light and increase the contrast of micrographs [15]. Since CLSM can construct 3D structures from obtained data, the flake orientation angles can also be calculated from measurements of optical reflection on the flake surface with CLSM [16,17].

The automotive industry currently utilises infrared thermography (IRT) as a non-destructive tool to test for cracks and defects in vehicle's body. IRT is a technique based on infrared radiation, acquiring and processing thermal information from non-contact measurement devices by a thermal camera [18]. Previous research has proven its capability of detecting dents and defects of car shells regardless of the shell geometry and location of defects [19]. Since IRT provides a two-dimensional facial temperature map, it is not able to obtain the orientation information of flakes within the base coat layer in 3D.

The high spatial resolution, including both axial and lateral resolution, makes OCT a potential technique for resolving the individual metallic or mica flakes, in the base coat of automotive paints, so that their size and orientation statistics may be measured. Recently, the capability of OCT to analyse clear coat and base coat thickness distribution in automotive paint systems has been demonstrated [20,21]. A point scan OCT system gave apparent resolution and size measurement of flakes using thresholding [20], however the lateral resolution of 12.4μm and point spacing of 10μm of the system used would mean significant errors for 10μm flakes [21]. The orientation of the flakes was not measured and the size calculation method did not consider the orientation of flakes from 2D projection onto horizontal plane. In this chapter, we will present the measurement of flakes with a full-field OCT system of significantly better lateral resolution (4.4μm vs. 12.4μm) for more accurate measurement of flake size and orientation properties.

6.1.3 OCT Segmentation methods

In addition to high resolution 3D image data, the measurement of flake size and orientation requires robust 3D image segmentation. We aim to resolve the metallic flakes and compute measurements of the flakes' properties, including size, number and orientation, by extracting them from the background using segmentation [22,23] which is an important technique in image analysis aiming to capture the edges of either all objects of an image [23] or only select ones [24]. In practice, this is often done by thresholding intensity values by a parameter selected either manually or automatically using a technique such as Otsu's [25]. While this can yield results quickly and may be favoured particularly for large 3D datasets, threshold parameters can require empirical manual selection and are not well suited to problems involving poorly-defined boundaries, varying contrast and particularly noise which is characteristic of images resulting from OCT. Methods aimed at the automatic segmentation of OCT images can be largely classified as graph-theoretical, machine learning and variational approaches.

Garvin et al. [26] proposed a graph-cut approach to segmenting five layers of macular OCT scans, presenting the segmentation as minimum-cost-cut problem on a graph using edge and region information. This was further extended to a method which was guaranteed to be optimal in terms of the cost function. A graph-theoretical approach was also presented by Chiu et al. [27] who used dynamic programming to optimise the segmentation. A shortest path search was also used by Yang et al. [28] to optimise the edge selection in a two-step segmentation schema. A common benefit of graph-theoretical methods is solution speed and it is typically used for segmenting layered

structures, which is not similar to our problem. While graph-search may be adapted to our problem, we are more concerned with accuracy and robustness than with speed. More recently, machine learning approaches have become popular due to their ability to obtain accurate results quickly. Fuller et al. [39] used support vector machines (SVM) to perform semi-automatic segmentation of OCT retinal images to calculate layer thickness for comparison with healthy volunteers and Vermeer et al. [40] has similarly used machine learning for OCT segmentation. Classifiers were trained from manually labelled samples and refined by the level set method. These methods can segment an image very quickly but they require large amounts of training data to be effective, expensive equipment with a large number of processing cores such as high-end Graphics Processor Units (GPUs) and may take a long time to train. The lack of available data makes this method unfeasible for testing.

In this work, we are interested in variational modelling for achieving segmentation due to its ability to achieve accurate results, robustness and potentially fast solution speeds. Mumford and Shah (MS) [22] proposed a more robust segmentation technique by building a variational model combining both intensity and region information. This was formulated as an optimisation problem with a trade-off between data fitting and contour length which aims to provide a smoother contour and reduce the likelihood of noise being regarded as an object. Chan and Vese (CV) [23] later provided an active contour solution to the Mumford-Shah problem by building in the level set function of Osher and Sethian [31] and a smooth approximation to the Heaviside step function. The authors also used the popular total variation semi-norm [32] for regularisation of the contour length. While not the only solution of the MS segmentation problem, active contours remains a robust technique for segmenting images

from many different modalities including OCT [33] on which many developments in segmentation have been based [24,33,34].

6.2 Materials and methodology

6.2.1 Materials preparation of automotive panel samples

In this study, five automotive paint samples with the same coating layers were measured, including two Indus silver samples, one Mauritius blue, one Barolo black and one Santorini black. For each sample, nine different 2.25x1.4 mm^2 sections were scanned as shown in Figure 6.1b. The entire paint coating consists of four layers including clear coat, base coat, primer coat and E-coat (as shown in Figure 6.1a). The first layer (clear coat) consists of uniform organic resins, which are transparent to visible light. The second layer (base coat) contains aluminium flakes which provide a sparkle effect. Because light cannot penetrate metal material and the third layer absorbs most of the light passing through gaps between the metallic flakes, our system can only resolve the top two layers which, since our interest is in the metallic flakes, is sufficient for our purpose.

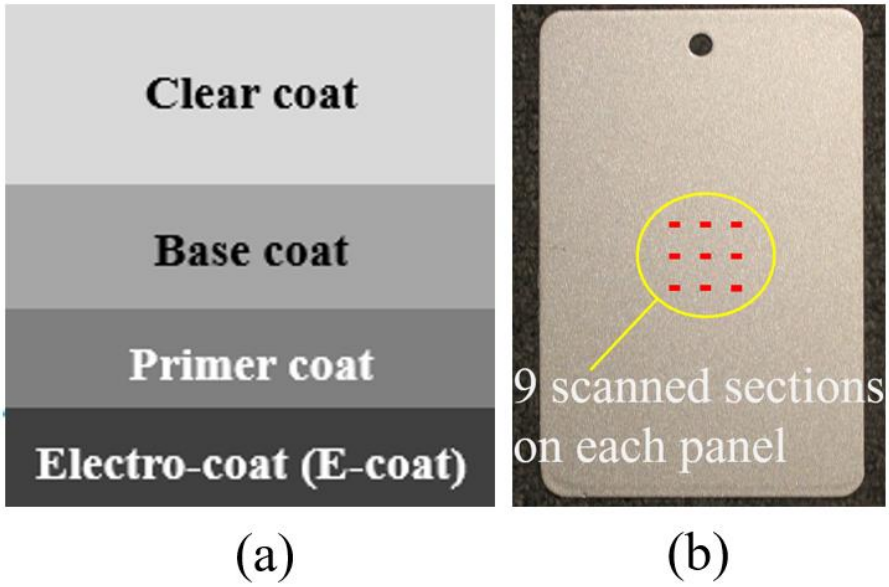

Figure 6.1: Automotive samples with 9 selected sections being scanned with our FF-TD-OCT system.

6.2.2 3D variational segmentation method

The procedure of our data processing is as follows:

1. **Data acquisition with FF-OCT system**
2. **Convolution process, Hilbert transform and base coat isolation**
3. **3D segmentation and labelling**
4. **Measurement of flakes properties: size, number and orientation**

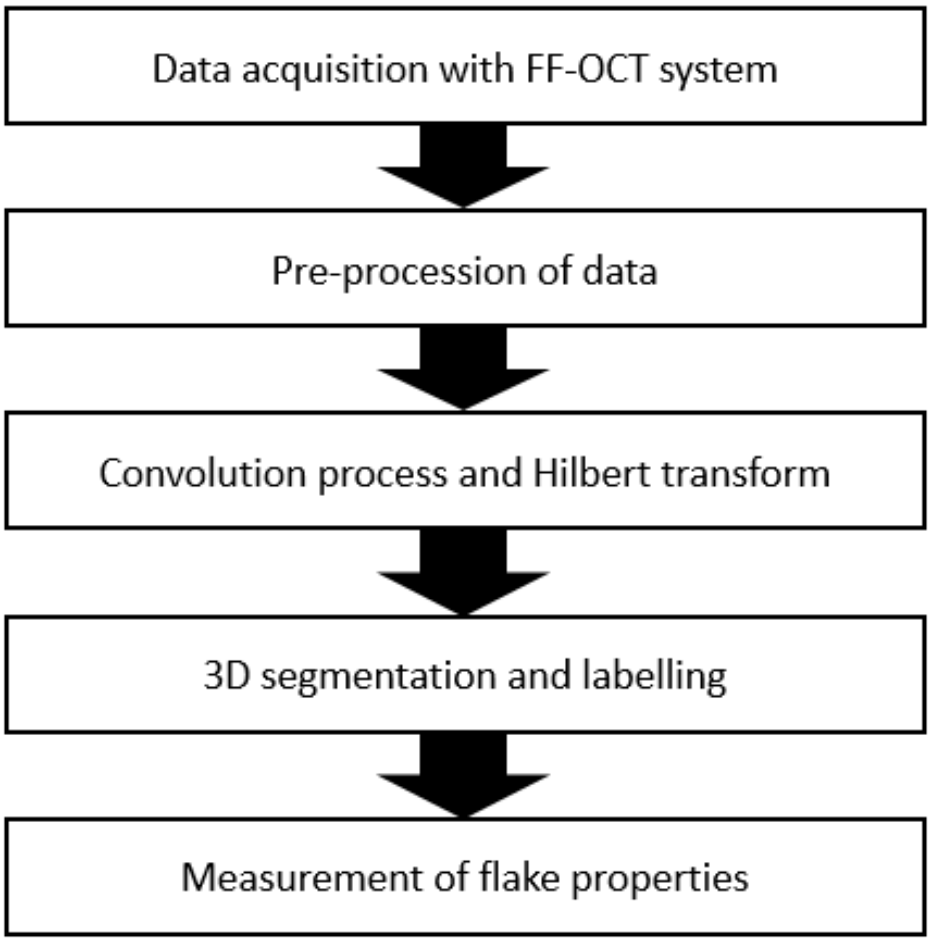

Figure 6.2: Flow chart of the data processing procedure. Firstly, data from each sample is acquired from our FF- OCT system. Secondly, we manually isolate the base coat layer from the raw data using cross-sectional images of the original data. Then, the base coat layer data is convoluted with the reference signal and processed with the Hilbert transform to extract the depth information of the flakes. Afterwards, our 3D segmentation method is applied to the data and each flake is labelled. Finally, we do a surface fitting to each flake and calculate its orientation and size individually as well as the quantity of flakes.

Firstly, five samples were scanned with our FF-OCT system. Secondly the base coat layer was isolated from each group of raw OCT data manually (although this may be achieved automatically by region intensity thresholding). Thirdly, background noise was reduced and the signal intensity of the flakes enhanced by a convolution process with the reference signal and an application of the Hilbert transform to the isolated data.

Given the processed data, we aim to automatically measure the properties of the imaged metallic flakes, particularly the size and orientation. To do this, we first define a method of segmenting the flakes, which allows them to be distinguished from background noise. We then obtain an index which allows us to identify individual flakes and finally fit the flake surface to a plane and calculate the desired measurements. We present this in the remainder of this section.

6.2.2.1 Segmentation of flakes

It is well-known that segmenting objects by thresholding or other intensity-based methods alone can result in poor results, particularly for images containing significant amounts of noise, such as those acquired by OCT. We aim to improve on this by incorporating spatial information. Chan and Vese [23] proposed a method of segmenting objects in images using region-intensity and contour length information. They proposed to solve the problem of Mumford and Shah [22] using the idea of level sets [31] to fit a contour to objects of interest. The problem is stated as:

$$\min_{\mathbf{c},\phi}\left\{f(\mathbf{c},\phi)=\underbrace{\lambda_1\int_\Omega(z-c_1)^2H(\phi)\mathrm{d}\mathbf{x}+\lambda_2\int_\Omega(z-c_2)^2(1-H(\phi))\mathrm{d}\mathbf{x}}_{:=f_F(\mathbf{c},\phi)}+\underbrace{\alpha\int_\Omega|\nabla H(\phi)|_\beta\mathrm{d}\boldsymbol{x}}_{:=f_R(\phi)}\right\} \quad (6.1)$$

where $\mathbf{c} = (c_1, c_2) \in \mathbb{R}^2$, denotes the average intensities of the flakes (c_1) and the background (c_2), and $\phi := \phi(\mathbf{x}): \Omega \to \mathbb{R}$ is a function whose zero-level set $\{\mathbf{x} | \phi(\mathbf{x}) = 0\}$ defines the boundaries of the flakes. The term $f_F(\mathbf{c}, \phi)$ is a data fitting term which should be minimised when the correct boundary is found and $H(\phi)$ denotes the Heaviside function. Note that if $\phi(\mathbf{x}) > 0$ for x within the flakes then $H(\phi)$ is equal to one on the flake and zero elsewhere. The final term $f_R(\phi)$ is a regularisation term designed to obtain a smooth contour around the flakes and prevent oscillations by constraining the length. In this case, regularisation is provided by a smooth approximation to the total variation semi-norm [32]. In our case, we have depth as well as lateral information which results in 3D data and so $\mathbf{x} = (x_1, x_2, x_3) \in \Omega \subset \mathbb{R}^3$, and we replace the Heaviside with the differentiable approximation

$$(H_\varepsilon(\phi) = 1/2 + \tan^{-1}(x/\varepsilon)/\pi, \varepsilon \in \mathbb{R}_{>0} \tag{6.2}$$

, which tends to the Heaviside as ε tends to zero. We solve the optimisation problem (6.1) by alternately minimising the objective functional with respect to c_1, c_2 and ϕ. We thus derive the first order optimality conditions with respect to these functions. For c_1 and c_2, we have :

$$\frac{\partial}{\partial c_1} f(\mathbf{c}, \phi) = 2\lambda_1 \int_\Omega (z - c_1) H_\varepsilon(\phi) \mathrm{d}\mathbf{x}, \quad \frac{\partial}{\partial c_2} f(\mathbf{c}, \phi) = 2\lambda_2 \int_\Omega (z - c_2)(1 - H_\varepsilon(\phi)) \mathrm{d}\mathbf{x}. \tag{6.3}$$

We also try to find the function φ which solves the optimisation problem (6.1)

$$c_1 = \frac{\int_\Omega z(\mathbf{x}) H_\varepsilon(\phi(\mathbf{x})) \mathrm{d}\mathbf{x}}{\int_\Omega H_\varepsilon(\phi) \mathrm{d}\mathbf{x}}, c_2 = \frac{\int_\Omega z(\mathbf{x})(1 - H_\varepsilon(\phi(\mathbf{x}))) \mathrm{d}\mathbf{x}}{\int_\Omega 1 - H_\varepsilon(\phi) \mathrm{d}\mathbf{x}}. \tag{6.4}$$

Similarly, we have

$$\frac{\partial}{\partial \eta} f_R(\phi + \eta\psi)|_{\eta=0} = -\int_{\Omega} \psi H_\varepsilon'(\phi) \nabla \cdot \frac{\nabla \phi}{|\nabla \phi|_\beta} \mathrm{d}\mathbf{x} + \int_{\Gamma} \psi H_\varepsilon'(\phi) \frac{\nabla \phi}{|\nabla \phi|_\beta} \cdot \tilde{n} \mathrm{d}\mathbf{x}, \tag{6.5}$$

, where $\Gamma = \partial\Omega$ denotes the boundary of Ω. We thus obtain the Euler-Lagrange equation

$$E_f(\phi(\mathbf{x})) = \lambda_1 (z(\mathbf{x}) - c_1)^2 - \lambda_2 (z(\mathbf{x}) - c_2)^2 - \alpha \nabla \cdot \frac{\nabla \phi(\mathbf{x})}{|\nabla \phi(\mathbf{x})|_\beta}, \mathbf{x} = (x_1, x_2, x_3) \tag{6.6}$$

6.2.2.2 Strategy for finding the level set function

We aim to find the zero point of the Euler-Lagrange equation (6.6). A common method of doing this is to use time marching. That is, we aim to solve the initial value problem:

$$\frac{\partial \phi(\mathbf{x};t)}{\partial t} = -\mathcal{E}_f[\phi(\mathbf{x};t)], \quad \phi(\mathbf{x},0) = \phi_0(\mathbf{x}) \tag{6.7}$$

which we can achieve by discretising in terms of time, selecting a suitable time step and defining an initial estimate of the function $\phi(\mathbf{x})$. While this is a commonly used method, in order to find a solution, the time step δ_t must be chosen sufficiently small, which makes this method slow. More recent approaches to solving this problem have been developed such as Additive Operator Splitting, split-Bregman [35] and Chambolle-Pock [36]. A fast solution technique for this problem was recently proposed for the two-dimensional (2D) case by the authors of [37] who proposed a restarted iterative homotopy approach to solving (6.7). The idea of the homotopy method is to transfer the non-linear problem of solving:

$$\mathcal{N}[\phi(\mathbf{x},t)] = 0 \text{ where } \mathcal{N}[\phi(\mathbf{x},t)] := \frac{\partial \phi(\mathbf{x};t)}{\partial t} + \mathcal{E}_f[\phi(\mathbf{x};t)] \tag{6.8}$$

to a high-order linear approximation $\mathcal{L}$. We thus construct the zero-order deformation equation:

$$(1-q)\mathcal{L}[\varphi(\mathbf{x};t,q)-\phi_0(\mathbf{x};t)]=q\hbar\mathcal{H}(\mathbf{x};t)\mathcal{N}[\varphi(\mathbf{x};t,q)] \tag{6.9}$$

where $\phi_0(\mathbf{x};t)$ is an initial estimate of the level set function, $\hbar$ is a non-zero auxiliary parameter, $\mathcal{H}$ and $q\in[0,1]$ is an embedding parameter and $\varphi(\mathbf{x};t,q)$ is a function of t and q:

$$\varphi(\mathbf{x};t,q)=\sum_{m=0}^{\infty}\phi_m(\mathbf{x},t)q^m=\phi_0(\mathbf{x},t)+\sum_{m=1}^{\infty}\phi_m(\mathbf{x},t)q^m \quad \text{s.t.} \quad \phi_m(\mathbf{x},t)=\frac{1}{m!}\frac{\partial\varphi^m(\mathbf{x};t,q)}{\partial q^m}|_{q=0}. \tag{6.10}$$

If the parameters and functions are chosen such that the approximation converges at $q=1$ then we have:

$$\varphi(\mathbf{x};t,1)=\sum_{m=0}^{\infty}\phi_m(\mathbf{x},t) \quad \text{and} \quad \left.\frac{\partial^m\varphi(\mathbf{x};t,q)}{\partial q^m}\right|_{q=0}=m!\,\phi_m(\mathbf{x};t) \tag{6.11}$$

Differentiating the zero-order deformation equation (6.9) m times with respect to q, diving by $m!$ and setting $q=0$, we have:

$$\mathcal{L}[\phi_m(\mathbf{x};t)-\chi_m\phi_{m-1}(\mathbf{x};t)]=\hbar\mathcal{H}(\mathbf{x};t)\mathcal{R}_m[\vec{\phi}_{m-1}(\mathbf{x};t)] \tag{6.12}$$

where $\vec{\phi}_k(\mathbf{x};t)=\{\phi_0(\mathbf{x};t),\dots,\phi_k(\mathbf{x};t)$ denotes the vector of solutions and we have:

$$\chi_m=\begin{cases}1 & \text{if } m>1\\ 0 & \text{if } m\le 1\end{cases}, \quad \mathcal{R}_m[\vec{\phi}_{m-1}(\mathbf{x};t)]=\frac{1}{(m-1)!}\left.\frac{\partial^{m-1}\mathcal{N}[\varphi(\mathbf{x};t,q)]}{\partial q^{m-1}}\right|_{q=0} \tag{6.13}$$

We choose the linear operator

$$\mathcal{L}[\varphi(\mathbf{x};t,q)] = \varphi_t(\mathbf{x};t,q) + \theta\varphi(\mathbf{x};t,q) \quad \text{s.t.} \quad \mathcal{L}^{-1} = e^{-\theta t}\int_0^t e^{\theta\tau}\varphi(\mathbf{x};\tau,q)\,\mathrm{d}\tau \tag{6.14}$$

Returning to our particular case, we aim to solve the non-linear parabolic equation

$$\mathcal{N}[\phi(\mathbf{x};t)] = \phi_t(\mathbf{x};t) + \lambda_1(z(\mathbf{x}) - c_1)^2 - \lambda_2(z(\mathbf{x}) - c_2)^2 - \alpha\nabla\cdot\frac{\nabla\phi(\mathbf{x})}{|\nabla\phi(\mathbf{x})|_\beta} = 0. \tag{6.15}$$

We make an initial estimate $\phi_0(\mathbf{x})$ of the level set function. We require the function R_1 in order to calculate ϕ_1:

$$\mathcal{R}_1[\phi_0(\mathbf{x};t)] = \mathcal{N}[\varphi(\mathbf{x};t,q)]|_{q=0} = \lambda_1(z(\mathbf{x}) - c_1)^2 - \lambda_2(z(\mathbf{x}) - c_2)^2 - \alpha\nabla\cdot\frac{\nabla\phi_0(\mathbf{x})}{|\nabla\phi_0(\mathbf{x})|_\beta} = \sigma(\mathbf{x}), \tag{6.16}$$

$$\phi_1 = \hbar e^{-\theta t}\int_0^t e^{(\theta-2)\tau}\sigma(\mathbf{x})\,\mathrm{d}\tau = \hbar e^{-\theta t}\int_0^t e^{(\theta-2)\tau}\,\mathrm{d}\tau\sigma(\mathbf{x}) = \hbar\frac{e^{-2t}-e^{-\theta t}}{\theta-2}\sigma(\mathbf{x}), \tag{6.17}$$

since R_1….. is a function of space but of time. Now, we aim to find ϕ_2 and similarly, we have

$$\mathcal{R}_2\left[\vec{\phi}_1(\mathbf{x};t)\right] = \hbar\frac{\theta e^{-\theta t}-2e^{-2t}}{\theta-2}\sigma(\mathbf{x}) - \alpha\beta\nabla\cdot\frac{\nabla\phi_1}{|\nabla\phi_0|}, \tag{6.18}$$

$$\phi_2 = \phi_1 + \hbar e^{-\theta t}\int_0^t e^{(\theta-2)\tau}\mathcal{R}_2[\vec{\phi_1}]\,\mathrm{d}\tau = \phi_1 + \hbar^2\left(\frac{-\theta(\theta-4)e^{-(\theta+2)t}-4e^{-4t}+(\theta-2)^2e^{-\theta t}}{2(\theta-2)(\theta-4)}\right)\left(\sigma(\mathbf{x}) - \alpha\beta\nabla\cdot\frac{\nabla\sigma(\mathbf{x})}{|\nabla\phi_0|}\right). \tag{6.19}$$

We proceed by beginning with ϕ_0 equal to the initial estimate and calculate to solutions

$$\phi^k = \sum_{i=0}^{2}\phi_i\,, k = 1\ldots n_{max} \tag{6.20}$$

Finally, we set the solution to be given by the heaviside $\phi := H(\phi^k)$ to obtain a binary result. We then define the corresponding matrices ϕ_h and ρ_h which are achieved by labelling the connected components. This provides us with an index of flakes and allows us to isolate individual flakes using the non-zero parts of

$$\mathbf{F}^i = \delta(\rho_h - i), \delta(x) = \begin{cases} 1 & \text{if } x = 0 \\ 0 & \text{otherwise} \end{cases} \tag{6.21}$$

for the ith flake.

6.2.2.3 Measurement of the metallic flakes

Given the segmentation result and index of distinct flakes, we aim to measure their properties. Letting $P^i = \{p = (p_1, p_2, p_3) | F^i(p) = 1\}$ denote the set of points for each flake, we calculate the number of flakes as the size of the set ${P^i}_i$ and the orientation and surface area of the flakes by calculating the best-fit 2D plane G^i defined by

$$n^i \cdot x = n^i \cdot p^i \tag{6.22}$$

where $\overline{p}^i = (\overline{p}^i_1, \overline{p}^i_2, \overline{p}^i_3)$, lying on the plane, is the mean of the coordinates of the flake $\mathbf{F}^i, n^i = (n^i_1, n^i_2, n^i_3)$ is the unit norm which gives the plane the best fit to the data. That is, it allows the plain to have minimal overall distance from the points $p^j_i \in P^i$ in the normal direction, satisfying the least squares problem

$$\min_{n^i} \left\{ \sum_j \left(\frac{n^i \cdot (p^i_j - \overline{p}^i)}{n^i \cdot n^i} |n^i| \right)^2 \right\}, \quad |n| = \sqrt{n_1^2 + n_2^2 + n_3^2} \tag{6.23}$$

Then we can give the normal n^i as the first eigenvector of the Hadamard product $Q^i \circ Q^i$ where $Q^i = \{p - \overline{p}^i | p \in P^i\}$ denotes the set P^i minus its mean triple $\overline{p}^i$. Given the best-fit plane, we use this to calculate the orientation with respect to the horizontal (lateral-lateral) plane by calculating the acute angle between the normals:

$$\theta^i = \cos^{-1}\left(\frac{n^i \cdot (0,0,1)}{|n^i||(0,0,1)|}\right) = \cos^{-1}(n_3^i) \tag{6.24}$$

since both vectors are normalised. We now calculate the flake size. We first project the flake data onto the fitting plane along with a horizontal integer-spaced grid $Z = \{z \in \mathbb{Z}^3 | z_3 = 0\}$ along its normal, giving

$$S^i = !\left\{\min_{z_j}(z^j - p)\right\} \quad \forall p \in \mathbb{P}_1(p^i) \tag{6.25}$$

where each element is distinct in terms of coordinate values. We can then measure the surface area in μm^2 as

$$v^i = \sqrt{r_1^2 + r_3^2}\sqrt{r_2^2 + r_3^2}|S^i| = \sqrt{1.17^2 + 0.4^2}\sqrt{1.17^2 + 0.4^2}|S^i| = 1.5289|S^i| \tag{6.26}$$

in our case where $|S^i|$ is the number of elements in the set S^i and r_1, r_2 and r_3 are the sizes of the pixels in μm in the two lateral and depth directions respectively. To report the results, we filter out remaining noise by removing grouped points which are too few to represent a flake ($\leqslant$ 5% expected flake size).We remove flake conjunctions from consideration by filtering those which are much too large ($\geqslant$ 10 times expected size) and excluding those whose mean depth values differ considerably from the fitted plane, indicating a considerable joint angle which is unexpected in a single flake.

6.3 Automotive panel coating analysis

In this study, five paint samples were scanned with our FF-OCT system in 9 different regions. The top two layers, clear coat and base coat, were focused in order to analyse the characteristics of the metallic flakes in the base coat. Figure 6.3 shows the metallic flakes within base coat layer under high magnification microscopy. The fulgurant sparks are the reflection of some of metallic flakes and the rest of flakes cannot be observed due to the angle of incident illumination light. Figure 6.4 shows the layer structure of automotive paint by our FF-TD-OCT, the base coat and the flakes within can be clearly resolved through the B-scan image.

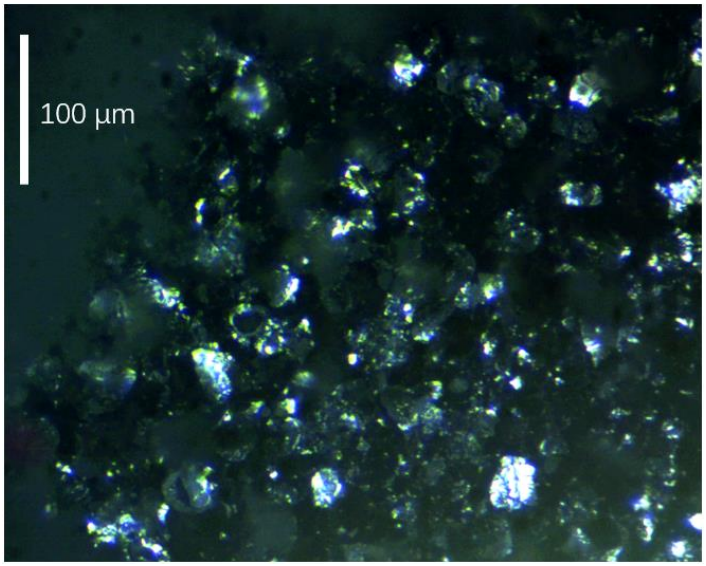

Figure 6.3: Metallic flakes under high magnification microscopy.

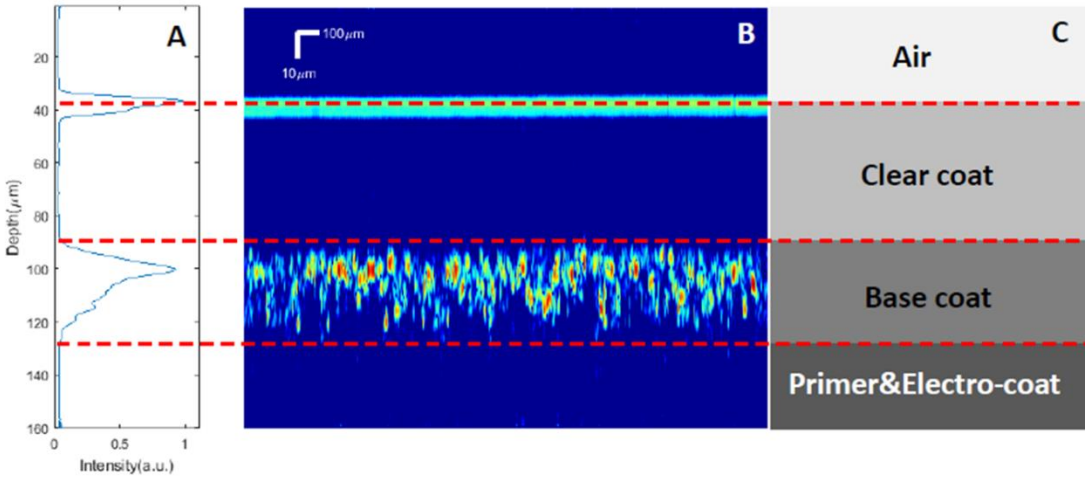

Figure 6.4: a) Average depth profile of automotive paint sample. b) Cross-sectional image of automotive paint sample. c) Schematic of automotive paint sample. The clear coat of sample is transparent while the base coat is cloudy because metallic flakes within are strong optical scattering media.

6.3.1 Cross-section images of automotive paint samples

The high intensity peaks in OCT cross-section images indicate reflections at the interface between two different media with different refractive indices. Figure 6.5 shows cross-sectional images of the Indus silver #1, Mauritius blue, Barolo black and Santorini black paint samples and their depth profiles. The clear coat and base coat can be determined as the first and second layers since the clear coat is transparent and the base coat has strong scattering metallic flakes inside. It can be noted from the figure that the number of flakes in the Indus silver and Mauritius blue samples is higher than that in the Barolo black and Santorini black samples. It should be noted that the OCT images are not photographic images of flakes. The thickness of the flakes in Figure 6.5 represent axial resolution at the surface position of the flakes.

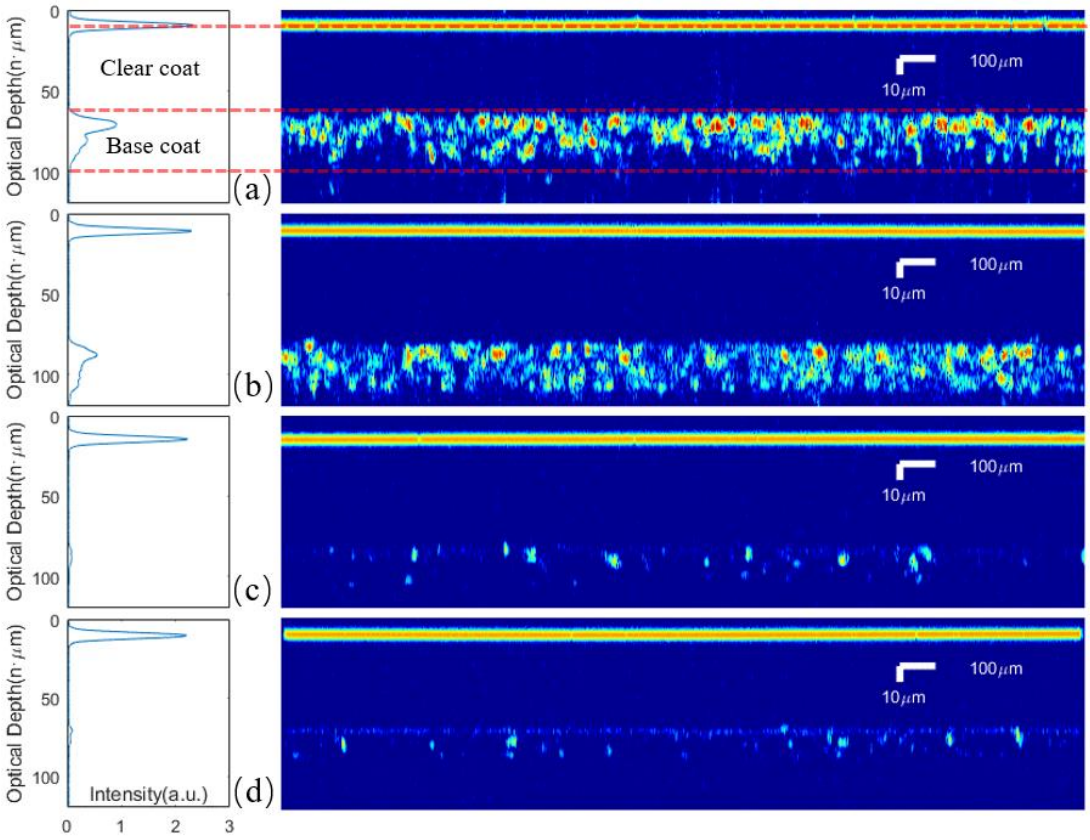

Figure 6.5: a) Indus silver sample #1; b) Mauritius blue sample; c) Barolo black sample; d) Santorini black sample; The right side shows the cross-section images of four samples and the left side shows their corresponding average depth profiles. The cross-sectional images show that there are more flakes in the Indus silver and Mauritius blue samples than Barolo black. (n is the refractive index of the sample.)

In order to quantify the metallic flakes in base coat layer, the 3D OCT data of the base coat layer is isolated from the raw data and processed. Figure 6.6a shows the small metallic flakes in the base coat after 3D segmentation. Cross section images of the flakes are shown in Figures 6.6b and Figure 6.6d. Figure 6.6c shows the top view (*en-face* image) of the flakes from which the flake size in 2D could be estimated. Since *en-face* images do not give information of the

flake orientation, the method of calculating flake size in 3D is not desirable, as discussed in a later section.

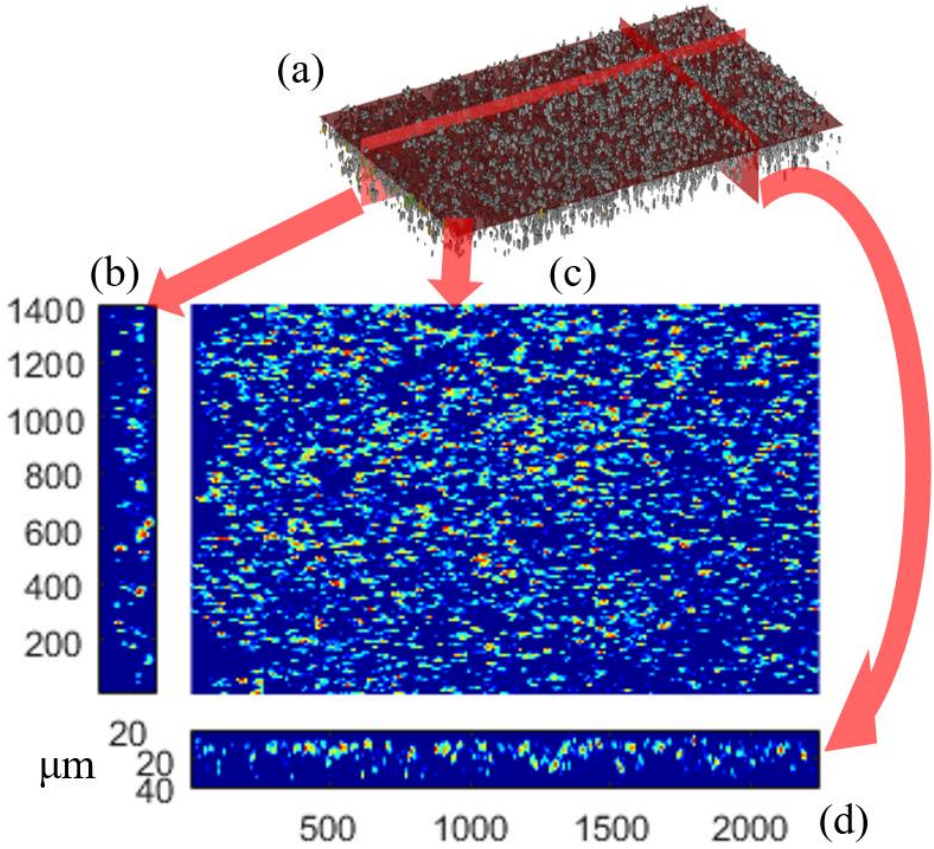

Figure 6.6: 3D view and cross-section images of the base coat of Indus silver #1. a) 3D view with metallic flakes. The base coat is isolated from raw OCT data before signal processing. b), c), d) show three cross-section images of base coat in three orthogonal planes.

6.3.2 Analysis of metallic flakes properties: size, number and orientation

The aim of this experiment is to characterise the flakes' size, number and orientation in 3D using nine sections of each sample. Therefore, each section is scanned with our FF-OCT, the base coat is isolated and 3D segmentation applied (as shown in Figure 6.7a-c). In order to calculate the number of flakes and create an index, a labelling process is subsequently applied to each section of the automotive paint samples. Each segmented flake is projected onto a best-fit plane and the size and orientation angle of each flake is calculated, as shown in Figure 6.8a-c.

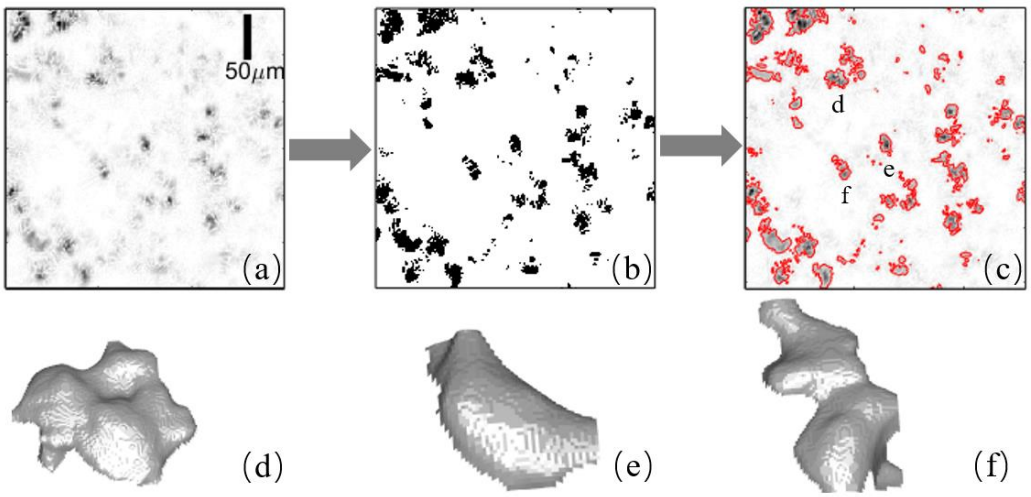

Figure 6.7: Example showing part of the segmentation of an en-face OCT image of car paint. An *en-face* OCT volume image (a) of metallic flakes is segmented by determining the level set function φ (b) in order to obtain the segmentation result (c). T (d)-(f) surface maps of example flakes.

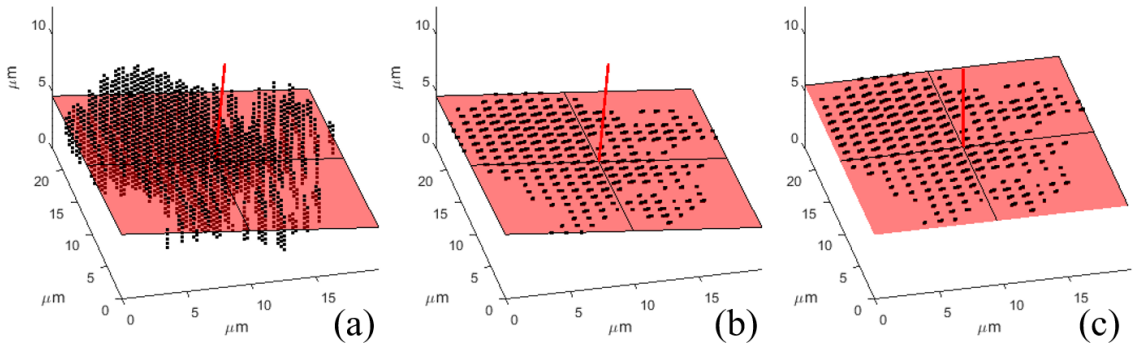

Figure 6.8: The orientation is defined as the angle between the fitting plane of flake and horizontal plane and calculated using the normal vectors of these two planes. Given the orientation, we measure a flake (a) by flattening it to a plane (b) and rotating it to be parallel with the horizontal plane (c).

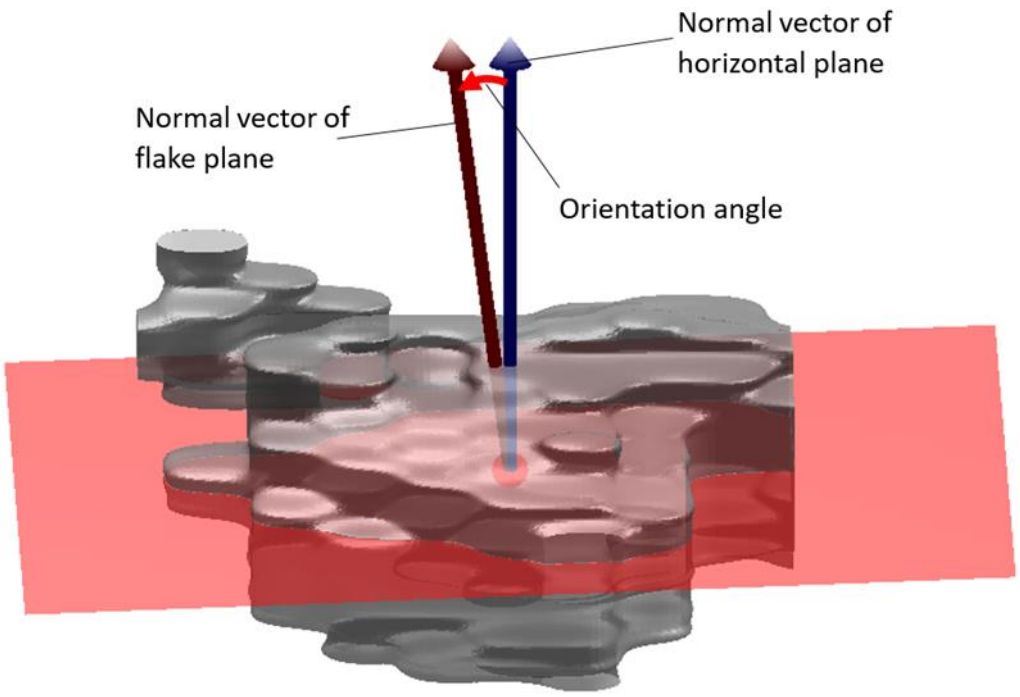

Figure 6.9: A 3D construction image of a single flake and its orientation plane.

The mean numbers of flakes for the two Indus silver samples across nine sections were 1994 ± 187 (633 ± 59/mm^2) and 1923 ± 189 (610 ± 60/mm^2) respectively, as shown in Table 6.1. The results show that the Mauritius blue sample has a similar density of flakes to the two Indus silver samples at 626 ± 17/mm^2, while the Barolo black and Santorini black samples have fewer flakes at 202 ± 14/mm^2 and 368 ± 51/mm^2 respectively. In addition to flake number, the results in Table 6.1 also show that the size of the flakes in the two Indus silver and Mauritius blue samples is similar, while the size of those in the Barolo black and Santorini black samples is smaller. By plotting the percentage of total flake number against flake size (as shown in Figure 6.10), we can see the flake number distribution by individual flake size. This figure suggests that the flakes' size distribution in the two Indus silver and Mauritius blue samples are different from the two black samples.

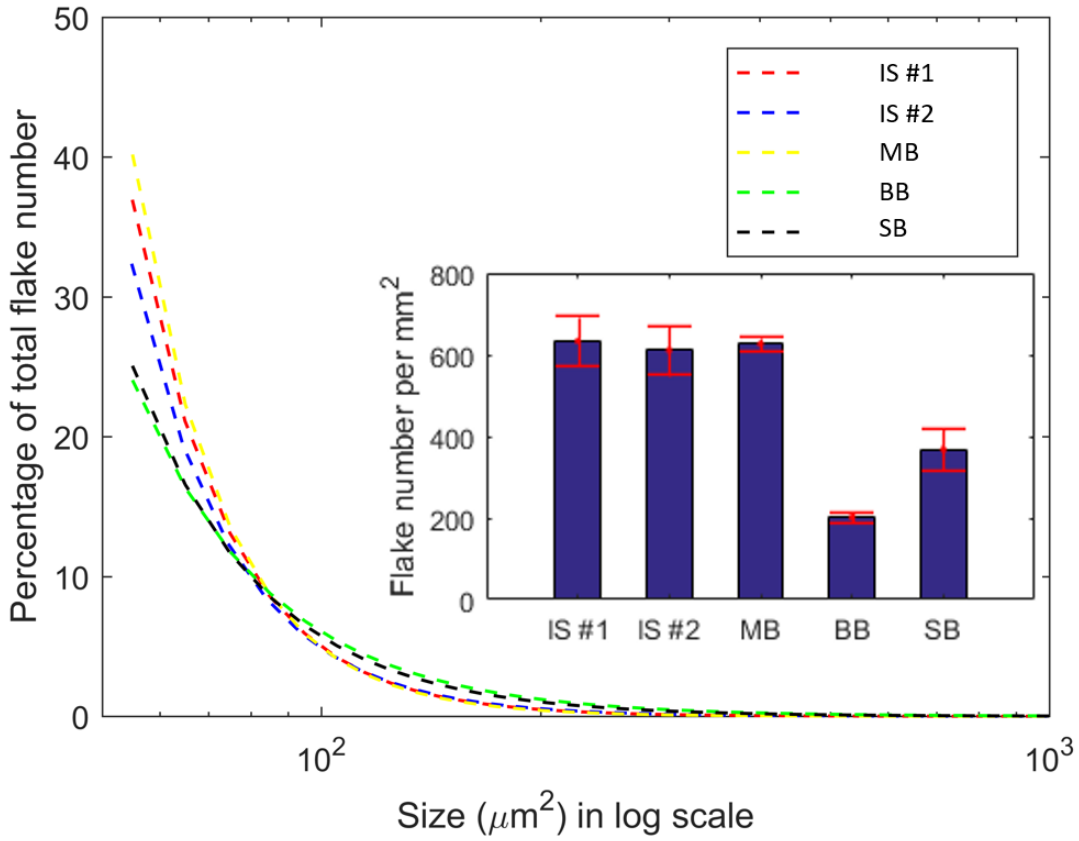

Figure 6.10: Histograms of percentage of total flakes number in samples. The inset enlarged view of this histogram shows that the Indus silver #1&2 and Mauritius blue sample have the consistent distribution of flake size, which suggested that the flakes in these three samples are the same kind, while the two black samples are different. The inset bar chart shows the flake numbers in unit area of five different samples. (IS #1: Indus silver #1, IS #2: Indus silver #2, MB: Mauritius blue, BB: Barolo black, SB: Santorini black.)

Table 6.1: The numbers, sizes and orientations of flakes in five paint samples.

	Number		Radius (μm)			Orientation (°)		
Samples	Mean	Std	Mean	Std1[1]	Std2[2]	Mean	Std1	Std2
Indus silver #1	1994	187	10.26	1.45	10.58	8.67	1.30	10.62
Indus silver #2	1923	189	10.28	1.92	10.54	9.01	1.86	11.96
Mauritius Blue	1972	54	10.26	1.62	10.50	9.08	0.41	10.82
Barolo black	635	43	10.06	2.27	9.32	6.38	2.08	11.05
Santorini black	1159	160	9.49	2.06	9.69	6.22	0.88	10.25

1. Standard deviation (Std) of mean flake sizes of 9 regions.
2. Standard deviation (Std) of individual flake sizes within a region

The orientation of a single flake is defined as the acute angle between the automotive panel surface (the horizontal plane), and the flake surface. By fitting each flake surface with a plane, the orientation angle can be calculated as the acute angle between a plane which is fit to the flake surface and the horizontal plane. Table 6.1 shows the mean orientations for each sample and their standard deviations. The flakes in the two black samples have a slightly smaller angle than the silver and blue samples.

6.3.3 Validation of results

To validate the repeatability of the OCT measurements, the scanning and processing of section number 5 of the Indus silver #1 automotive paint sample were repeated five times. Figure 6.11 shows the measured results of the

number of flakes and mean flake size. The consistency of these results demonstrates the repeatability of our OCT measurements. Additionally, Figure 6.11 shows a set of *en-face* images of repeated OCT data slices and their segmented results. The mean flake number of the five repeated measurements is calculated as 2133 ± 30. The mean flake size is 10.13 ± 1.35μm (radius). The mean orientation angle is 7.58 ± 0.22°. This demonstrates consistency.

In order to validate our experimental results, we cut and polish the samples, and obtain cross sectional images with high magnification microscopy, as shown in Figure 6.13 (right column). Using this 2D data, we can segment the flakes and calculate their angle to the horizontal line. Doing this for a series of cross-section images of the Indus silver #2, Mauritius blue, Barolo black and Santorini black, the mean angles are calculated as 6.5, 5.9, 2.8, 3.8 degrees. The estimates of these angles in 3D agree with our OCT results as shown in Table 6.2. The cross-sectional micrographs provide only 2D information while our system is capable of imaging in 3D.

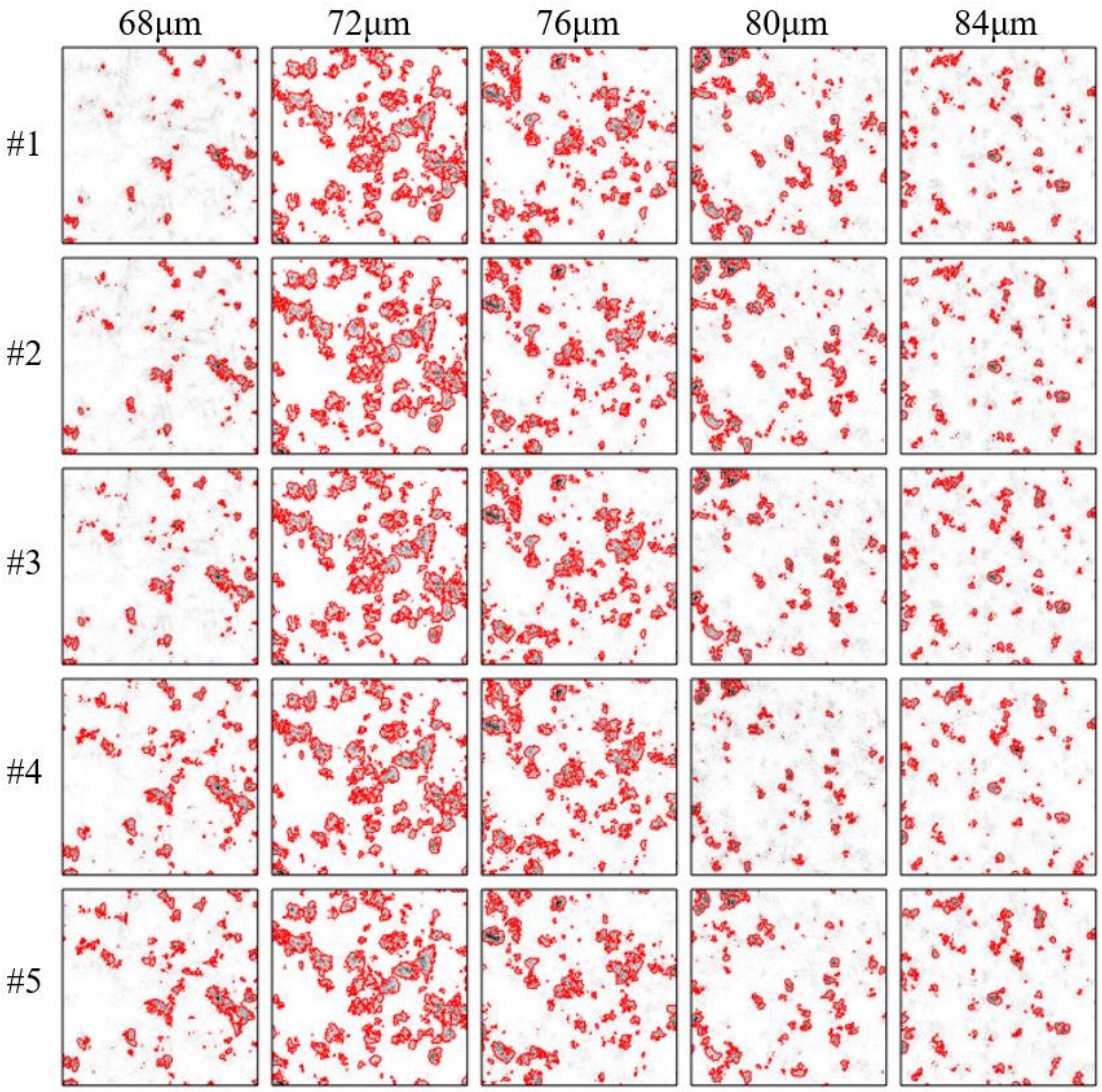

Figure 6.11: A set of *en-face* images of 5 repeated OCT measurements with their segmentation results overlaid. The consistency between repeated data demonstrates the repeatability of our OCT system and segmentation method. Each row represents 5 different repeated data and each column denotes 5 different optical depths (68µm, 72µm, 76µm, 80µm, 84µm)

Table 6.2: Comparison of mean flake orientations from our OCT and microscopy.

	Mean Orientation (°)	
Sample	Our FF-TD-OCT	Microscopy
Indus silver #2	9.01±1.86	9.2
Mauritius blue	9.08±0.41	8.3
Barolo black	6.38±2.08	4.0
Santorini black	6.22±0.88	5.4

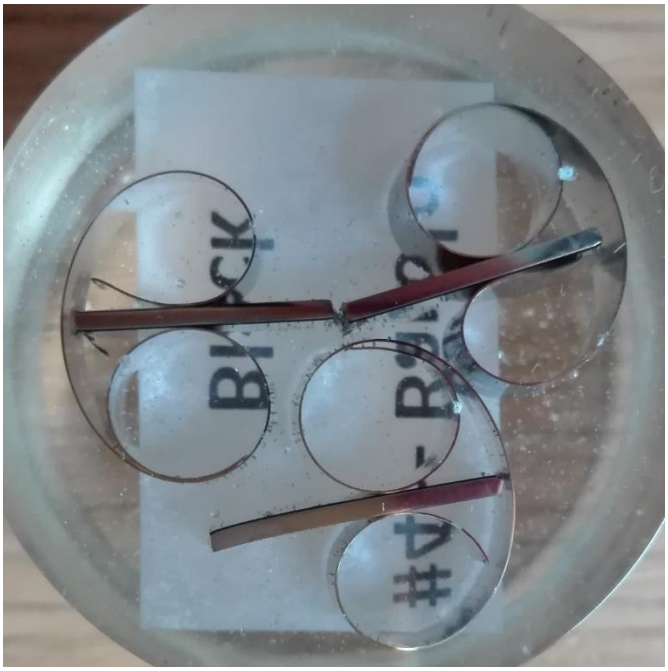

Figure 6.12: Dissected automotive samples, which are fixed and resin-mounted. The cross-sections of samples are carefully polished and placed upwards in order for microscopy imaging.

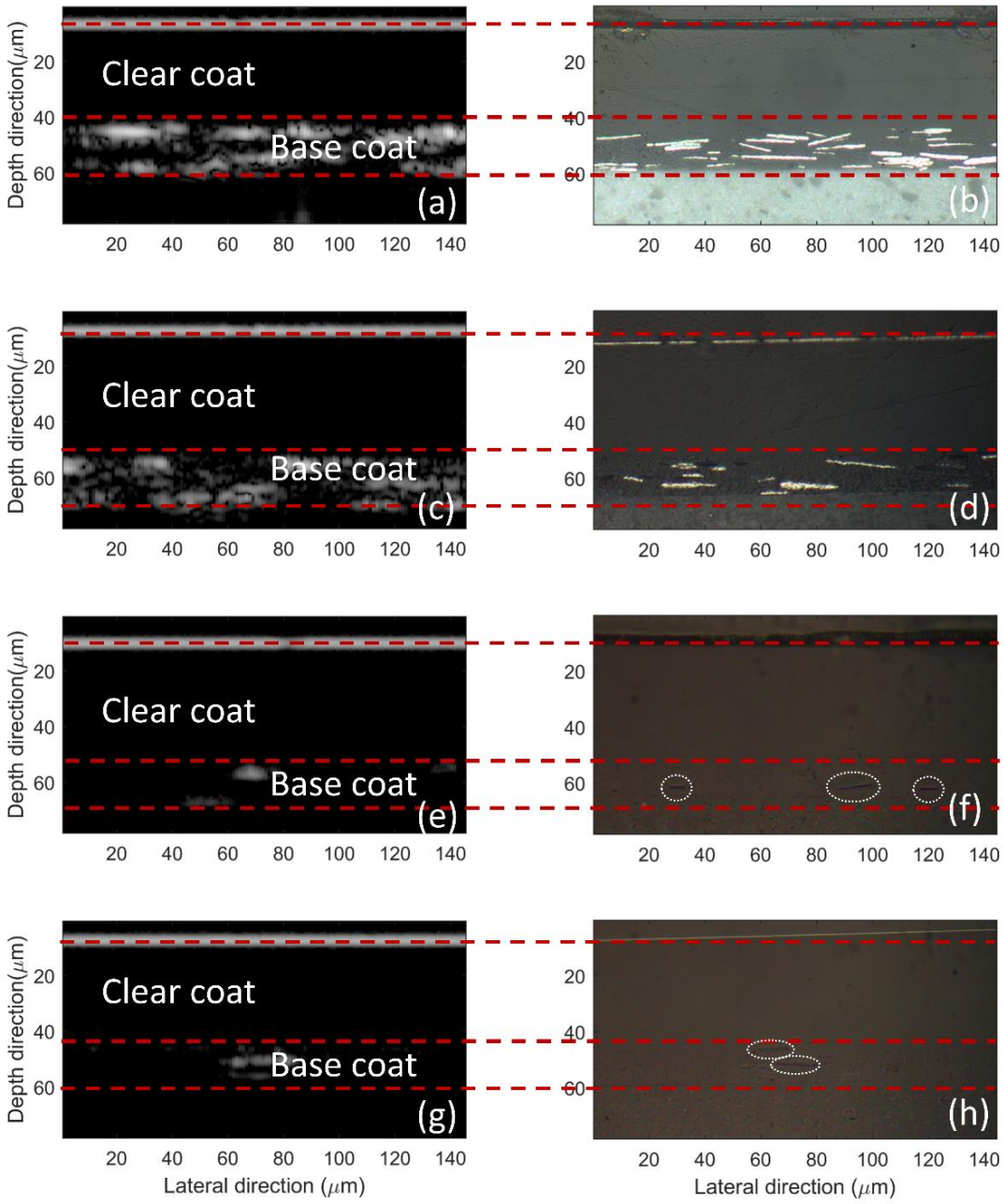

Figure 6.13: Comparison of B-scans from our OCT device (left column) with micrographs (right column) for four samples: Indus silver, Mauritius blue, Barolo black and Santorini black. The micrographs achieve a good quality result for validation, but necessitates destruction of the sample while our device keeps it intact.

6.4 Discussion

In this study, we have successfully measured metallic flakes within the base coat of automotive paint using our FF-TD-OCT system with a high lateral resolution of 4.4μm and integrated 3D variational segmentation, labelling and measurement technique. Five paint samples were scanned in nine regions and the base coat analysed automatically. The flake properties of the different panels were characterised, including their number, size and orientation.

Compared to classic commercial measurement methods related to automotive paint layers, such as ultrasound testing [3,4] and eddy-current testing [5,6], our OCT system is able to measure samples without contact with the sample surface. This allows our OCT system to measure paint samples regardless of the smoothness of the surface and makes it suitable for online in-situ quality control. Commercial measurement methods and recently developed non-contact paint layer measurement methods such as TPI [7–9] achieve insufficient lateral resolution to measure the metallic flakes, which are typically approximately 10μm in radius.

Both CLSM and our OCT system can achieve sufficiently high spatial resolution to resolve flakes and calculate their properties. In both cases, the en-face plane where the samples are being measured is kept coincident with the focal plane during 3D scanning, which provides a high-quality 3D construction. Neither method can penetrate metal material and thus only the clear coat and base coat layers can be resolved. Compared to CLSM, our OCT has a longer working distance and only requires a depth (z-axis) scan to capture 3D data while CLSM is a scanning point system and requires all three axes to be

scanned (x − y − z axis). Moreover, CLSM has not been demonstrated on real industrial car paint samples before. The advantages of our FF-TD-OCT over competing methods makes it the preferred choice for future QA of automotive paint coating systems. Indeed, to the best of our knowledge, the work reported in this chapter represents the first system capable of measuring the size, number and orientation of metallic flakes in automotive paint.

The previous method of calculating the properties of flakes relies on taking 3D data of the sample by 2D lateral scans, making a peak intensity map of the base coat and thresholding the intensity to get the shape and size of flakes in 2D maps [20]. Compared to previous work, our experiment focuses on small metallic flakes of micrometre size and manages to calculate the flakes' size in 3D space instead of a 2D surface peak intensity map which neglects that the flakes are projected onto the horizontal plane which distorts the measure. Therefore, it is novel to segment and label the acquired 3D OCT data of these small flakes in order to calculate their number, size and orientation accurately and precisely. In addition, our variational segmentation method is not restricted to our FF-TD-OCT system and can be applied other OCT setups and other 3D imaging techniques such as CLSM.

One limitation of our measurement method is that a small number of flakes were excluded from the segmentation results in order to get a more accurate result of the mean flake size, since there are physically conjunct flakes which were recognised as a single flake. Although we have identified such flakes automatically, the problem of segmenting these flake conjunctions is sophisticated, related to the conjunction angle between several flakes, and will be studied in future work.

Another limitation is that the light source of our OCT system is near-infrared, which cannot penetrate metal. Therefore, we have only measured the clear coat and base coat of automotive paint layers. We have demonstrated that our FF-OCT system is capable of identifying, resolving and measuring small flakes in a non-destructive and non-contact manner.

By combining with our 3D variational segmentation and labelling method, we have presented a technique of determining in 3D space the number, size and orientation of flakes within the base coat layer of automotive paint samples which, to our knowledge, is the first time that this has been done. This technique has the potential to considerably benefit QA testing of paint coating processes in the automotive industry.

6.5 Summary

In summary, the film builds in automotive paint systems have the functions of protecting vehicles' body from environmental corrosion as well as enhancing their aesthetic appearance. The flakes within base coat layer, the middle layer in the automotive paint system, can give a sparkle effect and the geometry properties of these flakes have a significant effect on the achievement of desired appearance in all angles. Therefore, we have developed a FF-TD-OCT system along with integrated analysis algorithms and demonstrated its capability as a non-contact and non-destructive analytical tool for measuring small flakes, characterising their number, size and orientation in 3D space for the first time. The high lateral resolution of our FF-TD-OCT system of 4.4μm, while keeping the flakes in focus, makes it possible to resolve individual flakes within the base coat of automotive paint which is not achievable by current

commercial methods. Our unique combination of FF-TD-OCT and flake segmentation, allowing the metallic flakes to be measured, has the potential to be of considerable benefit to the automotive industry as a quality assurance tool for coating processes.

Reference

1. N. K. Akafuah, S. Poozesh, A. Salaimeh, G. Patrick, K. Lawler, and K. Saito, “Evolution of the automotive body coating process - a review,” Coatings 6, 24 (2016).

2. M. Nichols and J. Tardiff, Active Protective Coatings (Springer Netherlands, 2016), chap. Automotive Coatings, 373–384.

3. F. J. Maile, G. Pfaff, and P. Reynders, “Effect pigments-past, present and future,” Progress in Organic Coatings 54(3), 150-163 (2005).

4. J. Allin, P. Cawley, andM. Lowe, “Adhesive disbond detection of automotive components using first mode ultrasonic resonance,” NDT & E International 36, 503–514 (2003).

5. S. A. Titov, R. G. Maev, and A. N. Bogachenkov, “Pulse-echo NDT of adhesively bonded joints in automotive assemblies,” Ultrasonics 48, 537–546 (2008).

6. B. Auld and J. Moulder, “Review of advances in quantitative eddy current nondestructive evaluation,” Journal of Nondestructive Evaluation 18, 3–36 (1999).

7. J. García-Martín, J. Gómez-Gil, and E. Vázquez-Sánchez, “Non-destructive techniques based on eddy current testing,” Sensors 11, 2525–2565 (2011).

8. K. Su, Y.-C. Shen, and J. A. Zeitler, “Terahertz sensor for non-contact

thickness and quality measurement of automobile paints of varying complexity," IEEE Transactions on Terahertz Science and Technology 4, 432–439 (2014).

9. S. Krimi, J. Klier, J. Jonuscheit, G. von Freymann, R. Urbansky, and R. Beigang, "Highly accurate thickness measurement of multi-layered automotive paints using terahertz technology," Applied Physics Letters 109, 021105 (2016).

10. M. Sudo, J. Takayanagi, and H. Ohtake, "Nondestructive thickness measurement system for multiple layers of paint based on femtosecond fiber laser technologies," Journal of Infrared Millimeter and Terahertz Waves 37, 1139–1147 (2016).

11. J. F. Federici, B. Schulkin, F. Huang, D. Gary, R. Barat, F. Oliveira, and D. Zimdars, "THz imaging and sensing for security applications - explosives, weapons and drugs," Semiconductor Science and Technology 20, S266 (2005).

12. Y. Shen, T. Lo, P. Taday, B. Cole,W. Tribe, andM. Kemp, "Detection and identification of explosives using terahertz pulsed spectroscopic imaging," Applied Physics Letters 86, 241116 (2005).

13. Y.-C. Shen, "Terahertz pulsed spectroscopy and imaging for pharmaceutical applications: a review," International Journal of Pharmaceutics 417, 48–60 (2011).

14. R. H. Webb, "Confocal optical microscopy," Reports on Progress in Physics

59, 427 (1996).

15. J. Pawley and B. R. Masters, “Handbook of biological confocal microscopy,” Optical Engineering 35, 2765–2766 (1996).

16. E. Kirchner and J. Houweling, “Measuring flake orientation for metallic coatings,” Progress in Organic Coatings 64, 287–293 (2009).

17. L.-P. Sung,M. E. Nadal,M. E.McKnight, E.Marx, and B. Laurenti, “Optical reflectance of metallic coatings: effect of aluminum flake orientation,” Journal of Coatings Technology 74, 55–63 (2002).

18. X. Maldague, Theory and Practice of Infrared Technology for Nondestructive Testing (Wiley, NY, USA, 2001).

19. M. Omar, K. Chuah, K. Saito, A. Numasato, andM. Sakakibara, “Infrared seed inspection system(IRSIS) on painted car shells,” Infrared Physics & Technology 48(3), 240-248 (2006).

20. Y. Dong, S. Lawman, Y. Zheng, D. Williams, J. Zhang, and Y.-C. Shen, “Nondestructive analysis of automotive paints with spectral domain optical coherence tomography,” Applied Optics 55, 3695–3700 (2016).

21. N. Zhang, C. Wang, Z. Sun, H. Mei, W. Huang, L. Xu, L. Xie, J. Guo, Y. Yan, Z. Li et al., “Characterization of automotive paint by optical coherence tomography,” Forensic Science International 266, 239–244 (2016).

22. D. Mumford and J. Shah, “Optimal approximations by piecewise smooth functions and associated variational problems,” Communications on Pure

and Applied Mathematics 42, 577–685 (1989).

23. T. F. Chan and L. A. Vese, “Active contours without edges,” IEEE T. Image Process. 10, 266–277 (2001).

24. C. Gout, C. Le Guyader, and L. Vese, “Segmentation under geometrical conditions using geodesic active contours and interpolation using level set methods,” Numerical Algorithms 39, 155–173 (2005).

25. N. Otsu, “A threshold selection method from gray-level histograms,” Automatica 11, 23–27 (1975).

26. M. K. Garvin, M. D. Abràmoff, R. Kardon, S. R. Russell, X. Wu, and M. Sonka, “Intraretinal layer segmentation of macular optical coherence tomography images using optimal 3-D graph search,” IEEE Transactions on Medical Imaging 27, 1495–1505 (2008).

27. S. J. Chiu, X. T. Li, P. Nicholas, C. A. Toth, J. A. Izatt, and S. Farsiu, “Automatic segmentation of seven retinal layers in SDOCT images congruent with expert manual segmentation,” Optics Express 18, 19413–19428 (2010).

28. Q. Yang, C. A. Reisman, Z. Wang, Y. Fukuma, M. Hangai, N. Yoshimura, A. Tomidokoro, M. Araie, A. S. Raza, D. C. Hood et al., “Automated layer segmentation of macular OCT images using dual-scale gradient information,” Optics Express 18, 21293–21307 (2010).

29. Fuller, R. Zawadzki, S. Choi, D. Wiley, J. Werner, and B. Hamann, “Segmentation of three-dimensional retinal image data,” IEEE Transactions

On Visualization And Computer Graphics 13, 1719–1726 (2007).

30. K. Vermeer, J. Van der Schoot, H. Lemij, and J. De Boer, “Automated segmentation by pixel classification of retinal layers in ophthalmic OCT images,” Biomedical Optics Express 2, 1743–1756 (2011).

31. S. Osher and J. A. Sethian, “Fronts propagating with curvature-dependent speed: algorithms based on Hamilton- Jacobi formulations,” Journal of Computational Physics 79, 12–49 (1988).

32. L. I. Rudin, S. Osher, and E. Fatemi, “Nonlinear total variation based noise removal algorithms,” Physica D: Nonlinear Phenomena 60, 259–268 (1992).

33. Yazdanpanah, G. Hamarneh, B. R. Smith, and M. V. Sarunic, “Segmentation of intra-retinal layers from optical coherence tomography images using an active contour approach,” IEEE Transactions on Medical Imaging 30, 484–496 (2011).

34. B. M. Williams, J. A. Spencer, K. Chen, Y. Zheng, and S. Harding, “An effective variational model for simultaneous reconstruction and segmentation of blurred images,” Journal of Algorithms & Computational Technology 10, 244–264 (2016).

35. T. Goldstein and S. Osher, “The split Bregman method for L1-regularized problems,” SIAM Journal on Imaging Sciences 2, 323–343 (2009).

36. Chambolle and T. Pock, “A first-order primal-dual algorithm for convex problems with applications to imaging,” Journal of Mathematical Imaging and Vision 40, 120–145 (2011).

37. Ghanbari, L. Rada, and K. Chen, “A restarted iterative homotopy analysis method for two nonlinear models from image processing,” International Journal of Computer Mathematics 91, 661–687 (2014).

Chapter 7. Conclusion and future work

7.1 Conclusion

The OCT technique has been demonstrated as a three-dimensional analytical non-destructive, non-contact and non-invasive testing method with a high spatial resolution and strong penetrative capability. These advantages make OCT suitable in film coating evaluation and characterisation. As an extension of TD-OCT, the FF-TD-OCT, inherits the advantages of the OCT technique and increases its data acquisition speed and efficiency by using a parallel detection scheme, allowing in-line measurement and in vivo measurement to be available.

In this thesis, a free-space FF-TD-OCT system has been developed to investigate the coating layer structures of pharmaceutical pellets, the surface-power distribution of human cornea and the small flakes properties of automotive panels. The developed FF-TD-OCT system utilised two different light sources, namely a thermal tungsten-halogen light bulb and an NIR LED, each for different purposes: The visible light source (i.e. the tungsten-halogen bulb) was used for thin layers and surface structure measurement because it provides high axial resolution, such as the surface optical power distribution of a human cornea; the NIR light source was used for high-penetration deep-layer structural measurement and for small particles within layers, such as the structural evaluation of the pharmaceutical pellet coating layer and the property analysis of automotive metallic flakes, because it provides better penetration. The best lateral resolution that our FF-TD-OCT system can provide is 4.4μm,

and the best axial resolution is 1.6μm for the thermal light source and 3.9μm for NIR light source.

In order to demonstrate the imaging capabilities of the FF-TD-OCT system, it has been applied to pharmaceutical pellets, human corneas, and automotive paint system analysis. Challenges should be handled in response to different applications.

Pharmaceutical pellet coating thickness

The film coating of pellets serves as an effective barrier in the human body to control the release time and rates of API. Film coating thickness has an effect on the decomposition speed of pellets or tablets in the human body. The precise evaluation of film coating thickness is of significance to ensure the high quality and uniformity of pharmaceutical pellets. In chapter 4, we proposed our FF-TD-OCT system to characterize the coating structure of small multi-layer pharmaceutical pellets with a diameter of less than 1mm and developed a thickness calculation method, which relies on the depth profile of averaged A-scan signals in 3D OCT data.

The two pellet samples used in this experiment are a two-layer drug-loaded pellet and a three-layer drug-loaded pellet. The mean thickness of a two-layer pellet was determined as precisely 39.7 ± 7.3μm and 49.1 ± 7.0μm, for the outer and inner layers respectively. The mean thicknesses of a three-layer pellet were 26.5 ± 2.3μm, 20.6 ± 3.4μm and 57.3 ± 7.2μm, for each layer respectively. Additionally, particle-like features in the inner layer can be clearly resolved from the cross-section images. It is demonstrated that our FF-TD-OCT has the

potential in imaging and evaluating the coating thickness distributions of pharmaceutical pellets.

Optical power distribution of human cornea

Eye diseases, such as astigmatism and glaucoma, may cause distorted or blurred vision and even vision loss. The ability to measure and analyse the shape and power of the human cornea is of benefit in therapeutic surgical treatment; precise information about the shape and power of the corneal surface is of significance to any corrective procedures to the corneal surface. Previous OCT applications in corneal power measurement have focussed on the net power measurement of the cornea. And the single-point scheme OCT system scans cornea samples radially along a series of meridians across the vertex point and produce a series of meridional images. Motion correction algorithms should be applied to adjust the surface map of cornea due to the motion of the human eye *in vivo* and possible errors in non-telecentric scan deformation. However, an FF-TD-OCT technique parallel detection scheme can solve the non-telecentric scan problem by acquiring a series of *en-face* images of cornea samples.

In chapter 5, our FF-TD-OCT was used to measure human corneas and was combined with an average back-vertex focal length and average power calculation algorithm to calculate the individual optical power of each point at the surface of human corneas. Six formalin-fixed and two fresh corneas were scanned in a large area of 4.95 × 4.92mm^2, and their power maps were illustrated. The cross-section image of the cornea generated by our FF-TD-OCT system clearly shows its structure, including epithelium, Bowman's layer and

stroma and also the features of the stroma. Overall, the combination of our FF-TD-OCT and the individual power calculation method is of significant benefit in planning any corrective procedures to the cornea and in facilitating the design and fit of contact lens.

Metallic flakes in automotive paint system

The base coat (consisting of colour pigments and metallic or mica flakes) of the automotive paint system provides vehicles with aesthetic enhancement and increases their attractiveness. The flake size, weight, orientation and geometry have an effect on achieving the desired appearance from all angles. Therefore, it's important to measure the flake properties during automotive industrial fabrication to achieve the desired appearance and maintain the consistency of automotive paint. Non-destructive methods, such as ultrasound testing, eddy-current testing and terahertz imaging, are unsuitable to capture these small metallic flakes (diameter < 10μm), due to their insufficient resolution.

In chapter 6, we introduce our FF-TD-OCT system along with an integrated 3D variational segmentation algorithm to measure small metallic flakes within the base coat layer of the automotive paint system non-destructively and without contact. The properties of the small flakes, including their number, size, and orientation in 3D, were characterised for the first time. The high lateral resolution of our FF-TD-OCT system makes it possible to resolve individual small flakes within the base coat layer of automotive paint, which cannot be achieved by current commercial methods. The unique combination of FF-TD-OCT and the 3D variational flake segmentation method, allowing the flakes to

be measured, has the potential to be of considerable benefit to the automotive industry as a QA tool for painting processes.

7.2 Major contributions

In sum, the major contributions of our research are as follows:

- The development of a free-space FF-TD-OCT system with a fast data-acquisition speed and high spatial resolution, at 1.6 × 4.4μm^2 (axial × lateral), which can achieve a variable image magnification from 1 to 5 to respond to samples of different sizes

- The characterisation of the pharmaceutical pellet with multi-layer coating structures using our FF-TD-OCT system. The layer structures are distinguished, and coating thickness is accurately calculated from the depth profiles of averaged A-scan signals.

- Intra-corneal imaging of formalin-fixed and fresh human corneas with the anterior surface, epithelium layer and Bowman's layer clearly resolved; non-telecentric scan problem avoided by using the *en-face* imaging FF-TD-OCT technique

- The calculation of individual optical corneal power and illustration of power maps by reconstructing the corneal surfaces from OCT data and developing and applying an average back-vertex focal length calculation algorithm, which reduces the paraxial approximation errors

- Cross-sectional imaging of different automotive paint panel samples with the clear coat and base coat layers clearly resolved, as well as the small

metallic flakes (diameter <10μm)

- Characterisation of the properties of metallic flakes in automotive paint system, including their size, number and orientation in 3D space by combining our FF-TD-OCT system and a novel 3D variational image segmentation method—It is the first time to resolve metallic flakes and calculate their properties, which is not achievable by current commercial methods

7.2 Future works

Since our FF-TD-OCT system has been applied to film coatings of pharmaceutical pellets and automotive panels in this thesis, future applications can be expanded to other areas related to film coating, such as ceramic glazes of porcelain and pottery, colour films for oil paintings and mural paintings, and wall paint architecture. These objectives have momentous historical and cultural values and can be only measured with non-destructive methods. Its high resolution and high penetration can make OCT suitable in authentication, the characterization of paint layer coating thickness and the identification of defects or cracks within coating layers.

With regard to hardware, the current FF-TD-OCT system is based on an optical platform and is not portable for different measurement circumstances. Future work can focus on how to make our FF-TD-OCT system more compact, able to be fixed on a portable optical breadboard. In addition, our current FF-TD-OCT system has the limitation of a relatively long-time acquisition time (a few minutes) for 3D OCT data. The data scanning time is limited by the frame rate of the camera, and it also takes a long time to upload 3D data from the

camera to the PC. Our FF-TD-OCT can be updated with 2D detectors with higher frame rates and PCs with better GPUs and solid-state hard drives to reduce time spent on data scanning, storing and processing. It will be of benefit to the in-line measurement for pharmaceutical pellets and human cornea *in vivo*.

Regarding software, our current novel 3D variational image segmentation algorithm can be applied to not only metallic flakes but also particle-like elements, such as drug powder within the pharmaceutical pellets and tablets. The 2D image segmentation algorithms, such as those for detecting the layer surface and interface automatically, could be useful for fast analysis of layer structure. Furthermore, a graphic user interface can be introduced to control all data acquisition and processing tasks for convenience and to reduce programming work.